Simulation of Electron Bernstein Waves in FLiPS with various numerical methods

Von der Fakultät Energie-, Verfahrens- und Biotechnik
der Universität Stuttgart
zur Erlangung der Würde eines Doktors der Naturwissenschaften
(Dr. rer. nat.) genehmigte Abhandlung

vorgelegt von
Kirill Rumiantsev
aus
Sewerodwinsk, Russland

Hauptberichter:	Prof. Dr. Thomas Hirth
1. Mitberichter:	Prof. Dr. Marc Kreutzbruck
2. Mitberichter:	Prof. Dr. Emanuele Poli

Tag der mündlichen Prüfung: 27.10.2021

Institut für Grenzflächenverfahrenstechnik und Plasmatechnologie
der Universität Stuttgart
2021

Kurzfassung

Die Plasmaerzeugung und -heizung durch Mikrowellen ist ein wichtiges Forschungsthema im Bereich der kontrollierten Kernfusion. Alle modernen Fusionsexperimente, wie Wendelstein 7-X verwenden Mikrowellenheizung. Diese erfolgt hauptsächlich an den Resonanzen, wo die Mikrowellen effizient absorbiert werden. Das Heizverfahren muss so ausgelegt sein, dass die Mikrowellen die Resonanz erreichen können. Wenn das Plasma jedoch die Cutoff-Dichte überschreitet, werden die Mikrowellen reflektiert, und die Resonanz wird unzugänglich. Es ist allerdings möglich, die Heizung mit Elektron-Bernstein-Wellen (EBW) durchzuführen, da diese elektrostatischen Wellen im Gegensatz zu den elektromagnetischen Plasmawellen auch bei Plasmadichten oberhalb der Cutoff-Dichte propagieren. EBW können nicht im Vakuum propagieren und müssen deshalb durch einen Kopplungsprozess erzeugt werden. Sowohl die O- als auch die X-Mode können an die EBW gekoppelt werden.
Diese Arbeit untersucht die Kopplung von O- und X-Mode an die EBW und die Propagation der EBW mit verschiedenen numerischen Methoden. Die Anwendung nur einer numerischen Methode ist nicht ausreichend, da die Kopplung sehr unterschiedliche Wellenlängenskalen beinhaltet. Das optimale Kopplungsschema für die erwarteten Plasmaparameter wurde mit einem FDTD-Code (Finite-Difference-Time-Domain) bestimmt. Da die EBW selber nicht in diesem Code enthalten sind, wurde ein BVP-Code (Boundary-Value Problem) entwickelt. Mit diesem wurde der Effekt von Teilchenstößen auf die EBW untersucht. Die Feldverstärkung an der oberen Hybridresonanz (UHR), wo die EBW an die elektromagnetischen Wellen koppeln, und die Wirkung des Magnetfelds auf die EBW konnten direkt untersucht werden. Die Ausbreitung der EBW wurde mit dem neu entwickelten Ray-Tracing-Code RiP untersucht. Die Simulationen lieferten ein klares Bild der wesentlichen Merkmale der Wellenpropagation. Erstmals wurde die Methode der Wigner-Funktion angewendet, um die Intensitätsverteilung der EBW zu berechnen. Sowohl Ray-Tracing-Rechnungen als auch Simulationen mit der Wigner-Funktion zeigten, dass das inhomogene Magnetfeld zur Fokussierung der EBW führen kann. Der Fokussierungseffekt kann in Experimenten gezielt für die lokale Heizung des Plasmas eingesetzt werden. Zusätzlich kann die Feldverstärkung in den Fokii zum parametrischen Zerfall führen.
Diese Arbeit widmete sich der Untersuchung der Wellenausbreitung. Der Schwerpunkt lag dabei auf der Simulation der Plasmawellen in der Geometrie der linearen Plasmaanlage FLiPS an der Universität Stuttgart. Messungen wurden durchgeführt, um die vorhergesagte Fokussierung der EBW an FLiPS zu untersuchen. Die erwartete Verstärkung des Signals an der UHR wurde nicht festgestellt, was entweder auf die vollständige Kollisionsabsorption der X-Mode an der UHR hinweist, oder auf die turbulenten Plasmadichteschwingungen, die die Kopplungseffizienz zu den EBW verringern.
Mit den im Rahmen dieser Arbeit entwickelten Codes steht nun eine vollständige Toolbox zur Verfügung, die die Untersuchung des gesamten Kopplungsprozesses zwischen den elektromagnetischen Wellen und den elektrostatischen Elektron-Bernstein-Wellen in einer beliebigen Plasmageometrie ermöglicht.

Abstract

The plasma generation and heating by microwaves is an important research topic in the field of controlled nuclear fusion. All modern fusion plasma devices such as Wendelstein 7-X use microwave heating. The microwave plasma-heating primarily occurs at the resonances, where the microwaves are efficiently absorbed. The heating scenario must be designed such that the microwaves can reach the resonance. When the plasma exceeds the cutoff density, the microwaves will be reflected, and the resonance becomes inaccessible. However, it is possible to perform heating by Electron Bernstein Waves (EBWs), since these electrostatic waves propagate even in overdense plasmas, unlike the electromagnetic plasma waves. EBWs cannot propagate in the vacuum and must be created through a coupling process. Both O- and X-mode can couple to EBWs.
The thesis investigates the coupling of the O- and X-mode to EBWs as well as the EBW-propagation with various numerical methods. The application of only one numerical method is not sufficient as the coupling involves very different wavelength scales. The optimal coupling scheme for the expected plasma parameters was determined using a Finite-Difference Time-Domain (FDTD) code. Since EBWs are not included in the code, a Boundary-Value Problem (BVP) code was developed. Using the BVP code, the effect of the collisions on EBWs was studied. The field amplification at the upper-hybrid resonance (UHR), where EBWs couple to the electromagnetic waves, and the effect of the magnetic field on EBWs could be directly visualized.
The propagation of the EBW was investigated using the novel ray-tracing code RiP. The ray-tracing simulations provided a clear picture of the essential features of the wave propagation. For the O- and X-mode coupling, the importance of the axial plasma inhomogeneity was shown. For the first time, the method of the Wigner function was applied to calculate the intensity distribution of EBWs. Both, ray-tracing and the Wigner function simulations showed that the inhomogeneous magnetic can cause focusing of EBWs. The focusing effect can have practical applications e.g. for controlled local heating of the plasma. Additionally, the focusing effect can cause a parametric decay due to the field enhancement in the focal regions.
In this thesis, the simulations were focused on excitation and propagation of EBWs in the geometry of the linear plasma device FLiPS located at the University of Stuttgart. Measurements were carried out to study the predicted focusing of the EBWs in the FLiPS plasma with monopole antennas. The measurements provided the density profile used in the simulations. The expected amplification of the signal at the UHR was not detected, indicating either the complete collisional absorption of the X-mode at the upper-hybrid resonance, or the turbulent plasma density oscillations that reduce the coupling efficiency to EBWs. These effects can be studied further using the developed tools since they provide a complete toolbox to study the full coupling process to EBWs in an actual experimental geometry.

List of Figures

List of Symbols

Latin symbols

Symbol	Meaning
A_B	coefficient of absorption
$\vec{B}$	magnetic field of a microwave
$\vec{B}_0$	background magnetic field
c	speed of light in vacuum
C_{eff}	conversion efficiency
$\vec{D}$	electric displacement
e	elementary charge and euler's number
$\vec{E}$	electric field of a microwave
i	imaginary unit
$I_{i,sat}$	ion saturation current
I	current
I_n	modified Bessel functions of the first order
$\vec{j}$	current density
k_0	wavenumber in vacuum
$\vec{k}$	wavevector
L	gradient length
m_e	electron mass
n_e	electron plasma density
n_0	neutral gas density
N	refractive index
P_{in}	incoming microwave power
P_{out}	outgoing microwave power
q	ratio of the the microwave frequency to the cyclotron frequency
r	radial coordinate
R	coefficient of reflection
s	normalised distance between the R-cutoff and the UHR
T	coefficient of transmission
T_e	electron temperature
v_{th}	thermal velocity
w_0	gaussian beam radius
W	Wigner function
x, y, z	cartesian coordinates
$\Delta x, \Delta y, \Delta z$	dimensions of Yee's cell
X	normalised plasma density
Y	ratio of the cyclotron frequency to the microwave frequency
Z	normalised collisional frequency

Greek symbols

Symbol	Meaning
γ	ratio of the thermal velocity to the speed of light
ϵ_0	the electric constant
$\bar{\bar{\epsilon}}$	dielectric tensor and operator
η_B	Budden parameter
θ	angle
θ	phase
θ_{opt}	optimal injection angle
Λ_D	Debye radius
μ	mean
μ_0	magnetic constant
ν	collisional frequency
ν_{ei}	electron-ion collisional frequency
ν_{en}	electron-neutral collisional frequency
ρ	charge density
ρ	gaussian beam radius
ρ_L	Larmor radius
$\bar{\bar{\sigma}}$	conductivity tensor
σ	standard deviation
σ	total cross-section
ϕ	electric potential
χ	thermal correction
$\Delta\phi$	phase difference
ω	angular frequency
ω_{pe}	plasma frequency
ω_{ce}	cyclotron frequency

Contents

Chapter 1

Introduction

When an ionised gas exhibits collective behaviour and has a small total charge, the ionised gas is called a plasma [1]. The sun, lightings are examples of the plasma occurrence in nature. The importance of plasma research is difficult to overstate, as many technological processes employ plasmas to modify surfaces, deposit films, and to sterilise food to name a few. But perhaps, the most important plasma application is the controlled nuclear fusion. When temperatures are extremely high, atoms are completely stripped off of their electrons. When these fully ionised atoms collide, they may fuse releasing energy as it occurs in the sun [1]. To create this reaction in a controlled manner in a fusion reactor, the plasma has to be held away from the reactor walls, since the plasma would damage the walls and cool down upon touching them. Inserting a plasma in a magnetic field will confine it as the particle diffusion across the magnetic field is mitigated. These plasmas are called magnetised plasmas, and they are the main subject of the research in the field of magnetic confinement fusion.

A plasma produces electromagnetic radiation, which causes the plasma to lose its energy. Thus, an energy influx is required to compensate for the energy loss and to maintain the plasma. Often the energy can be delivered in the form of an electromagnetic wave, since at certain positions in magnetised plasmas the incoming electromagnetic wave resonates with the plasma particles, leading to the absorption of the wave [2]. The absorbed energy is distributed between the particles causing an increase in the temperature and, possibly, the density.

The position where a wave is efficiently absorbed is called a *resonance*. When the plasma density reaches a critical density, the microwave radiation shone upon the plasma, instead of reaching the resonance, will be reflected. This phenomenon is known as a *cutoff*, and a plasma with this critical density called an *overdense-plasma*. Thus, reaching densities above the critical, requires either utilisation of even higher frequency microwaves, which is costly and limited by the technological progress, or coupling to the so-called Electron Bernstein Waves (EBWs). Two properties make EBWs extremely useful for the plasma heating, namely, EBWs do not have a density cutoff unlike other plasma waves, and they are strongly absorbed at the harmonics of the electron cyclotron frequency [3]. The main disadvantage of this method is that to achieve a high coupling efficiency to EBWs, the launching antenna must be carefully designed, based on the expected plasma properties. Apart from the heating, measuring EBW thermal radiation yields information about the plasma temperature [4, 5].

The EBW research has spanned many decades and the theoretically predicted EBW properties were well-established experimentally. At present, the main research interest

is concentrated around the application of EBWs for plasma heating and diagnostics [6]. The application of EBW heating is not only limited to fusion plasma physics. Another example is Electron Cyclotron Resonance Ion Sources (ECRIS), where high plasma densities and temperatures are desired to produce highly charged ions [7].
The goal of the thesis is to apply different numerical methods to fully characterise EBW propagation in the linear plasma device FLiPS, which will be presented in Ch. 3. Application of only one numerical method would not be sufficient to describe all existing plasma-wave phenomena, due to possible numerical difficulties, nature of the used approximations, or dimensionality of the considered problem. The methods that were applied to study the plasma-wave phenomena in the FLIPS plasma are the Finite-Difference Time-Domain method (FDTD) [8], the boundary value problem (BVP) [9, 10], the eikonal method [11, 12] and the Wigner function method [11, 13, 14, 12].
Before starting the numerical investigation, plasma diagnostics were installed at FLiPS to measure the electron density n_e and the temperature T_e. General experimental studies of the FLiPS plasma were carried out for different magnetic field configurations and neutral gas pressures. Using the experimentally measured plasma parameters, the wave propagation was numerically investigated. The simulations of the wave propagation in the FLiPS plasma is a complicated task, since a magnetised plasma is an anisotropic medium, which means that the plasma effect on the waves depends on the direction of the propagation. Additionally, one of the main objectives of this study was determination of the optimal coupling process of the electromagnetic waves to the EBWs. The coupling process involves very different wavelength scales. Thus, a fine numerical grid is required to resolve simultaneously all the scales. Furthermore, the presence of the resonance in the plasma complicates the simulations even further, since the wavelength becomes very short in its vicinity.
Since the FDTD is based on the cold plasma theory, and EBWs exist only in warm plasmas, a code based on the boundary-value problem in the frequency domain was developed to simulate EBWs. The main purpose of these simulations was to investigate the effect of the collisional damping on the EBWs, and whether the EBWs can be detected experimentally in the FLiPS plasma. The presented EBW full-wave simulations are valid, strictly speaking, only close to the so-called Upper Hybrid Resonance (UHR). To study EBW propagation farther from the UHR, the ray-tracing method was applied. The ray-tracing allowed to calculate the direction of the wave energy flux. The method was implemented in two codes. The first more sophisticated code is based on the full hot dielectric tensor $\epsilon_h(\omega, k)$, which includes all possible plasma waves. To verify the obtained results, a second ray-tracing code that can simulate only EBWs, was developed.
The ray-tracing approach is not able to describe wave effects such as diffraction and interference. But applying the so-called Wigner function technique and the kinetic wave equation formalism, it is possible to calculate the EBW intensity in the paraxial approximation (Sec. 6.4).
The ray-tracing simulations, as well as the Wigner function simulations, showed that EBWs are focused by the inhomogeneous axial magnetic field in the FLiPS plasma (Sec. 6.5). The effect was observed in simulations for different magnetic fields and density profiles. Based on these predictions an experiment was set up to study this effect. The measurements did not reveal a clear field amplification at the expected focal positions, which can be explained by the strong collisional damping at the UHR. Indeed, the UHR is situated at the plasm edge, where the electron temperature is low, which favours the collisional damping. Another explanation for the lack of the EBW signal is the presence

of turbulence. Turbulence causes density fluctuations that scatter the EBWs, which leads to the blurring of the regions with the amplified field. Fluctuations can be included in the simulations using the Wigner function as described in [15] in future investigations.
The structure of the thesis is shown in Fig 1.1 as a flowchart. Chapter 2 introduces the main concepts that will be used to analyse the results of the numerical simulations. The plasma parameters presented in Ch. 3 will be used in the numerical simulations carried out in chapters 4, 5, 6. In the flowchart, the chapters dedicated to the simulations are depicted as a Venn diagram to signify that only a combination of all three methods yields the complete theoretical descriptions of the wave propagation in the FLiPS plasma.

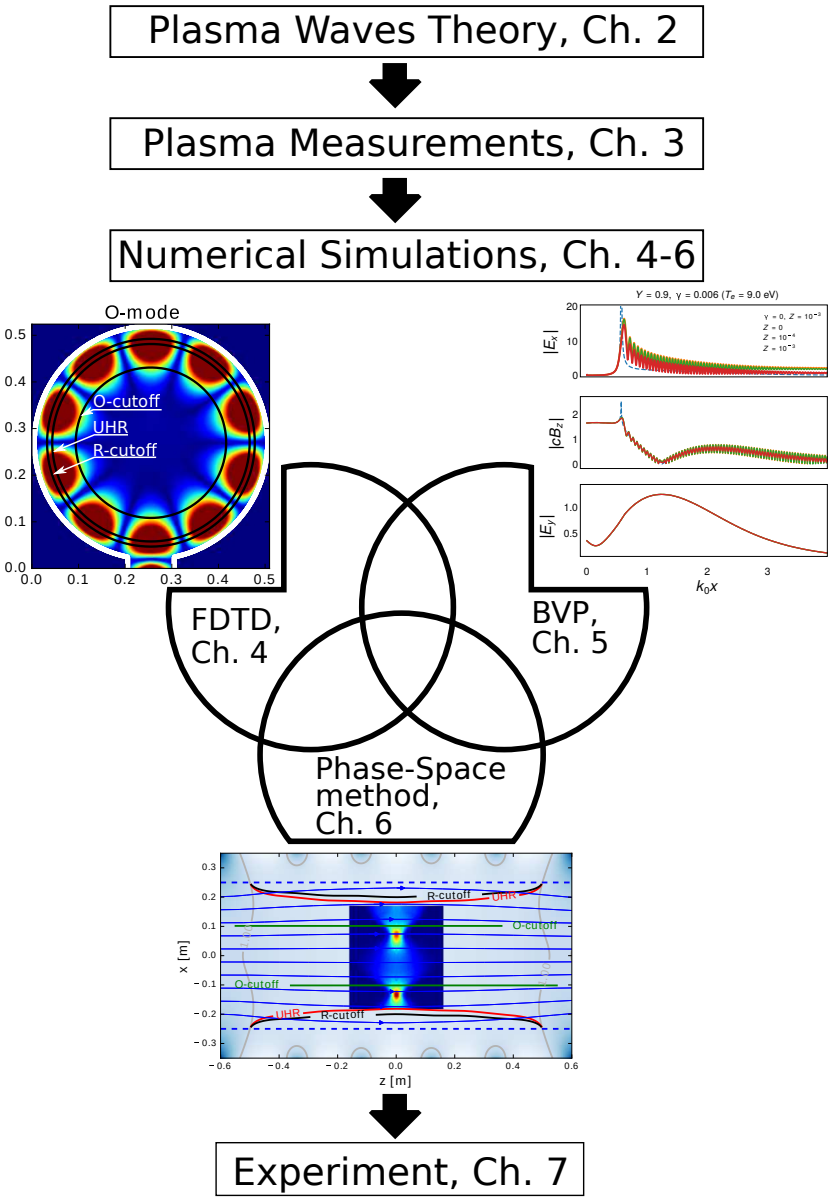

Figure 1.1: The flowchart of the thesis. The simulation-relevant plasma parameters were measured in Ch. 3. These parameters were used for the numerical simulations. The used methods are complimentary to each other allowing a full theoretical description of the plasma waves in FLiPS. The results of the simulations guided the experiment design to study EBWs in Ch. 7

.

Chapter 2

Waves in plasmas

The purpose of this chapter is to introduce the reader to the key concepts of the electrodynamics of plasmas and notations that will be used throughout the thesis. Starting from general concepts, the cold plasma model will be presented. Then the quasi-electrostatic approximation will be introduced. Using the quasi-electrostatic approximation, the Electron Bernstein Waves (EBWs) will be introduced. The possible coupling schemes to EBWs will be discussed. At the end of the chapter, the finite Larmor radius approximation will be described, which can be used to perform full-wave simulations of EBWs.

2.1 Electrodynamics of plasmas

The fundamental equations of electrodynamics are Maxwell's equations [16]

$$\begin{cases} \nabla \times \vec{B} = \mu_0 \vec{j} + \dfrac{1}{c^2}\dfrac{\partial \vec{E}}{\partial t}, & \text{Ampere's law} \\ \nabla \times \vec{E} = -\dfrac{\partial \vec{B}}{\partial t}, & \text{Faraday's law} \\ \nabla \cdot \vec{E} = \rho/\epsilon_0, & \text{Gauss' law} \\ \nabla \cdot \vec{B} = 0, & \text{absence of magnetic monopoles} \end{cases} \tag{2.1}$$

where $\vec{B}$, $\vec{E}$ are magnetic and electric fields, and $\vec{j}$ is a current density. Obviously, in vacuum $\vec{j} = 0$, but in a medium such as a plasma, the fields may accelerate charges, creating an electric current. The generated current will produce its own field, modifying the original field. If this feed-back loop is considered, when solving the equations, the problem is said to be solved self-consistently.
The relation between the current and the electric field are not given by Maxwell's equations. Instead, this relation has to be derived by considering the microscopic dynamic of the system [17]. In general, this relation can be written in an integral form as follows [3]

$$\vec{j}(\vec{r},t) = \int_V \int_{-\infty}^{t} \bar{\bar{\sigma}}(\vec{r},\vec{r'},t,t')\vec{E}(\vec{r'},t')dt'd\vec{r'}, \tag{2.2}$$

where the kernel $\bar{\bar{\sigma}}(\vec{r},\vec{r'},t,t')$ is the conductivity tensor. The form of $\bar{\bar{\sigma}}(\vec{r},\vec{r'},t,t')$ is known only in the frequency domain [18, 19]. Equation (2.2) implies that the value of the response $\vec{j}(\vec{r},t)$ depends non-locally on the applied field $\vec{E}$. The non-local behaviour in time is due to inertia of the particles and causes the frequency dispersion. The non-locality in space

is due to the thermal motion of the particles. This effect is referred to as the kinetic effect. Alternatively, the medium response can be described with the help of a dielectric tensor as usually done in the standard treatment of dielectrics. In the following, this formalism is briefly introduced. In a dielectric medium there are two types of charge carriers: bounded and free charges. Thus, the charge density in Gauss' law can be split in two parts, $\rho = \rho_{free} + \rho_{bounded}$. The function $\vec{D}$ is called the electric displacement and defined such that $\nabla \cdot \vec{D} = \rho_{free}$. This approach seems to be counterproductive, as one more unknown variable $\vec{D}$ has been introduced. This approach is useful, because often the field is sufficiently weak, and $\vec{D}$ can be assumed to be linearly proportional to $\vec{E}$, or $\vec{D} = \bar{\bar{\epsilon}} \cdot \vec{E}$. Therefore, one more relation, the so-called constitutive relation can be introduced. Now Ampere's law can be written in the following form

$$\nabla \times \vec{B} = \mu_0 \frac{\partial \vec{D}}{\partial t} \tag{2.3}$$

In a plasma *all* the charge carriers are considered to be bounded [1], therefore $\nabla \cdot \vec{D} = 0$. And, in general, $\bar{\bar{\epsilon}}$ is an integral operator due to the possible non-locality of the response

$$\vec{D}(\vec{r}, t) = \epsilon_0 \int_V \int_{-\infty}^{t} \bar{\bar{\epsilon}}(\vec{r}, \vec{r'}, t, t') \vec{E}(\vec{r'}, t') dt' \vec{r'} \tag{2.4}$$

This equation is useful for describing the electrostatic waves (Sec. 2.2).
Applying the curl operator to the left hand side of Faraday's law and using Ampere's law, the following wave equation is obtained

$$\nabla \times \nabla \times \vec{E} = -\mu_0 \frac{\partial^2 \vec{D}}{\partial t^2} \tag{2.5}$$

For a stationary and homogeneous plasma, Eq. (2.5) can be Fourier transformed

$$\vec{k} \times \vec{k} \times \vec{E} - \frac{\omega^2}{c^2} \bar{\bar{\epsilon}}(\omega, \vec{k}) \cdot \vec{E} = 0 \tag{2.6}$$

The dielectric tensor is related to the conductivity tensor as follows

$$\bar{\bar{\epsilon}}(\omega, \vec{k}) = \mathbf{I} + i \frac{\bar{\bar{\sigma}}(\omega, \vec{k})}{\epsilon_0 \omega}, \tag{2.7}$$

where $\mathbf{I}$ is a unit matrix.
Now the concept of a dispersion relation is introduced. This concept will be used throughout this thesis, because of its importance for the understanding of wave propagation phenomena. A dispersion relation relates the frequency of a wave to its wavelength in a homogeneous and stationary medium. It determines, where the wave energy can be efficiently absorbed, where different types of waves can transform into each other, and what kind of waves are allowed to propagate. Equation (2.6) can be written in the following compact matrix form

$$\bar{\bar{M}}(\omega, \vec{k}) \cdot \vec{E} = 0 \tag{2.8}$$

This matrix equation has a non-trivial solution ($\vec{E} \neq 0$) only if the determinant of the matrix $\bar{\bar{M}}$ is zero. That is, the dispersion relation is a condition for the existence of non-trivial solutions of the matrix equation

$$\det \bar{\bar{M}}(\omega, \vec{k}) = 0 \tag{2.9}$$

The determinant will depend on the choice of the model of the plasma response, which has not been specified yet. The cold plasma approximation is a model that describes both electrostatic and electromagnetic plasma waves. In this approximation, the thermal motion of the particles is completely neglected, and the plasma is characterised by only two parameters: plasma density n_e and the ambient magnetic field $\vec{B}$. In this thesis, the ion dynamic is also neglected. This simplification is justified by the fact that the ions have much higher inertia than the electrons. The electron plasma and electron cyclotron frequencies are given by

$$\omega_{pe} = \sqrt{\frac{n_e e^2}{\epsilon_0 m_e}}, \tag{2.10}$$

$$\omega_{ce} = \frac{eB}{m_e} \tag{2.11}$$

The plasma frequency ω_{pe} characterises how fast the electrons can react to the applied electric field. The cyclotron frequency ω_{ce} is the gyration frequency of an electron in a magnetic field. When the coordinate system is chosen such that $\vec{B} \parallel z$ and the wavevector $\vec{k}$ lies in $xz-$ plane, the cold plasma dielectric tensor using the Stix' notation is given by [20]

$$\bar{\bar{\epsilon}}_c = \begin{bmatrix} S & -iD & 0 \\ iD & S & 0 \\ 0 & 0 & P \end{bmatrix}, \tag{2.12}$$

where the quantities S, D and P are defined as follows

$$\begin{aligned} S &= \frac{1}{2}(R+L) \\ D &= \frac{1}{2}(R-L) \\ R &= 1 - \frac{X}{1-Y} \\ L &= 1 - \frac{X}{1+Y} \\ P &= 1 - X, \end{aligned} \tag{2.13}$$

where X and Y are defined as

$$X = \frac{\omega_{pe}^2}{\omega^2} \tag{2.14}$$

$$Y = \frac{\omega_{ce}}{\omega}, \tag{2.15}$$

which will be used throughout the thesis. In the case of the cold plasma, the determinant of the matrix $\bar{\bar{M}}$ is given by the following polynomial of the 4th degree

$$\begin{aligned} &An^4 - Bn^2 + C = 0 \\ &A = S\sin^2\theta + P\cos^2\theta \\ &B = RL\sin^2\theta + PS(1+\cos^2\theta) \\ &C = RPL \end{aligned} \tag{2.16}$$

Note that the cold dielectric tensor does not depend on the wavevector as the thermal motion of the particles is neglected.
Equation (2.16) has four different solutions. But in total, there are two different modes, as the waves can propagate backwards and forwards. These two modes are called an Ordinary mode (O-mode) and an Extraordinary mode (X-mode). For certain plasma parameters the refractive index becomes infinite or zero. The positions where $N \to \infty$ are resonances and $N = 0$ are cuttoffs. Analysis of Eq. (2.16) shows that in a magnetised plasma there exists a cutoff whenever $C = 0$. Thus, cutoffs occur at $P = 0$, $R = 0$ and $L = 0$. A resonance occurs when $A = 0$, which is called the generalised resonance condition [20]. For the perpendicular propagation a resonance occurs for $S = 0$, which is called the Upper Hybrid Resonance (UHR).
The cold dispersion relation (2.16) can be re-written in another useful form given by the Altar-Appleton-Hartree (AAH) dispersion relation

$$N^2 = 1 - \frac{2X(1-X)}{2(1-X) - Y^2\sin^2\theta \pm Y\sqrt{Y^2\sin^4\theta + 4(1-X)^2\cos^2\theta}} \tag{2.17}$$

In this form, the dispersion relation explicitly relates the magnitude of the refractive index vector to its direction. The + and − signs correspond to O- and X-modes. An example of the refractive surfaces is shown in Fig. 2.1.
Note that the O-mode propagates only for $X < 1$. For the X-mode, there is a forbidden zone, where the wave is always evanescent. For the perpendicular propagation, this zone lies between R-cutoff and UHR. The solution that propagates until the R-cutoff is called the Fast X-mode (FX-mode) and the solution after the UHR is the Slow X-mode (SX-mode). This terminology reflects the fact that the phase velocity of the SX-mode is smaller the speed of light in vacuum. For the parallel propagation another terminology is often used. As shown in Fig. 2.1, for the parallel propagation the O-mode is connected to the X-mode at $X = 1$, forming a continuous refractive surface. This new surface represents the L-mode, and the mode that propagates until the R-cutoff is the R-mode. If the thermal motion cannot be neglected, the dielectric tensor becomes extremely complicated, and some approximation is usually necessary. One of them is the quasi-electrostatic approximation, which is covered in the next section.

2.2 Quasi-electrostatic waves

In the quasi-electrostatic approximation, the electric field is assumed to be the gradient of a scalar function ϕ

$$\vec{E} = \vec{\nabla}\phi \tag{2.18}$$

Doing that simplifies the vector problem to a scalar one. Replacing the electric field in Gauss' law and assuming a homogeneous plasma, the following equation is obtained

$$\begin{aligned} &\nabla \cdot \bar{\bar{\epsilon}}(\omega, k)\vec{\nabla}\phi = 0, \\ &(\vec{k} \cdot \bar{\bar{\epsilon}} \cdot \vec{k})\phi = 0 \end{aligned}$$

And the quasi-electrostatic dispersion relation for the plasma waves is given by:

$$k_x^2\epsilon_{xx} + 2k_xk_z\epsilon_{xz} + k_z^2\epsilon_{zz} = 0 \tag{2.19}$$

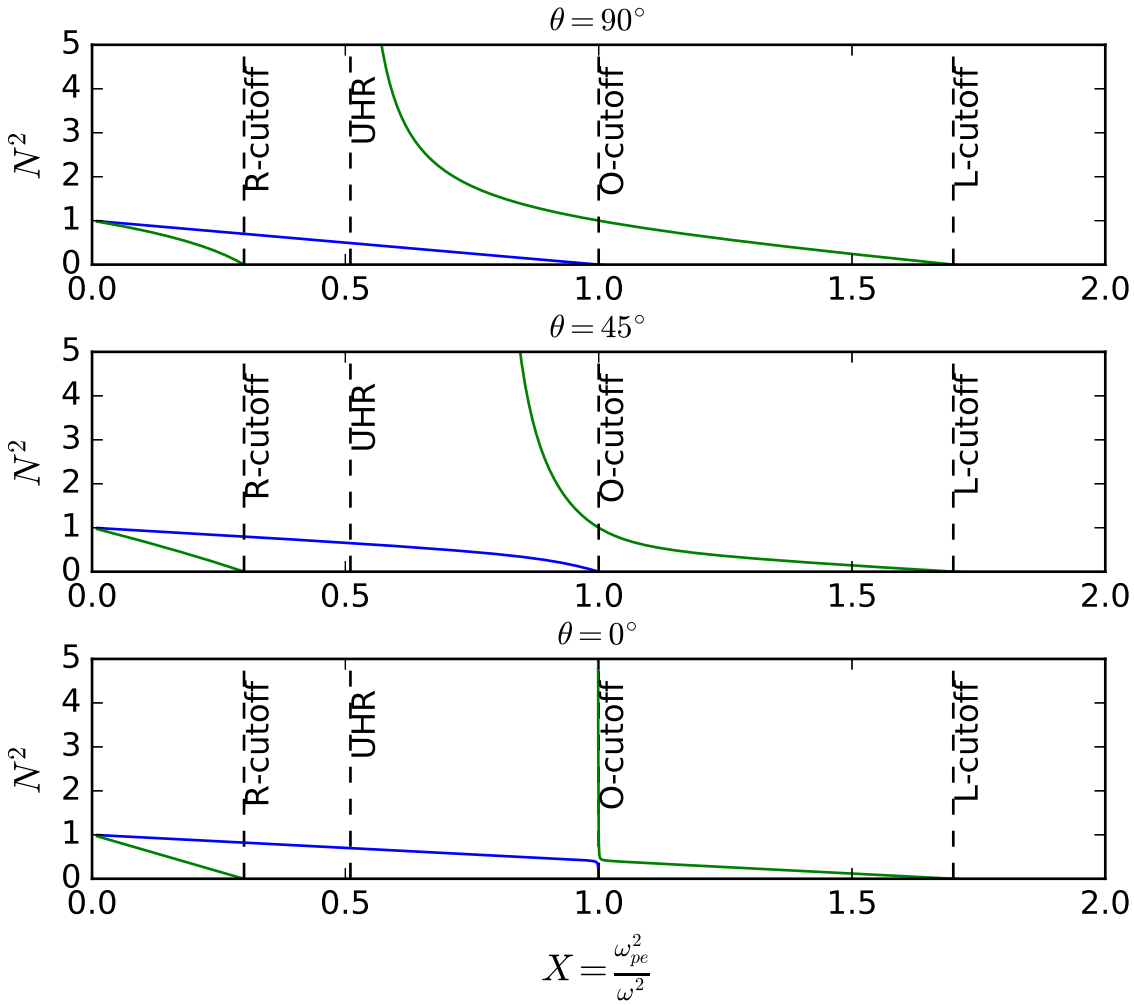

Figure 2.1: Refractive indices of O- and X-mode for perpendicular ($\theta = 90°$), oblique ($\theta = 45°$) and parallel propagation ($\theta = 0°$) with respect to the background magnetic field. The blue and green lines correspond to the O- and X-mode, respectively.

In the case of a cold plasma, $\bar{\bar{\epsilon}}$ is given by Eq. (2.12), and the following dispersion is obtained

$$Sk_x^2 + Pk_z^2 = 0 \tag{2.20}$$

Thus, the electrostatic waves propagate in a magnetised plasma at the angle θ_{res} given by

$$\tan^2 \theta_{res} = -\frac{P}{S}, \tag{2.21}$$

where P and S are given by Eqs. (2.13). It can be shown [20] that in a cold magnetised plasma the antenna will radiate the waves in the directions given by θ_{res}, forming the so-called resonance cone as shown in Fig. 2.2.
Figure 2.3 shows the refractive index surfaces for $P > 0$ and $S < 0$ obtained from the AAH dispersion relation given by Eq. (2.17). The closed round surface belongs to the O-mode. The open surface describes the SX-mode. As the wave vector on the SX-mode surface approaches the resonant angle θ_{res} the refractive index magnitude becomes infinite, indicating the resonance. It should be kept in mind that this dispersion relation does not describe a new type of waves. Indeed, Eq. (2.20) is nothing else but the angular resonance condition that can be obtained from the Altar-Appleton-Hartree dispersion relation. It implies that the quasi-electrostatic approximation is applicable in the case of a

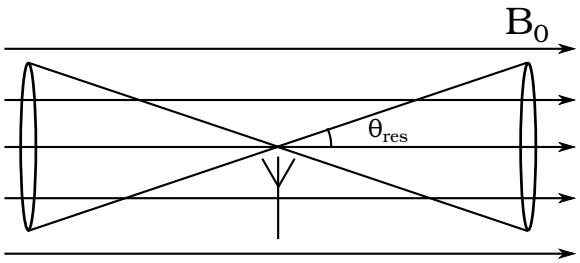

Figure 2.2: A small antenna inserted in a magnetised plasma radiates predominantly along the surface of a cone with the opening angle θ_{res} given by (2.21). Thus, the plasma can significantly change the radiation pattern of an antenna. The waves that propagate along the surface are electrostatic, similarly to EBWs.

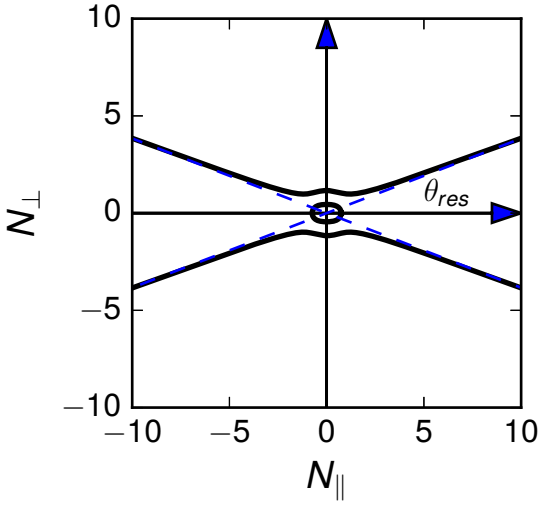

Figure 2.3: The cold plasma refractive index surfaces for the O- and X-modes for $P > 0$ and $S < 0$. The O-mode refractive index has a closed oval surface and the X-mode refractive index surface is open. The wings of the surface is the resonance cone with the opening angle θ_{res}.

large refractive index N.
Having introduced the quasi-electrostatic approximation and the necessary concepts, Electron Bernstein Waves will be introduced in the next section.

2.3 Electron Bernstein Waves

The Electron Bernstein Waves are quasi-electrostatic waves and exist only in magnetised plasmas. An intuitive explanation is depicted in Fig. 2.4. Their existence was first pre-

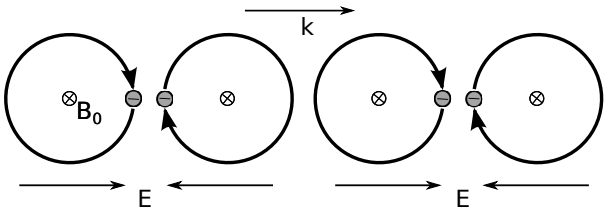

Figure 2.4: Illustration of how the EBWs are formed. As the electrons collectively gyrate in the ambient magnetic field, the electric field is periodically perturbed, forming the wave field. The wavelength of EBWs is of the order of the Larmor radius, and it is a longitudinal wave.

dicted theoretically by Ira B. Bernstein in his famous article of 1958 [21], and then was confirmed experimentally [22, 23]. These waves do not have a high-density cutoff, are not Landau damped for the exact perpendicular propagation, and resonate at the harmonics of the electron cyclotron resonance. These properties make them a good candidate for

plasma heating [24, 6].
In the case of perpendicular propagation, the diagonal component of the plasma dielectric tensor $\epsilon_{xx} = 0$ as follows from Eq. (2.19), where ϵ_{xx} is given by [20]

$$\epsilon_{xx} = 1 - Xq^2 \sum_{n=1}^{N=\infty} \frac{2e^{-\lambda} I_n(\lambda)}{\lambda} \frac{n^2}{q^2 - n^2}, \tag{2.22}$$

where $\lambda = \frac{1}{2}(N_\perp \gamma q)^2$, $q = \frac{\omega}{\omega_{ce}}$, $\gamma = \frac{v_{th}}{c}$ and I_n are the modified Bessel functions of the first order [25].
The EBW dispersion relation is shown in Fig. 2.5. The solutions of the dispersion rela-

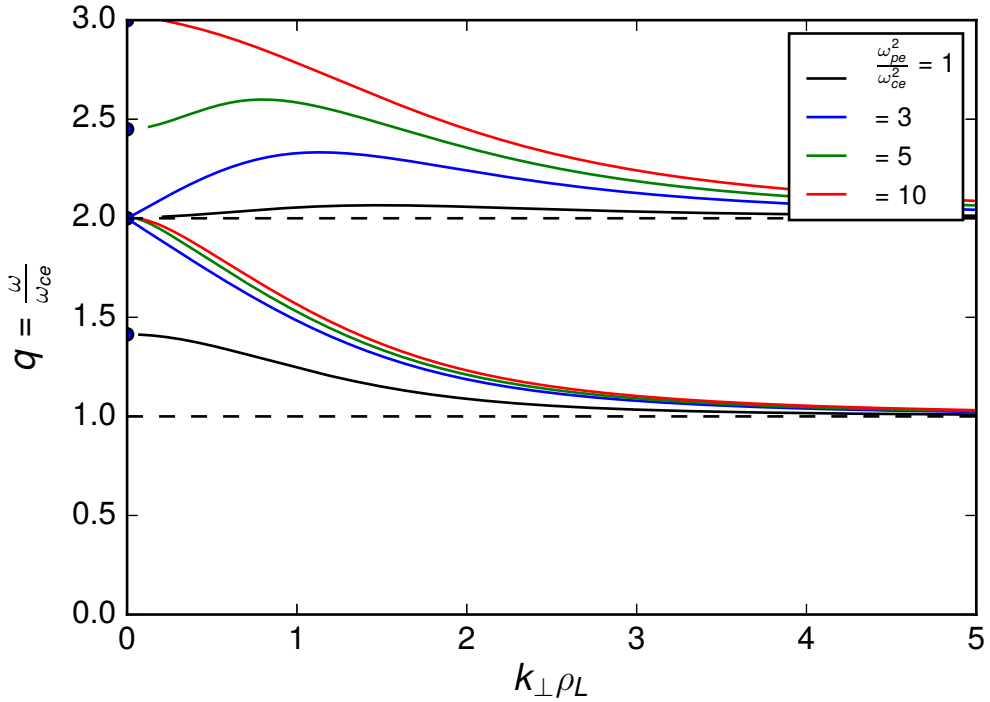

Figure 2.5: The EBW dispersion relation for the almost perpendicular propagation for bands $1 < q < 2$ and $2 < q < 3$ for different values of the parameter $\omega_{pe}^2/\omega_{ce}^2$. The bands correspond to the fundamental and the first EBW harmonics, respectively.

tion were obtained using the ray-tracing method described in Ch. 6. To be able to use Eq. (2.22) in calculations, the sum was truncated at $N = 10$. It should be noted that the solutions shown in Fig. 2.5 were obtained in the quasi-electrostatic approximation, which can be violated at the UHR, where the EBWs can transform into the usual electromagnetic plasma waves. The solutions lie in the frequency bands formed by the harmonics of the cyclotron resonance. There are propagating solutions in each frequency band with the exception of $0 < q < 1$. The solutions are plotted for fixed values of the parameter $\alpha = Xq^2 = (\frac{\omega_{pe}}{\omega_{ce}})^2$. To understand better how the solutions behave, consider the band $1 < q < 2$. In this band, the UHR exists for $0 < \alpha < 3$. If $\alpha = 3$ the upper hybrid resonance coincides with the second harmonic resonance $q = 2$ and all the other solutions in this band will originate from this point. In the next band $2 < q < 3$ for $1 < \alpha < 3$ the solution will originate at the second harmonic resonance. For $\alpha > 3$ in this band, there is UHR until $\alpha = 8$, which coincides with the third harmonic of the cyclotron resonance. The EBWs can be excited through the coupling schemes, which will be presented in the following.

2.3.1 The first scheme — O-X conversion

One of the schemes to excite EBWs in a magnetised plasma is a three-step process, where the incoming O-mode launched from the vacuum side converts into the SX-mode upon the reflection at the O-cutoff [26]. This process received attention not only due to the problem of heating of the fusion plasmas, but also due to the importance for the ionospheric research. The O-X conversion explains the signal tripling that occurs when an O-mode is reflected from the dense ionospheric plasma [27, 28].
The coupled SX-mode propagates outwards, towards the UHR, where in the cold plasma approximation the SX-mode has a resonance. If the thermal effects are included the SX-mode cannot reach the UHR and instead will be reflected as the EBW. In general, the efficiency of the coupling is defined as

$$C_{eff} = \frac{P_{in} - P_{out}}{P_{in}}, \tag{2.23}$$

where P_{in} and P_{out} are the incoming and outgoing energy fluxes. In the case of the O-X conversion, these fluxes are carried by the O-mode. The coupling to the EBWs is mostly determined by the coupling of the incoming O-mode to the SX-mode at the O-cutoff. The conversion is efficient, when energy from one mode can flow into the other, which happens when the refractive indices of the two waves have close values at the same point in space. The AAH dispersion relation (2.17) shows that the X- and O-modes have the same refractive indices whenever the square root in the denominator vanishes. It occurs only if both $X = 1$ and $\theta = 0$. Thus, setting $\theta = 0$ the AAH dispersion relation simplifies to the following form

$$N^2 = 1 - \frac{2X(1-X)}{2(1-X) \pm 2Y|1-X|} \tag{2.24}$$

For the O-mode approaching the limit from the low-density side leads to

$$\lim_{X \to 1^-} N^2 = \frac{Y}{1+Y}.$$

For the X-mode approaching the limit from the high-density side leads to

$$\lim_{X \to 1^+} N^2 = \frac{Y}{1+Y}.$$

Assuming a homogeneous plasma in the z-direction, the optimal injection angle at which the maximum conversion efficiency is expected, is given by

$$\cos^2 \theta_{opt} = N^2_{z,opt} = \frac{Y}{1+Y}. \tag{2.25}$$

Figure 2.6 demonstrates the ideas presented above. For the optimal injection angle the O-mode is directly connected to the SX-wave. For $\theta < \theta_{opt}$ the O-mode reflects before reaching the $X = 1$. If the the injection angle is larger than the optimal value, the SX-mode starting point is shifted towards the higher density. In the following, examples of the O-X conversion in the 2D plasma geometry will presented.
The simulations were performed with the FD3D full-wave code (see Sec. 4.3 for details). The incoming O-mode at 2.45 GHz was initiated as a Gaussian beam. As a reference, the Gaussian beam propagation in vacuum is shown in Fig. 2.7. Along the r-axis the beam shape is given by the Gaussian function, and the beam width at the waist is characterised

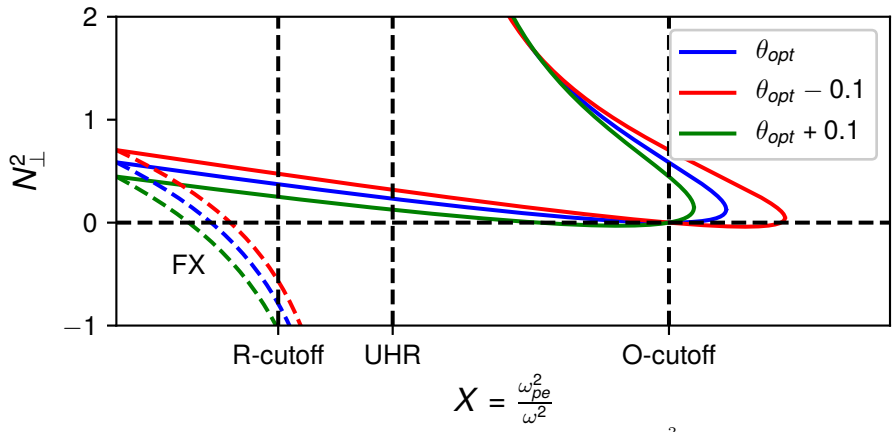

Figure 2.6: Dependency of the perpendicular refractive index $N_\perp^2$ on $X = \frac{\omega_{pe}^2}{\omega^2}$. The colors correspond to different launching angles at the vacuum side $X = 0$. The dashed lines correspond to the FX-mode which is evanescent after the R-cutoff. The solid lines correspond to the O- and SX-mode. The waves become evanescent whenever $N_\perp^2 < 0$. The O-mode and SX-mode, in general, are separated by the evanescent region. When the O-mode is launched at the optimal angle, the evanescent region vanishes and the modes are efficiently coupled. A similar plot is shown in Fig. 6.2, where the mode labelling is discussed.

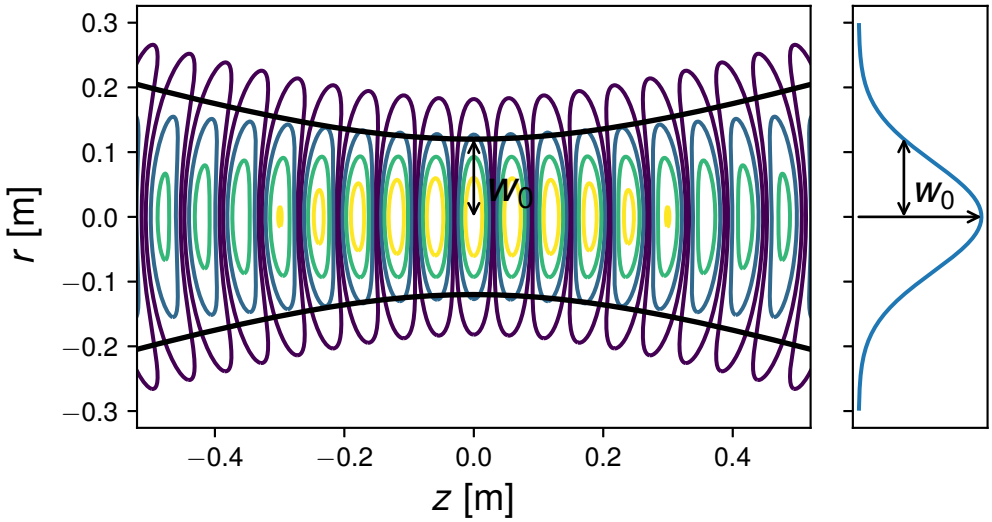

Figure 2.7: Left: demonstration of the Gaussian beam propagation at 2.45 GHz in vacuum. The beam is initiated at $z = 0$ with the initial beam waist $w_0 = 0.12$ m. The contours show the levels of the electric field $E > 0$. The beam radius is shown by the black thick curve. Right: the beam cross-section at $z = 0$

by the beam waist radius w_0. At the distance $r = w_0$, the field strength is $1/e$ of the field at the center of the focus ($r = 0$). Generally, the plasma waves are elliptically polarised. To excite the O-mode, the magnetic B_y and the electric E_y components are simultaneously excited at the antenna plane, such that their ratio is given by

$$\frac{E_y}{B_y} = -\frac{Y \sin\theta - \Gamma}{2\cos\theta} \exp i\frac{\pi}{2}, \tag{2.26}$$

where

$$\Gamma = \sqrt{Y^2 \sin^4\theta + 4\cos^2\theta}.$$

This relation can be derived with a little algebra by combining Eq. (2.6) and Eq. (2.17). The fields involved in the O-X conversion can be also found analytically in 1D geometry for shallow density profiles [29].

Figures 2.8 and 2.9 show simulations of the O-mode propagation for the injection angles θ_{opt} and $\theta > \theta_{opt}$, respectively. The simulations were performed in a magnetised plasma

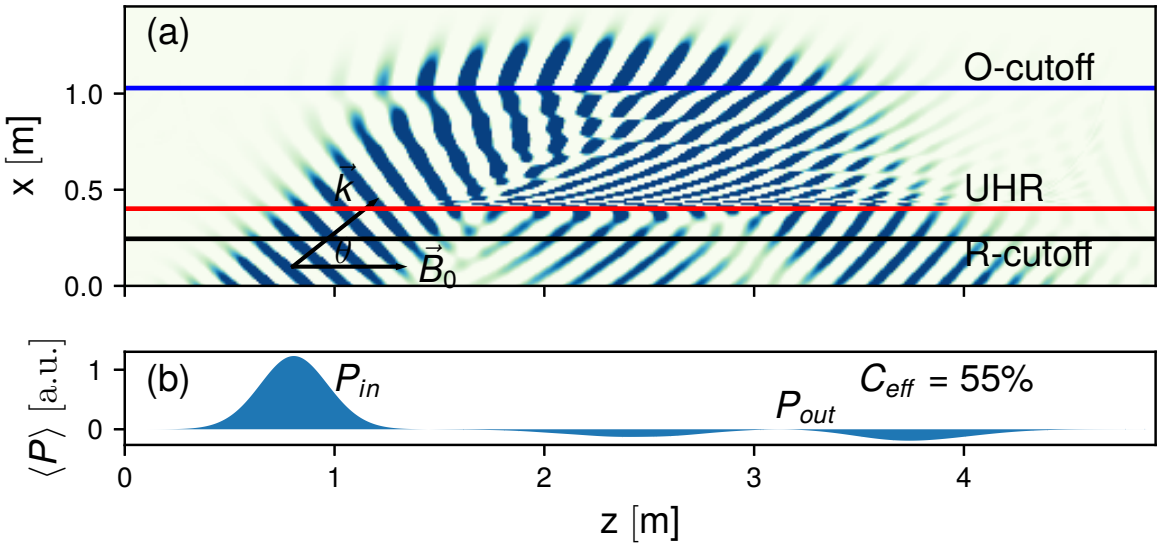

Figure 2.8: (a): Propagation of the O-mode launched at θ_{opt} in an inhomogeneous magnetised plasma with $\nabla n_e \parallel x$ and $Y = 0.8$. The initial beam waist radius $\omega_0 = 2\lambda$. (b): Poynting flux at the antenna plane $x = 0$. Positive values correspond to the incoming flux and the negative to the outgoing flux.

with a linearly increasing plasma density along the x-axis. As expected, the O-mode is not affected by the R-cutoff and the UHR. The wave propagates through the plasma until the O-cutoff, where the coupling to the SX-mode occurs. The excited SX-mode propagates towards the UHR, where it is dissipated by collisional damping. Collisional damping is included in the FDTD simulations as shown in Eq. (4.4). For the non-optimal angle the value of $C_{eff} = 13\%$ is lower than in the case of the injection at θ_{opt}.
As pointed out in [30], the conversion efficiency of the O-X scheme depends on the beam divergence and thus on the beam waist w_0 of the injected O-mode beam. Only the central part of the beam propagates at the optimal angle, because of the finite beam width. The effect of the beam size on the conversion can be clearly seen in Fig. 2.8 (b). The figure

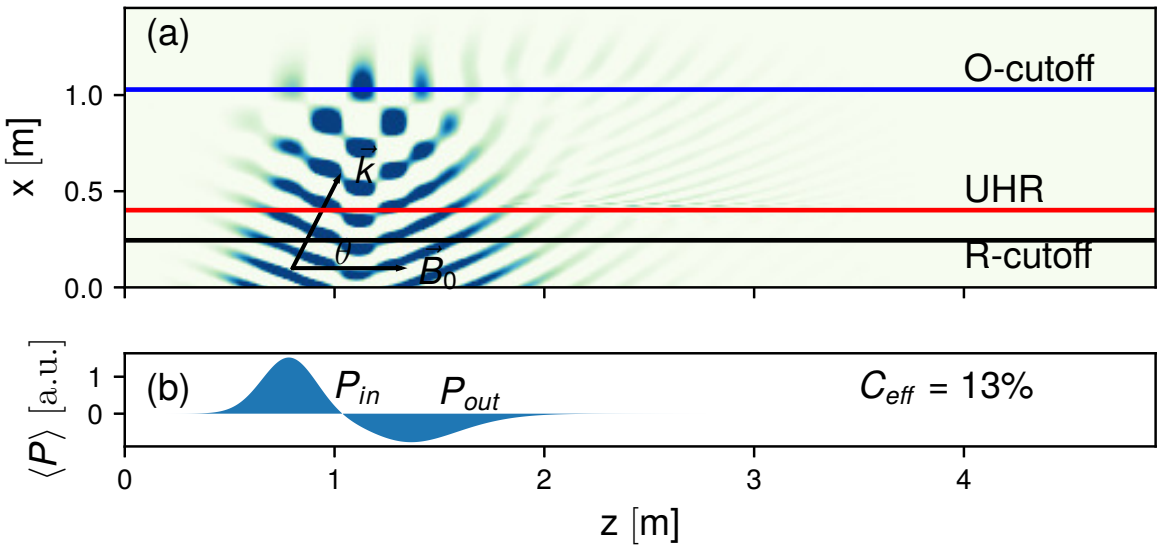

Figure 2.9: Same as Fig. 2.8, but for $\theta > \theta_{opt}$.

shows the Poynting flux of the incoming O-mode at the optimal angle and the outgoing unconverted O-mode. The outgoing power flux demonstrates that only the central part

of the O-mode beam angular pattern was perfectly converted into the SX-mode. Analytically, the conversion efficiency C_{eff} of the O-X conversion is given by the Mjølhus formula [31]

$$C_{eff} = \exp(-\pi k_0 L \left(\frac{Y}{2}\right)^2 (2(N_z - N_{z,opt})^2(1+Y) + N_y^2)), \tag{2.27}$$

where L is the density-gradient length at the O-cutoff. In general, L provides a typical scale of the inhomogeneity and is given by

$$L = \left(\frac{dX}{dr}\right)^{-1} X \tag{2.28}$$

Figure 2.10 (left) illustrates C_{eff} as a function of L for fixed values of N_z.

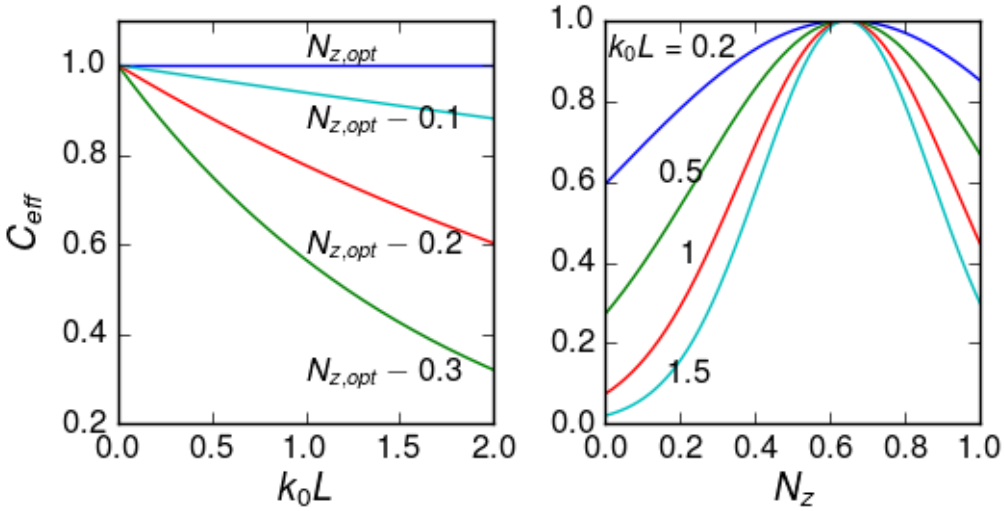

Figure 2.10: The conversion efficiency of an O-mode into the SX-mode according to the Mjølhus formula 2.27. Left: C_{eff} for different N_z as a function of the normalised density-gradient length k_0L. Right: C_{eff} for fixed k_0L as a function of N_z. For the smaller values of k_0L there exists a wider range of injection angles with high conversion efficiency. However as k_0L becomes smaller the approximation that was used to derive the Mjølhus formula may not be applicable and tunnelling of the SX-mode through the UHR towards the lower plasma density will significantly decrease C_{eff}.

The Mjølhus formula implies that for $N_z = N_{z,opt}$, the conversion efficiency does not depend on k_0L, and $C_{eff} = 1$ for $k_0L = 0$. On the right-hand side of Fig. 2.10, C_{eff} is plotted as a function of N_z for fixed values of k_0L. For the smaller values of k_0L the conversion efficiency is higher over a broader range of N_z. From the Mjølhus formula, it can be concluded that small k_0L is beneficial for the conversion. However, the Mjølhus formula was derived assuming a shallow density gradient L at the O-cutoff. For small values of k_0L, C_{eff} will be smaller than predicted by the Mjølhus formula due to the SX-mode back tunnelling as described in Sec. 5.1.2. Generally, the exact value of C_{eff} has to be found using numerical methods such as the boundary value problem method or the Finite-Difference Time-Domain method. Calculations of C_{eff} in the FLiPS plasma using the FDTD method are presented in Ch. 4. For the case of the linear steep density profile, C_{eff} is calculated in Ch. 5.

2.3.2 The second scheme — direct FX-SX coupling

The second scheme is the direct FX-SX coupling scheme. The FX-SX coupling is a tunnelling process that was studied by Budden [27]. He considered the problem of the

wave propagation in a medium with the refractive index given by

$$N^2 = \frac{\beta}{x} + \frac{\beta^2}{\eta^2}, \tag{2.29}$$

where β and η are constants that determine the position of the cutoff, where $N = 0$. This expression approximately describes the refractive index of an X-mode [32]. The main feature of this refractive index model is that a wave propagating from left to right will encounter a cutoff at $x = -\frac{\eta^2}{\beta}$, and then a resonance at $x = 0$ as shown in Fig. 2.11. For an X-mode, the cutoff corresponds to the R-cutoff and the resonance to UHR. The

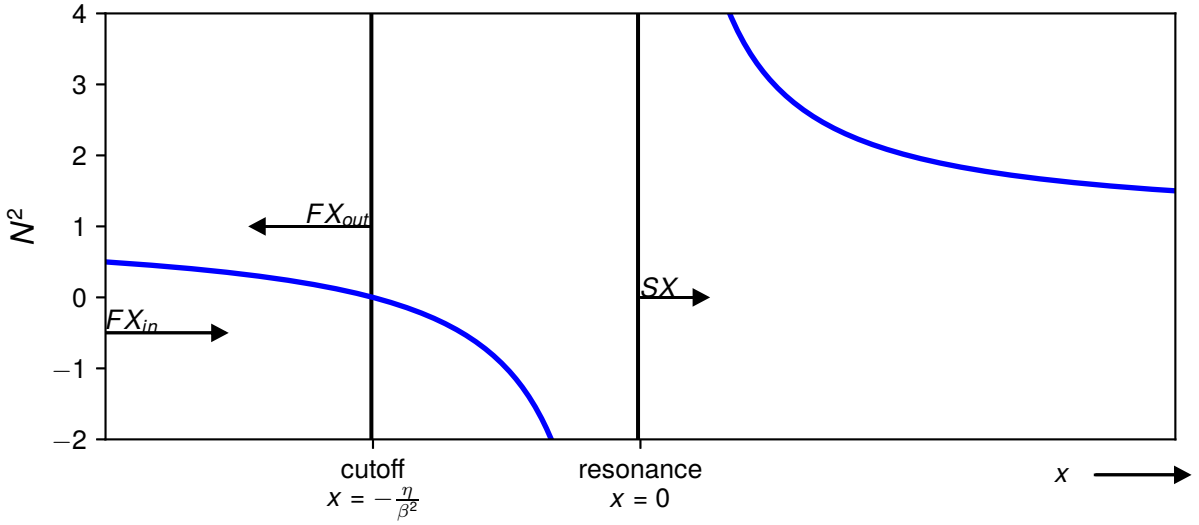

Figure 2.11: Refractive index N^2 used in the Budden analysis. A wave propagating in a medium with such a refractive index will encounter a cutoff and a resonance.

absorption A_B due to the resonance is given by

$$A_B = e^{-\pi s_0}(1 - e^{-\pi s_0}), \tag{2.30}$$

where $s_0 = k_0 x$ is the normalised distance between the cutoff and the resonance. The direct FX-XS coupling belongs to a class of tunnelling problems, often encountered in plasma physics. The term tunnelling refers to the fact that two branches of the same mode are coupled, unlike in the mode conversion case, where two different modes are coupled [11].

The Budden analysis assumes that only one cutoff is present. However, an X-mode has additionally the L-cutoff, when the plasma density is high enough. The presence of the L-cutoff significantly modifies the tunnelling efficiency predicted by the Budden theory [32]. Consider the density profile shown in Fig. 2.12. The incoming FX-mode, propagating towards higher density, encounters the R-cutoff, where it splits into a transmitted and a reflected wave. The transmitted part tunnels through the evanescent region between the R-cutoff and the UHR, coupling to the SX-mode. The SX-mode reflects at the L-cutoff and propagates towards the lower density. Then part of it will be absorbed at the UHR, and some energy will leave the plasma in the form of the FX-mode. One can expect perfect coupling efficiency, when the reflected FX-mode and back tunnelled FX-mode interfere destructively. The coupling efficiency C_{FX-SX} is given by

$$C_{FX-SX} = 4e^{-\pi\eta_B}(1 - e^{-\pi\eta_B})\cos^2(\frac{\phi}{2} + \theta), \tag{2.31}$$

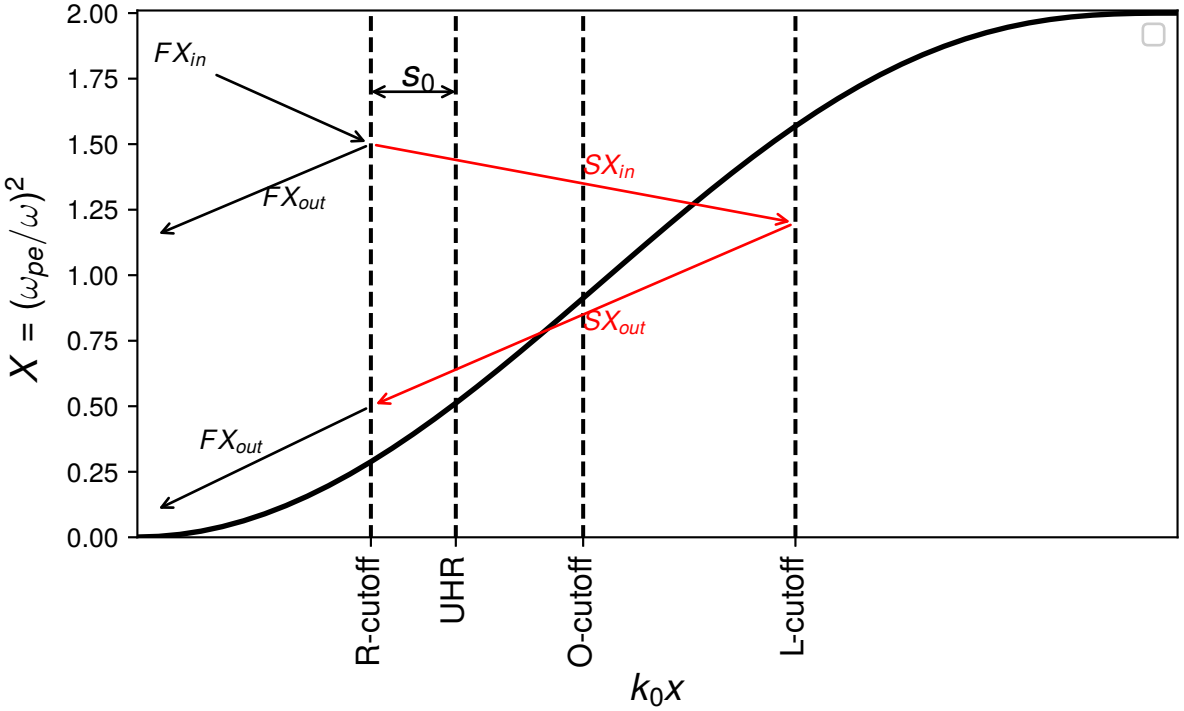

Figure 2.12: Sketch of the direct FX-SX coupling process and the RL-resonator. The incoming FX-mode partially reflects at the R-cutoff. The transmitted part is a SX-mode. The wave reflects at the L-cutoff and is partially absorbed at the UHR and partially transmitted as a FX-mode.

where in the case of $L_B \gg L$, where L_B and L are the magnetic field and the density characteristic lengths, the Budden parameter η_B is given by

$$\eta_B = \frac{Yk_0L_n}{\alpha}(\sqrt{1-\alpha^2}-1)^{\frac{1}{2}}, \tag{2.32}$$

where $\alpha = \frac{\sqrt{1-Y^2}}{Y}$. The phase factor $\cos^2(\frac{\phi}{2}+\theta)$ in Eq. (2.31) can significantly modulate the conversion efficiency as shown in Sec. 5.1. If the density is not high enough and the L-cutoff is not present inside the plasma, the maximum conversion efficiency according to the Budden analysis is 25 %.

2.3.3 Plasma dispersion relation in the case of finite electron temperature

Up to now, only the cold plasma approximation has been considered. Here, the behaviour of the refractive index of the SX-mode is discussed when the thermal effects are included in the plasma model. The SX-mode refractive index will be calculated with three different approaches. Using the obtained results, the applicability range of the approximations will be discussed.

The most general and complicated approach is based upon the full hot dielectric tensor $\bar{\bar{\epsilon}}_h$. No approximations are made, which results in extreme complexity of $\bar{\bar{\epsilon}}_h$. Its expression can be found in [20], or in any other advanced plasma physics book. Within this approach the SX-mode and the EBWs are described by the same refractive index surface. When the electromagnetic effects are not important, the quasi-electrostatic approximation can be used. This approximation is limited to only short wavelength waves with vanishing magnetic field component. Its clarity makes the study of the EBWs a more tractable task.

But the SX-mode cannot be, in general, described within this approach.
Another approach can be used when T_e is small. In this case, kinetic effects can be treated as a small correction to the cold plasma dielectric tensor. This approach is useful for the full-wave simulation of the EBWs and is discussed in detail in Sec. 5.3. Figure 2.13 shows the refractive indices of the SX-mode and the EBWs obtained using the methods described above for two different background magnetic field strengths. The thermal cor-

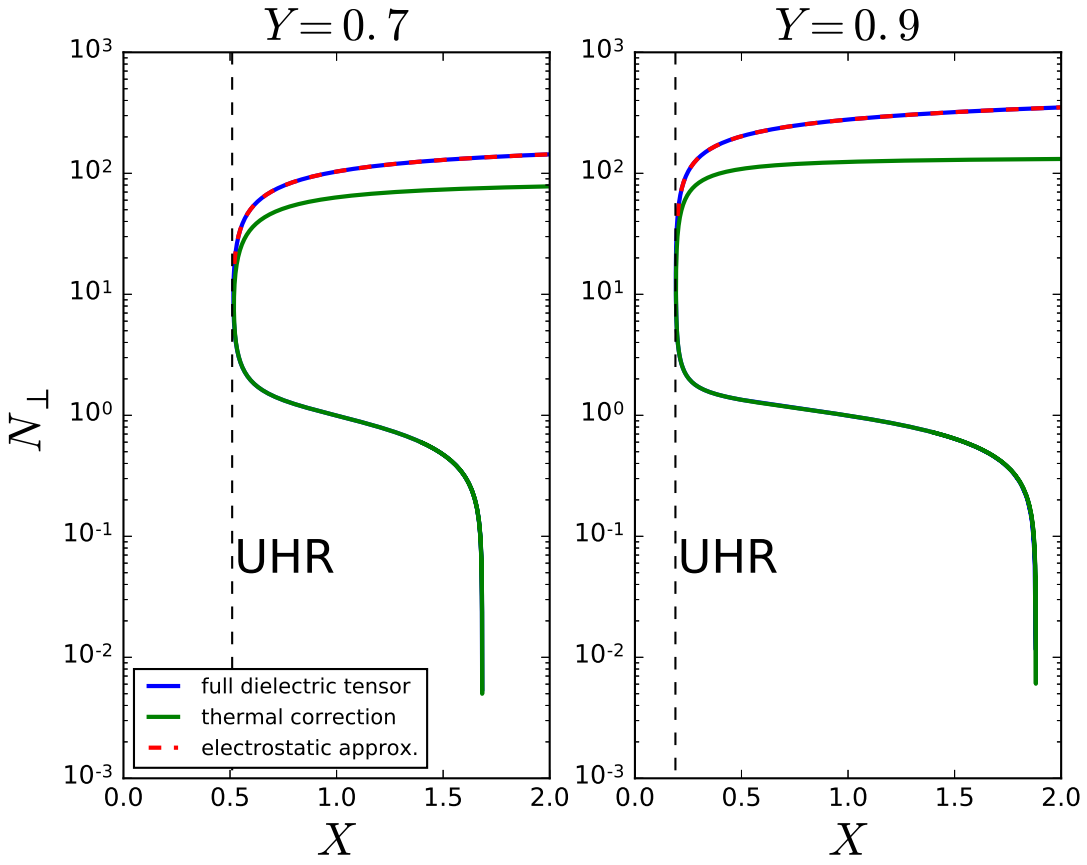

Figure 2.13: Perpendicular refractive index calculated for three different approximations as a function of $X = \frac{\omega_{pe}^2}{\omega^2}$. $N_\perp$ based on the hot dielectric tensor was calculated using a ray-tracing code described in Sec. 6.3.1. This approach can be used to find $N_\perp$ for any density and electron temperature. The large values of $N_\perp$ can be also found from the electrostatic approximation. The thermal correction approximation matches the exact values only in the UHR vicinity.

rection approach is in good agreement with the dispersion relation based on the full hot dielectric tensor only in the UHR vicinity. As the density increases the thermal correction approximation will underestimate the refractive index. An excellent agreement can be seen between the full hot dielectric tensor and the quasi-electrostatic approximation for large values of the refractive index.

Chapter 3

The linear experiment FLiPS

3.1 Introduction

This chapter introduces the linear flexible plasma device FLiPS, where EBW experiments were carried out. FLiPS can be operated as a magnetic mirror plasma device with arbitrary mirror ratios $1 < B_{max}/B_{min} < 3.9$. In magnetic mirror devices, at the vessel ends the background magnetic field reaches its maximum B_{max}. The inhomogeneous magnetic field creates a force exerting on the charged particles in the direction of the lower magnetic field. This force repels the particles from the ends of the vessel, back into the confined plasma region within the low magnetic field B_{min}. Plasma dynamics in such devices was previously studied in depth in relation to the controlled fusion [33]. Heating scenarios in a device similar to FLiPS were reported in [34].
In this chapter, the base plasma heating system will be described as well as the plasma diagnostics that were used to measure the plasma density n_e and the electron temperature T_e. This chapter does not deal with the EBW measurements, but only with the general

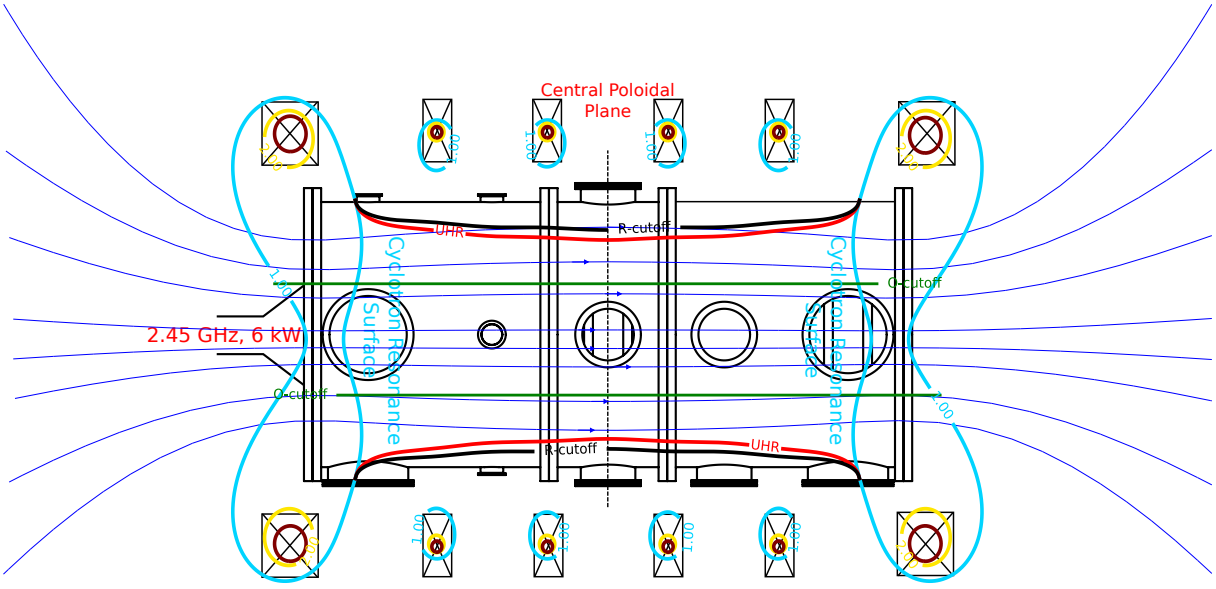

Figure 3.1: A schematic of the experimental set up. The presented calculated magnetic field configuration is created by the current of 500 Amps and 320 Amps in the outer and inner coils respectively. Towards the end of the vessel the magnetic field is stronger, which is beneficial for the axial plasma confinement.

experimental investigation of the base plasma, where later the EBW experiments were carried out. The optimal neutral gas pressure and the magnetic field configurations that

produce a stable and dense plasma will be described. For some magnetic field configurations and neutral gas pressures, the plasma produced hazardous levels of X-ray emission. The X-ray emission risk could not be completely mitigated and, in general, safety measures are always required when working with magnetic mirror devices [7]. In this thesis, plasma configurations that produced strong X-ray emission were avoided.
The plasma produced by the main heating system served as the base plasma, in which the wave propagation could be studied. An additional plasma heating system was also used, and will be referred to as the auxiliary heating. The waves launched into the base plasma by this auxiliary heating system will be the main objective of the numerical as well as experimental investigations in the next chapters. For the measured plasma parameters, the Mjølhus and the Budden analytical models (see Eqs. (2.27) and (2.31)) were applied to predict, which auxiliary heating configuration is preferable to couple to the EBWs. Using these parameters, the effect of the collisional and Landau damping on the EBW propagation was calculated. In the chapters dedicated to the EBW simulations, these parameters will be used to perform the numerical analyses.

3.2 Magnetic field configuration and heating system

Figure 3.1 depicts the FLiPS vessel with an overlaid example of the magnetic field configuration. The vessel length was 1.16 m and the diameter $D_{FLiPS} = 0.52$ m. The magnetic field was created by the magnetic field coils constructed for FLiPS with the diameter 0.66 m. The two outer coils had twice more windings than the inner four coils. Each outer coil had its own power supply that produced the current up to 500 Amp. The inner coils were connected in series to a high-current system. The high-current system can produce current outputs much higher than the power supplies. In practice, the inner coils current was never set to more than 500 Amp, since it would lead to the loss of the axial plasma confinement.
Since the outer coils were controlled independently from each other and from the inner coils, a variety of the magnetic configurations with different magnetic field ratios as well as asymmetric configurations could be produced. All the coils were water-cooled, which allowed a continuous operation. The routinely used magnetic field configuration was created by 500 Amp in the outer coils and 320 Amp in inner coils. This magnetic field configuration is shown in Fig. 3.1.
The main microwave heating system that was used to produce the base plasma is shown in Fig. 3.2 (Left). The microwave was produced by an adjustable power $0 < P \leqslant 6$kW, 2.45 GHz magnetron. A three-stub tuner (a) was used to match the impedance of the heating system and the plasma. The tuner is followed by a rectangular-to-circular transition (b). According to the cold plasma wave theory discussed in Ch. 2, only a right-hand circularly polarised wave (R-wave) is efficiently absorbed at the cyclotron resonance. Therefore, a polariser (c) was developed to convert the linear polarised wave produced by the magnetron into the R-wave. The polariser [35] was a piece of a circular waveguide with two parallel metal bars attached to the inner side. The dimensions of the metal bars had been optimised with CST microwave simulations to obtain circular output polarisation. The polarisation of the output wave could be controlled by rotating the polariser around its axis.
Due to possible hazardous X-ray emission from the plasma, the vessel was covered with lead plates, as shown in Fig. 3.2 (Right). The figure also shows the port that was used for

the auxiliary plasma heating at 2.45 GHz with the $\leqslant$ 2kW power. For more information on the auxiliary heating see Ch. 7.

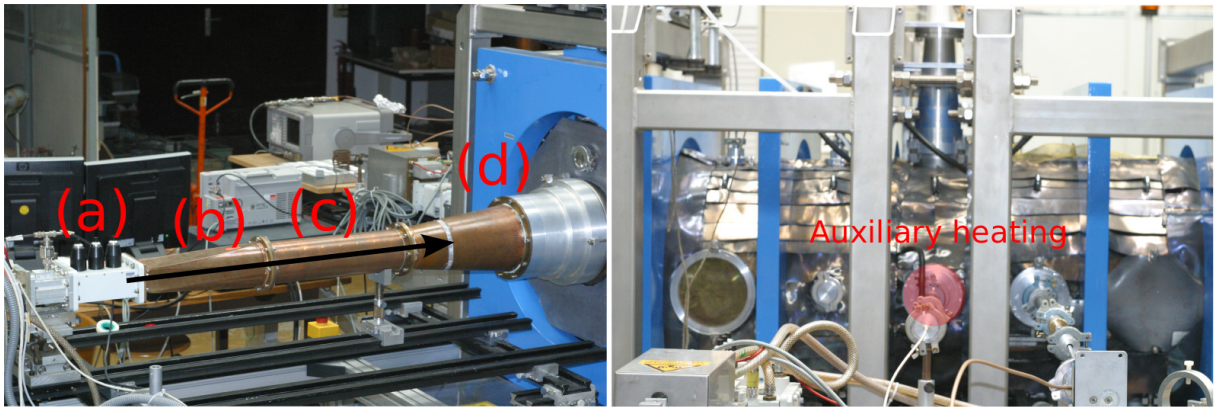

Figure 3.2: Left: the main plasma heating system. (a)-three stub tuner, (b)-rectangular-to-circular transition, (c)-polariser, (d)-taper. Right: the port in the middle was reserved for the O- or X-wave injection across the background magnetic field. The lead plates were installed to reduce the X-ray emission

3.3 Diagnostics

In the course of the work, FLiPS was equipped with an interferometer and a Langmuir probe. An interferometer is a non-invasive diagnostic that measures the average plasma density along the line-of-sight

$$\bar{n}_e = \frac{1}{l}\int_0^l n_e(r)dr, \tag{3.1}$$

where $\bar{n}_e$ is the average density and l is the length of the line-of-sight, which in the case of FLiPS equals to D_{FLiPS}. The principle of the diagnostic is based on comparing the phase difference between two microwave beams, one of which propagates through the plasma (plasma channel) and the other is the reference as described in [36, 37]. A well-collimated Gaussian beam was launched into the plasma by a lens horn and received by a smaller corrugated horn antenna. This helped to reduce the standing wave between the horns, which could affect the interferometric measurements.
A schematic of the interferometer at FLiPS is shown in Fig. 3.3. A directional coupler (b) splits the incoming 70 GHz microwave generated by a Gunn oscillator. One part of the signal goes through the plasma and the other through the reference channel. Afterwards, both are combined by the directional coupler (d). The whole system was fixed to a rigid metal frame around the vessel to avoid effects caused by vibrations. The length of the plasma and reference channels were balanced to avoid measurement errors due to possible frequency variations of the Gunn oscillator.
The total time-averaged intensity was measured by the diode detector (e) and depends on the phase shift between the signals in the plasma and reference channels, as shown in Fig. 3.3. The phase difference and the line-averaged plasma density are related as follows [36]

$$\frac{\Delta\phi}{2\pi} \approx \frac{D_{FLiPS}}{2\lambda n_c}\bar{n}_e, \tag{3.2}$$

where λ is the wavelength of the probing signal and n_c is the corresponding plasma cutoff density. The simple and robust setup of the interferometer could unambiguously measure

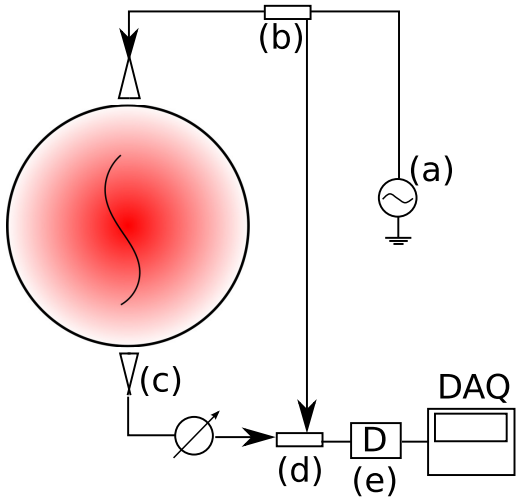

Figure 3.3: A schematic of the homodyne interferometer diagnostic at FLiPS. (a)-70 GHz microwave source, (b), (d)-directional couplers,(c)-phase shifter, (e)-diode detector.

$\Delta\phi < \pi$, which was sufficient for the FLiPS experimental conditions. A typical example of an interferometric signal measured in FLiPS is shown in Fig. 3.4. After the initial density rise, the plasma density stays relatively constant for $t > 1$ s until the end of the discharge at $t = 5$ s. The signal shows density fluctuations with the standard deviation $\sigma = 0.11$. Since the measurements were line-averaged, the local density fluctuation level could be much higher.

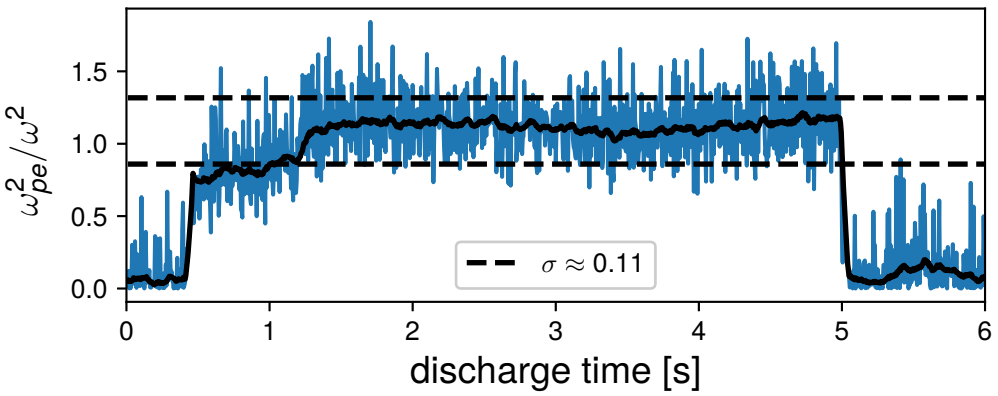

Figure 3.4: A typical interferometric signal measured at FLiPS plotted as ω_{pe} normalised to the frequency of the main heating system ω. The discharge duration was 5 s. The magnetron was turned on at $t = 0$. The MW power was set to 4.8 kW. After the discharge there was a low density plasma in the vessel, since the magnetron still radiates power even when the modulation is not active, which is enough to maintain this afterglow plasma.

The local plasma parameters were measured using the Langmuir probe (LP) diagnostic [37]. A LP is a small metal tungsten wire inserted into a plasma. Biasing the tip and measuring the current draw, one obtains the current-voltage (IV) characteristic, from which the local plasma parameters such as n_e and T_e can be deduced. An idealised IV-characteristic of a probe in an unmagnetized, collisionless plasma is shown in Fig. 3.5. The potential V_{fl} is called the floating potential at which $I(V_{fl}) = 0$. At the floating potential V_{fl} there is no current draw, since the ion and electron currents balance out each other. The IV-characteristic can be divided into three regions. In the regions (A) and (C) the probe current is the ion saturation $I_{i,sat}$ and the electron saturation $I_{e,sat}$ current, respectively. The characteristic shown in Fig. 3.5 is said to be idealized [1] because in reality the $I_{e,sat}$ does not reach the plateau and keeps increasing with the applied voltage.

An example of the experimentally measured IV-characteristic is shown in Fig. 3.6.

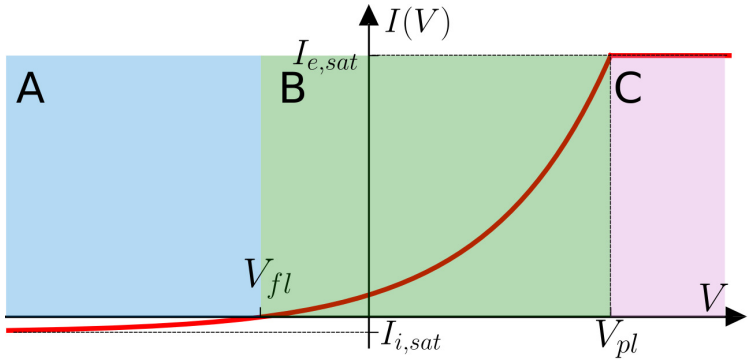

Figure 3.5: The idealized IV-characteristic of a Langmuir probe. Three distinctive regions A, B, C can be identified. A, C are the ion/electron saturation regimes and B is the exponential part.

The ion saturation current is given by

$$I_{i,sat} = 0.61 e n_e A_s \sqrt{\frac{T_e}{m_i}}, \tag{3.3}$$

where A_s is the probe surface and m_i is the ion mass. From the ion saturation measurements only, it is impossible to calculate separately T_e or n_e. However, coupled with the interferometric measurements, it can serve as an indication for the appearance of hot electrons. The X-ray emission was sometimes detected for neutral gas pressures $< 10^{-2}$ Pa. At these pressures, the electrons do not collide often enough with the other particles to become thermalised. It explains why the X-ray emission was detected at low plasma densities. As the electrons pass through the electron cyclotron region, they gain energy from the R-wave. Eventually, the confinement of these electrons is lost and they collide with the vessel walls, which causes the X-ray emission, due to the bremsstrahlung [7, 37].

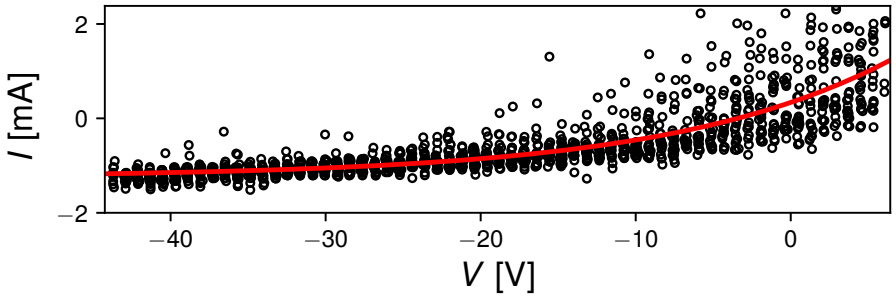

Figure 3.6: An example of the IV-characteristic measured in FLiPS. The obtained plasma parameters are $T_e = 14$ eV and $n_e = 6 \times 10^{17}$ m^{-3}. It is sufficient to measure the IV-characteristic only around the floating potential

The main drawback of the LP measurements is the complicated theory in the case of magnetised plasmas, since the effective collective area of the probe is modified by the magnetic field, leading to a large error in n_e. To obtain the correct local plasma density, the data from the interferometric measurements was used as follows

$$\frac{C}{D_{FLiPS}} \int_{-R_{FLiPS}}^{R_{FLiPS}} n_e'(r) dr = \bar{n}_e, \tag{3.4}$$

where $n_e'(r)$ are the LP measurements, $\bar{n}_e$ is the average radial density from the interferometric measurements and C is a normalisation constant. Thus, when the density profile is

measured with a LP, the constant C can be found and the correct local density obtained as $n(r) = Cn'_e(r)$.

3.4 Heating by EBWs

Using the measured density profile, the expected efficiency of the two coupling schemes to the EBWs for the FLiPS plasma will be calculated. Then, the possible damping mechanisms that can affect coupling to the EBWs will be discussed.

3.4.1 Coupling scheme

The most important parameter that determines which conversion scheme is preferable, is the density gradient length L given by Eq. (2.28). The value of L can be calculated at any point at the profile and characterises how fast the density changes. For the O-X conversion and the direct FX-SX scheme, the required density-gradients are L_O at the O-cutoff and L_{UHR} at the UHR, respectively. From Fig. 3.7, the density gradient length for both cases can be calculated to determine which of the two coupling scheme is preferable for the FLiPS plasma. In the case of the O-X conversion L_O is given by

$$L_O = \left(\frac{dX}{dr}\Big|_O \right)^{-1} X_O, \tag{3.5}$$

where the derivative is calculated at the O-cutoff and $X_O = 1$. Thus, L_O is determined

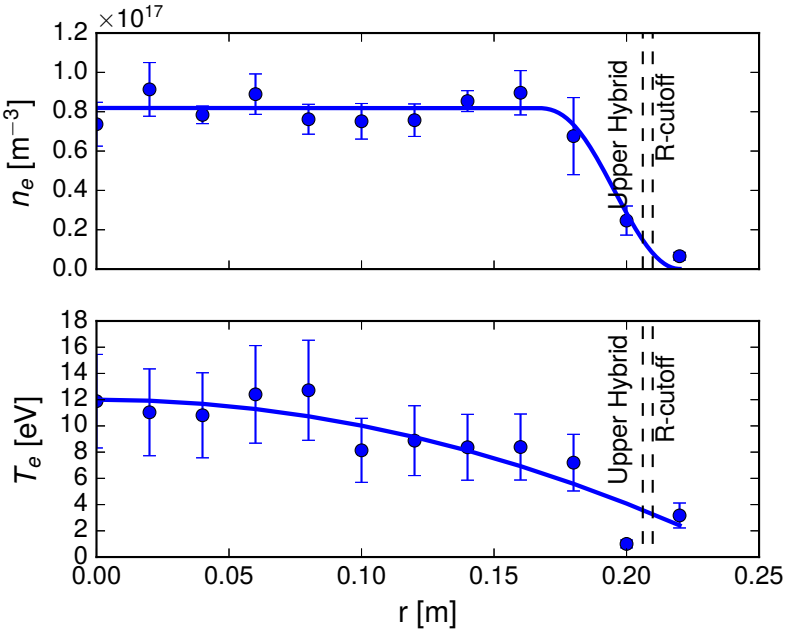

Figure 3.7: Langmuir Probe measurements of the FLiPS plasma parameters. The absolute value of n_e was obtained using the interferometric data. The measurements show that the plasma density has a steep rise at the edge and remains approximately constant in the plasma bulk. The density profile was fitted using Eq. (4.3).

only by the plasma density profile. For the measured profile the density gradient normalised to the wave vector is $k_0 L_O < 3$. For such L_O, Mjølhus' formula given by Eq. (2.27)

might be not applicable due to the smallness of the density-gradient length, since the formula assumes total absorption of the SX-wave at the UHR. For small density-gradient lengths, the SX-mode leaks through the UHR and leaves the plasma as a FX-mode. The estimation of the conversion efficiency in this case requires numerical simulations. The corresponding numerical simulations will be presented in detail in Ch. 5. The simulations show that even for the optimal injection angle $C_{eff} < 0.4$.
In the case of FX-SX coupling, L_{UHR} is

$$L_{UHR} = \left(\frac{dX}{dr}\Big|_{UHR} \right)^{-1} X_{UHR}, \tag{3.6}$$

where $X_{UHR} = 1 - Y$ is the density of the plasma at the UHR. Thus, L_{UHR} depends on the background magnetic field. Figure 3.8 gives C_{FX-SX} as a function of the background magnetic field, assuming the density profile in Fig. 3.7. From Fig. 3.8 it can be conclude that the maximum of C_{FX-SX} is achieved around $Y = 0.6$. However, this plot has to be treated with caution, because even small density fluctuations can lead to a significant modification of C_{FX-SX} .

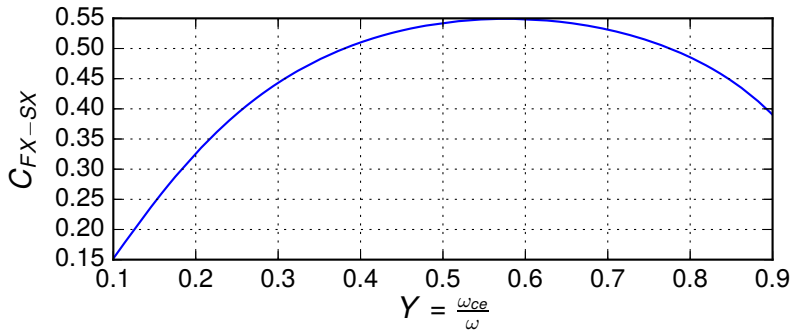

Figure 3.8: The efficiency of the FS-FX tunnelling for the density profile shown in Fig. 3.7 as a function of the background magnetic field calculated using Eq. (2.31). The C_{FX-SX} was calculated assuming presence of the L-cutoff given by $X = 1 + Y$.

Another important aspect that must be discussed is the presence of the L-cutoff in the plasma. The FX-SX coupling scheme can be very efficient, when the L-cutoff lies inside the plasma, as discussed in Sec. 2.3.2. From Fig. 3.7, the peak density $n_e = 0.8 \times 10^{17}$ m^{-3}, which corresponds to $X = \frac{\omega_{pe}^2}{\omega^2} = 1.1$. The L-cutoff is inside the plasma when the $X \geqslant 1 + Y$. In the experiments that were performed in course of the study, $Y \geqslant 0.7$, therefore the density must fulfil $X \geqslant 1.8$. Thus, for the measured profile shown in Fig. 3.7, the L-cutoff is not inside the plasma.

3.4.2 Collisional damping and parametric decay

The collisional damping of the SX-mode at the UHR can reduce coupling to the EBW [6]. The effect of collisions on the EBWs has been discussed in [38, 39], where the authors estimated that the EBW propagation is not strongly affected by the collisions when $\nu_{coll}/\omega < 10^{-4}$, where ν_{coll} is the collisional frequency. In FLiPS, the electrons collide mainly with ions and with neutrals. Thus, $\nu_{coll} = \nu_{ei} + \nu_{en}$, where ν_{ei} and ν_{en} are electron-

ion and electron-neutral collisional frequencies given by [7]

$$\nu_{en} = \sigma v_{th} n_0 \tag{3.7}$$

$$\nu_{ei} = 2 \times 10^{-6} n_e \frac{\ln[\Lambda_D/b]}{T_e^{1.5}}, \tag{3.8}$$

where σ is the total cross-section, which characterises the likelihood of the electron-neutral interaction, and n_0 is the neutral gas density. For Ar, the total cross-section can be estimated as $\sigma \leq 25 \times 10^{-20}$ m^2, based on [7]. The term $\ln[\Lambda_D/b]$ is the so-called Coulomb logarithm [1] defined as a logarithm of the ratio of the Debye radius Λ_D to the impact parameter b. The value of ν_{ei} mainly depends on T_e. The lower T_e corresponds to the higher collisional frequency. This dependency is explained by the fact that the interaction time of the faster electrons with the ions is shorter than for the slow electrons. In very cold plasmas which occurs at the plasma edge, ν_{ei} can become large enough to effectively damp the EBWs [40].
Figure 3.9 shows ν_{coll}/ω, calculated according to Eqs. (3.7, 3.8). The range of parameters found in the FLiPS plasma is labelled with a white cross. Thus, even though T_e is small at the plasma edge, thanks to low n_e the collisional frequency is small enough to allow EBW propagation. However, it should be noted that in [40], wave propagation in a

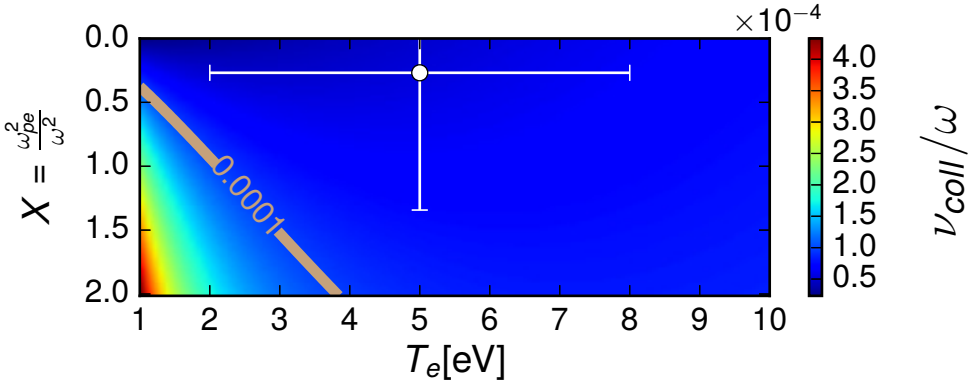

Figure 3.9: Normalised collisional frequency ν_{coll}/ω as a function of T_e and X. Lower density and higher T_e correspond to the low collisional frequency. The white cross shows the range of expected plasma parameters at the plasma edge in FLiPS.

magnetised plasma with parameters similar to FLiPS plasma was investigated, and the authors came to the conclusion that the SX-mode in their experiment was completely collisionally damped before turning into the EBW at the UHR.
An additional loss channel that can reduce coupling to EBWs is the parametric decay [6, 41]. The parametric decay is a non-linear process, where an incoming pump wave decays into daughter waves. The parametric decay occurs, when the amplitude of the electric field exceeds a parametric decay threshold [6], which can occur at the UHR. The parametric decay was, for example, detected in MAST for intense injected microwave powers > 1 MW as reported in [42].
The parametric instability threshold power is given by [43]

$$\frac{P^*_{UHR}}{\pi\rho^2} = 2 \times 10^{-3} \left(\frac{\mathrm{W}}{\mathrm{cm}^{2/3}\mathrm{T}^{1/3}\mathrm{GHz}^{1/3}\mathrm{eV}^{13/6}} \right) \times \frac{f^{1/3} T_e^{13/6} B^{1/3}}{L^{4/3}}, \tag{3.9}$$

where all plasma parameters are taken at the UHR, and ρ is the beam radius. Taking $T_e \approx 10$ eV, $k_0 L \approx 0.5$ and $\rho \approx 5$ cm, the threshold power $P^*_{UHR} = 6$ kW, which

significantly exceeds the power of the auxiliary heating. Therefore, it is unlikely that the parametric decay can be a significant loss channel. However, it should be noted that in [44] the parametric decay was observed experimentally in a plasma similar to the FLiPS plasma, and the authors concluded that the parametric decay at the UHR did not significantly affect the plasma heating.

3.4.3 Plasma fluctuations

In previous experimental studies of EBW [23, 45], the plasma waves were studied in the so-called glow discharges to avoid plasma fluctuations. The plasma of a glowing discharge is more quiescent than a plasma produced by microwave heating such as the R-wave heating used at FLiPS. The plasma fluctuations include not only density fluctuations, but also temperature fluctuations (δT_e) and plasma potential fluctuations (δV_{pl}). Measuring local plasma fluctuations can be performed with a single or with the so-called emissive Langmuir probes [46]. The measurement of plasma fluctuations is an active research topic in plasma physics. In this study, only the density fluctuations δn_e were measured. The measurements of the plasma fluctuations in FLiPS is important, since in the FLiPS plasma $\omega_{pe} > \omega_{ce}$. According to [7], plasmas with $\omega_{pe} > \omega_{ce}$ become unstable. Thus, it is expected that the FLiPS plasma has density fluctuations that can strongly affect the coupling to EBWs and their propagation.
According to the interferometric measurement shown in Fig. 3.4, the density fluctuations $\delta\bar{n}_e/\bar{n}_e \approx 0.11$, where $\bar{n}_e$ is the line-averaged density defined by Eq. (3.1).
The local density fluctuations were measured at two positions with a single Langmuir probe using the ion saturation part of the IV-characteristic. According to [47, 48], δT_e do not strongly affect the Langmuir probe measurements, which allows a straightforward calculation of δn_e from the following relation

$$\frac{\delta I_{i,sat}}{I_{i,sat}} = \frac{\delta n_e}{n_e}. \tag{3.10}$$

At the central position the local density fluctuations are $\delta n_e/n_e \approx 0.11$, which matches the value obtained with the interferometric measurements. At the edge position the local density fluctuations $\delta n_e/n_e \approx 0.13$, which shows that both central and edge plasma are affected by the fluctuations. The measured value of the density fluctuations will be used in Ch. 4 to investigate their effect on the coupling efficiency to the EBWs.

3.4.4 Landau damping

When EBWs propagate at an angle to the background magnetic field, even without the collisions, the so-called Landau damping will occur [20, 3]. The Landau damping is significant when the phase velocity of the wave is comparable to the thermal velocity of the electrons. In this case, the wave strongly interacts with the particles and the wave energy is transferred from the wave to the electrons. Thus, a wave is not Landau damped, when the following criterion is satisfied [49]

$$\frac{\omega}{k_\parallel} \gg \sqrt{\frac{2eT_{e,\parallel}}{m_e}} \tag{3.11}$$

According to this criterion, for $T_{e,\parallel} = 10$ eV, the waves are not affected by the Landau damping, when the parallel refractive index $N_\parallel < 156$. At FLiPS, the expected values are

$N_{\parallel} < 10$, as seen in Fig. 6.11. Thus, it can be concluded that the EBWs in the FLiPS plasma are not unaffected by the Landau damping.

3.5 Summary

In this chapter, the linear plasma device FLiPS was described. The heating system, based on the R-wave absorption at the cyclotron resonance, provided a reliable plasma heating. Results of the interferometric and the Langmuir probe measurements showed that the plasma is moderately overdense and the density-gradient length is small compared to the vacuum wavelength 0.12 m of 2.45 GHz. Thus, for the O-mode launch, a reasonable, but by far not perfect coupling to EBWs over a broad range of angles (see Fig. 2.10) is expected. In the case of the X-mode auxiliary heating, a better coupling is expected because the small distance between the R-cutoff and the UHR favours the coupling to the EBWs.
The FLiPS plasma density was found to be small enough so that the collisional damping should not be significant [38]. On the other hand, the low T_e is beneficial, since the Landau damping is not expected to play a significant role in the experiment. Therefore, FLiPS provides a good test bed for the EBW investigation in the fusion relevant plasmas. However, processes such as fluctuations and collisions still can prevent efficient coupling to the EBWs. Indeed, the UHR, where coupling to EBWs occurs, is located close to the plasma edge, where the plasma was found to be fluctuating, and precise measurement of T_e is difficult.

Chapter 4

The Finite-Difference Time-Domain Method

4.1 Introduction

The previous chapter dealt with the measurements of the base plasma parameters. The base plasma provided a controlled environment to study the efficiency of the additional heating, which will be referred to as the auxiliary heating. The measurements showed that the typical plasma gradient lengths of the FLiPS plasma are smaller than the expected wavelengths of the O- and X-modes in FLiPS. Therefore, the geometrical optics approximation cannot be applied to describe their propagation in the FLiPS plasma, and the full set of the differential equations describing the wave propagation must be solved [50].
In this chapter, the auxiliary heating will be investigated using the so-called Finite-Difference Time-Domain (FDTD) method, which is comprehensively described in [8]. The FDTD method had already been successfully applied to investigate the coupling of the FX-mode to the SX-mode in magnetised plasmas bounded by vessel wall [40, 51]. One of the advantages of the FDTD method is that it is possible to include- arbitrarily shaped structures such as the vessel wall in the simulations. The main objective of the simulations in this chapter is to estimate the efficiency of the FX-mode coupling to the EBWs, when factors such as reflections from the vessel wall, finite beam width, and the shape of the UHR and R-cutoff layers are all taken into account.
Apart from a few exceptions, the power of the auxiliary heating in the experiments was small compared to the main heating system. Therefore, it can be assumed that the base plasma is unaffected by the auxiliary heating. In further discussions, the wave propagation will be described by the cold plasma dispersion relation given by the Altar-Appleton-Hartee dispersion relation (2.17). It means that in this chapter, the EBWs will not be considered explicitly, since the plasma is assumed to be cold. In the following FDTD simulations, SX-mode will be completely damped collisionally at the UHR. However, as pointed in [30], the collisional absorption of the SX-mode at the UHR is equivalent to the coupling efficiency of the SX-mode to the EBWs. Thus, despite using the cold plasma model, the correct coupling efficiency still can be obtained. The full-wave simulations of EBWs will be carried out in Ch. 5.
Only 2D FDTD simulations will performed. It means that the plasma properties may vary arbitrarily in the 2D plane, where the waves propagate. But along the third dimension, which is perpendicular to this plane, the plasma remains homogeneous. Treating the wave phenomena in 2D allows investigation of the effect of the vessel wall and the

axial plasma inhomogeneity, which are missing in the 1D simulations. In contrast, the 3D simulations would be very computationally demanding, and the benchmarking of the obtained results will be complicated. Thus, the expected problems outweigh the benefits of the plasma investigation in the 3D geometry.

4.2 Introduction to FDTD

The FDTD method solves Maxwell's equations on a discrete numerical grid with the time and space derivatives replaced with the corresponding central differences. The method is in the time domain, which means that one can visualise field propagation in time and obtain transient solutions as well as steady-state solutions, when the simulation time is long enough.
In FDTD simulations even a monochromatic source will initially produce a band of frequencies as it starts to run. As time progresses, these frequencies will decay, and only the central frequency will remain. In this state, called a steady state, the fields and the currents will oscillate at the frequency of the source.
The FDTD method is based on the so-called Yee grid, first introduced in [52], which is a particular way to arrange electromagnetic fields on the discrete numerical grid in time and space. To understand how the method works consider a simple 1D case with a plane wave

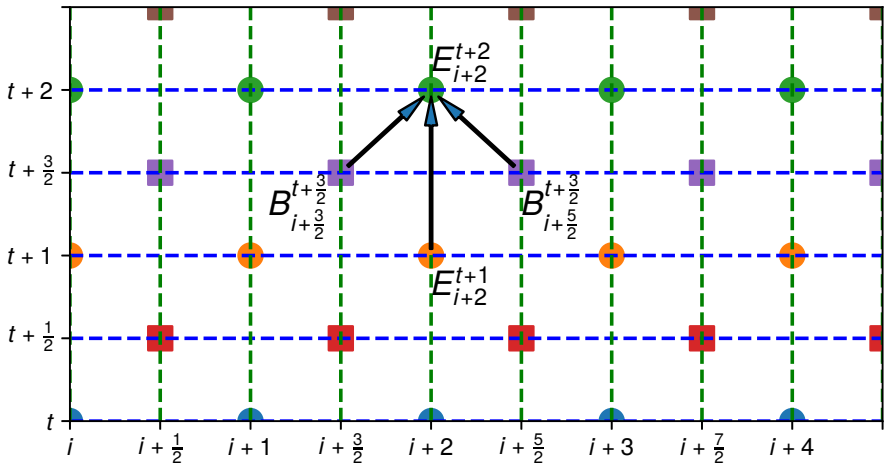

Figure 4.1: Illustration of 1D Yee grid. The magnetic and electric fields are shifted with respect to each by $\frac{1}{2}$ in time and space. The fields propagate in time according to Eq. (4.3) which requires fields in the adjacent nodes.

propagating along the z-direction in a medium. The corresponding 1D Yee grid shown in Fig. 4.1 demonstrates how the fields progress in time and space. Then the corresponding Maxwell's equations are

$$\begin{cases} \dfrac{\partial B}{\partial z} = \dfrac{1}{c^2}\dfrac{\partial E}{\partial t} + \mu_0 j \\ \dfrac{\partial E}{\partial z} = -\dfrac{\partial B}{\partial t} \end{cases} \tag{4.1}$$

The medium properties enter into the equations through the induced current density j. Replacing the derivatives with the central differences, the equations transform into the

following form

$$\begin{cases} \dfrac{B_{i+\frac{3}{2}}^{t+\frac{1}{2}} - B_{i+\frac{1}{2}}^{t+\frac{1}{2}}}{\Delta z} = \dfrac{1}{c^2}\dfrac{E_{i+1}^{t+1} - E_{i+1}^{t}}{\Delta t} + \mu_0 \dot{j}_{i+1}^{t+\frac{1}{2}} \\ \dfrac{E_{i+1}^{t} - E_{i}^{t}}{\Delta z} = -\dfrac{B_{i+\frac{1}{2}}^{t+\frac{1}{2}} - B_{i+\frac{1}{2}}^{t-\frac{1}{2}}}{\Delta t}, \end{cases} \tag{4.2}$$

where the lower and upper indices correspond to the spatial coordinate and to the time, respectively. The time and spatial steps lengths are Δt, Δz, respectively. After a straight forward algebra the update equations for the fields are

$$\begin{cases} B_{i+\frac{1}{2}}^{t+\frac{1}{2}} = B_{i+\frac{1}{2}}^{t-\frac{1}{2}} - \dfrac{\Delta t}{\Delta z}(E_{i+1}^{t} - E_{i}^{t}) \\ E_{i+1}^{t+1} = E_{i+1}^{t} + \dfrac{\Delta t}{\Delta z} c^2 (B_{i+\frac{3}{2}}^{t+\frac{1}{2}} - B_{i+\frac{1}{2}}^{t+\frac{1}{2}}) - \dfrac{\Delta t}{\epsilon_0} \dot{j}_{i+1}^{t+\frac{1}{2}} \end{cases} \tag{4.3}$$

In a cold magnetised plasma the term $\vec{j}$ is given by

$$\frac{d\vec{j}}{dt} = \epsilon_0 \omega_{pe}^2 \vec{E} + \vec{j} \times \hat{\omega}_{ce} - \nu \vec{j}, \tag{4.4}$$

where $\hat{\omega}_{ce} = e\vec{B}_0/m_e$. The term ν is the collisional frequency that describes a damping mechanism. Replacing the time derivative with the central difference leads to the following relation

$$\frac{\vec{j}^{t+\frac{1}{2}} - \vec{j}^{t-\frac{1}{2}}}{\Delta t} = \epsilon_0 \omega_{pe}^2 \vec{E}^t + \vec{j}^t \times \hat{\omega}_{ce} - \nu \vec{j}^t, \tag{4.5}$$

where $\vec{j}$ and $\vec{E}$ are assumed to be placed at the same nodes of the Yee grid. Thus, in a magnetised plasma to advance the current in time, one needs the value $\vec{j}^t$, which has not been found yet. To overcome this problem, its value can be interpolated as follows [53]

$$\vec{j}^t = \frac{\vec{j}^{t+\frac{1}{2}} + \vec{j}^{t-\frac{1}{2}}}{2} \tag{4.6}$$

Other methods to interpolate $\vec{j}^t$ also exist. The choice of the method may affect numerical stability as reported in [53].

The temporal and spatial steps cannot be chosen independently. Stability analysis of the method in the case of propagation in vacuum gives the following general bound for Δt for which the method is stable

$$c\Delta t \leq \left(\frac{1}{\Delta x^2} + \frac{1}{\Delta y^2} + \frac{1}{\Delta z^2} \right)^{-\frac{1}{2}}, \tag{4.7}$$

where c is the speed of light. In the plasma case, the condition above is not sufficient, and the upper bound of Δt must be determined empirically [54, 55].

The number of the nodes on the grids is finite, thus the grid must be terminated with proper boundary conditions. Setting the fields to zero at the boundary nodes will cause reflections since in this case the boundary behaves like a perfect conductor. The reflections can be reduced by introducing a medium before the boundary with a slowly increasing damping rate towards the boundaries. The layer has to be thick enough to sufficiently damp the wave before the reflection occurs. The thickness of the absorbing layer is usually

one or two vacuum wavelength [56]. The main disadvantage of this approach is enlargement of the numerical grid due to the additional layer.
The most advanced approach is to truncate the grid with the so-called perfectly matched layer (PML) [8]. The PML needs much less grid point than the absorbing medium around the boundaries. The simulations performed in the thesis had the PML layer thickness set to $20\Delta x$, which was sufficient to avoid reflections from the boundaries. Therefore, the use of the PML made the computational domain smaller, which resulted in the reduction of computational time.

4.3 2D plasma wave simulations with IPF-FD3D

The simulations were carried out with the IPF-FD3D code, developed by C. Lechte for the Doppler reflectometry simulations [57]. The code is based on the cold plasma model, written in C and fully parallelised. The numerical stability was assured by relating the time and spatial steps as $\Delta x = 2c\Delta t$, which is consistent with the criteria given by Eq. (4.7). The time steps that were normally used in the simulations, were $\Delta T = T/256$ and $\Delta T = T/512$, where T is the wave period. It means that there were 128 or 256 Yee cells per vacuum wavelength. The numerical grid was terminated with the PML. The wave was excited by an antenna placed right after the PML. It was possible to excite either the magnetic or electric field components of the wave. The field amplitudes at the antenna plane were ramped up slowly to minimize creation of spurious frequencies. The code provides a number of different methods to calculate the $\vec{j}^t$ term. In this chapter, the interpolation scheme given by Eq. (4.6) was always used. A detailed description of the code and its different current solvers can be found in [53].
Reflecting structures can be implemented in the FDTD method by setting the tangential electric field to zero at the surface. A more consistent way, which was used in this investigation is to use a highly overdense unmagnetised plasma as the vessel wall. The density of the plasma that was used to model the vessel wall was taken as the maximal plasma density that can be resolved in the FDTD simulations. The maximal frequency that can be resolved in the FDTD simulations is given by $\omega_{max} = 1/\Delta t$. Thus, the maximal plasma frequency that can be used in the simulations is $\omega_{pe} = \omega_{max}$. From that the maximal plasma density that can be used in the simulations found as $n_e = \epsilon_0 m_e/e^2\Delta t^2$. Within this well established approach, effects of the ohmic losses in the walls due to the finite conductivity can be included [58, 59].
The wave propagation was simulated in the plasma with the density profile given by

$$X = X_0 + (X_1 - X_0)\left(1 - \left(\frac{x}{x_b}\right)^{p_1}\right)^{p_2} \tag{4.8}$$

where $p_1 = 2$, $p_2 = 3$. The parameter x_b characterises the width of the plasma edge and determines the density gradient. This function describes closely the experimentally measured density profile shown in Fig. 3.7 with $x_b = 0.02$ m.
The magnetic field in all simulations corresponds to 500 A in the outer coils and 320 A in the inner coils. This magnetic field configuration was normally used in the experiments as it could support a stable plasma without X-ray emission.
Since the simulations were in the 2D geometry, the simulations were performed in the two main characteristic planes, which are the central poloidal plane ($x - y$, $z = 0$) and the

central axial plane ($x - z$, $y = 0$), as depicted in Fig. 4.2. For each plane, the O- and X-mode heating scenarios were investigated .

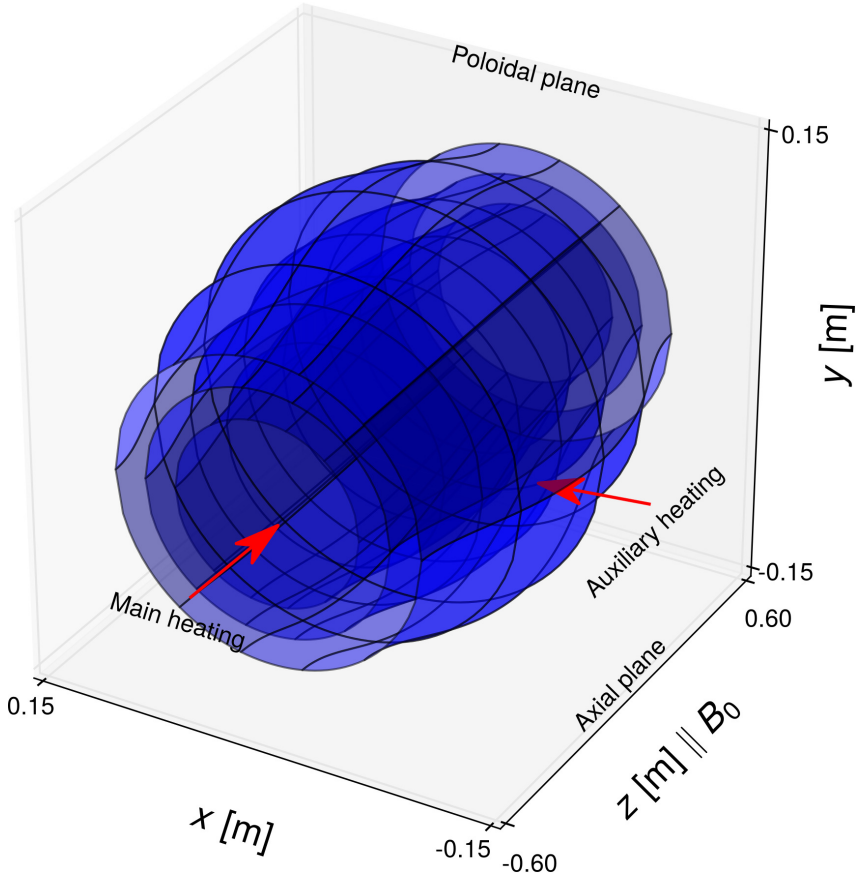

Figure 4.2: 3D geometry of the FLiPS magnetic field. The radii of the surface at the openings are 0.1 m, 0.8 m and 0.6 m. The lines on the surface along the z-axis are the magnetic field lines. The openings become more narrow towards the ends since the magnetic field is stronger there. Two characteristic planes were defined where 2D FDTD simulations were performed: axial plane at $y = 0$ and the poloidal plane at $z = 0$.

4.4 X-mode absorption

The analysis of the results of the FDTD simulations requires the usage of the Budden problem, described in Sec. 2.3.2. By comparing the theoretical predictions with the simulations it is possible to establish the optimal duration of the simulations and the optimal resolution of the numerical grid. Duration of the FDTD simulations must be long enough that the steady state is achieved. Otherwise, the numerically obtained conversion efficiency does not match the analytical theories which were derived under the assumption that the system is in the steady state. On the other hand, simulations cannot be too long since the round-off errors become significant and may cause numerical instability.
The Budden formula determines the absorption of the FX-mode due to the UHR, and is given by [20, 60]

$$A_B = e^{-\pi s}(1 - e^{-\pi s}), \tag{4.9}$$

where $s = k_0 \Delta x$, $\Delta x = x_{UHR} - x_R$ is the distance between the UHR and R-cutoff. The Budden formula is derived for a medium with the refractive index shown in Fig. 2.11. The incoming FX-mode encounters the resonance only once, and afterwards is assumed to

propagate indefinitely. However, in the FLiPS plasma due to the radial density gradient, the SX-mode will pass through the resonance twice as demonstrated in Fig. 4.3. The

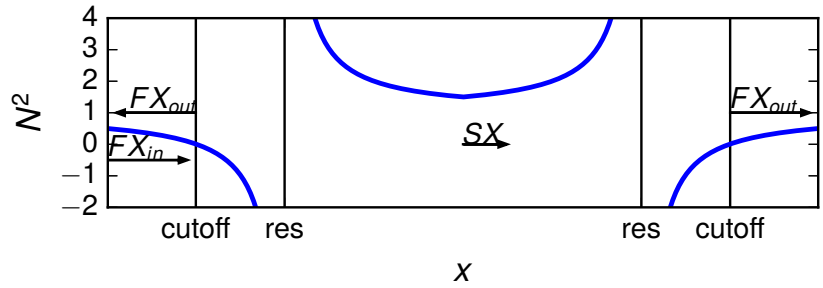

Figure 4.3: The refractive index of the X-mode has two resonances ($N^2 \to \infty$) and two cutoffs ($N^2 < 0$) due to the radial density gradient unlike in the original Budden problem as shown in Fig. 2.11.

range of applicability of the Budden formula can be extended to account for the second absorption as follows

$$A_{tot} = A_B + e^{-\pi s}(1 - e^{\pi s}) \tag{4.10}$$

The total absorption A_{tot} can be calculated, using the Poynting flux through the surface, enclosing the whole plasma, as shown in Fig. 4.4 (a). Since the incoming energy flux is known, the absorption of the wave energy can be found.

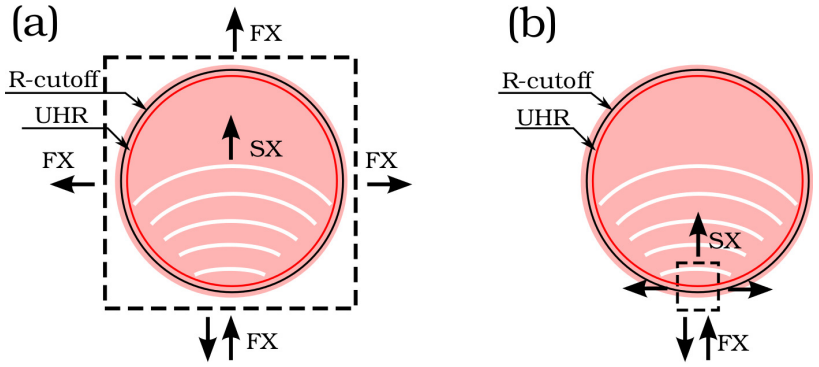

Figure 4.4: A schematic of the FLiPS poloidal cross section to explain the calculation the absorption. The dashed enclosure is the boundary through which the Poynting flux of the FX-mode was calculated. (a): the whole plasma is within the enclosure and the total absorption of the incoming FX-mode can be found. (b): the enclosure is chosen around the UHR which allows to find the absorption coefficient locally and compare it with the Budden theory.

4.5 Density fluctuations

As discussed in Sec. 3.4.3, the FLiPS plasma has density fluctuations that affect the coupling to EBWs. The fluctuations and instabilities make the plasma turbulent. Numerical simulations for the wave propagation in turbulent plasmas require a vast amount of computational power as one has to use many turbulence realisations as described in [61], and for each of the realisations a FDTD simulation must be carried out.

To avoid performing demanding simulations and still be able to include effects of the plasma fluctuations on the wave propagation a simplified model will be used. In this model only the cumulative effect of the local density fluctuations on the peak density is considered. This cumulative effect can be estimated from the interferometric measurements.

The interferometric measurements shown in Fig. 3.4 are line-averaged measurements

meaning that the fluctuations are averaged along the line-of-sight of the interferometer. From the standard deviation of the interferometric signal, the cumulative effect of the fluctuations changes the density by about ±10% with respect to the mean density. Thus, the effect of the density fluctuations on the wave propagation can be approximately included in the density profile by modifying the peak density of the density profile as shown in Fig. 4.5. This changes the distance Δx between the R-cutoff and the UHR which affects the coupling to SX-mode.
Since in the FDTD simulations, the cold plasma model is used, the temperature fluctuations are not included. But as T_e is low, the O- and X-modes are almost unaffected by T_e, and the effects due to temperature fluctuations on these modes can be neglected.

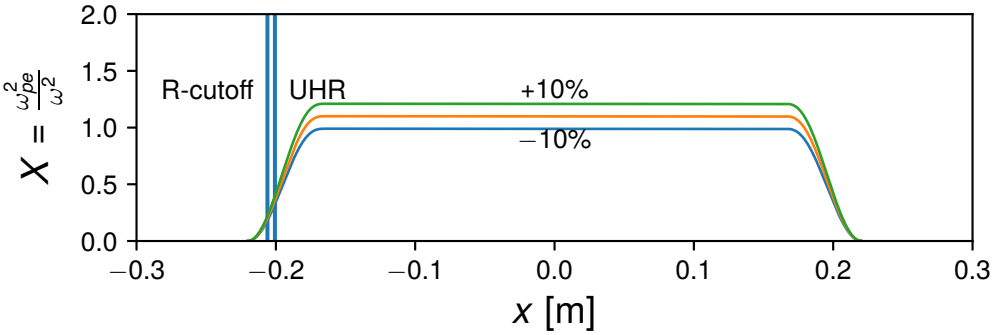

Figure 4.5: Fitting of the experimentally measured density profile with the function (4.3) and its variations due to the density fluctuations. The profiles are characterised by a steep edge and a flat central part with a constant density. The density fluctuations change the level of the central density altering the edge density gradient. In the figure, density profiles with $\delta X/X = \pm 10\%$ of the experimentally measured density profile are presented.

4.6 Results and discussions

4.6.1 Simulations in the poloidal plane

Here, the FDTD simulations will be presented in the poloidal plane. This plane is defined as the $z = 0$ plane, and is shown in Fig. 4.2. In this plane, the propagation of the O- and X-modes was simulated. The O-mode was excited by the E_z component, which is parallel to the background magnetic field and perpendicular to the simulation plane. The X-mode was excited by the B_z component with the corresponding electric field (E_x, E_y) lying in the $z = 0$ plane.
In these simulations, the O- and X-mode propagate perpendicular to the background magnetic field. In this geometry, the coupling between the modes is completely absent [20], thus the evaluation of the O-X conversion efficiency is impossible, and only the FX-SX coupling efficiency can be found.
Figure 4.6 (left) shows the time-averaged field of the O-mode. The field is not affected by the magnetic field and thus by the UHR, and therefore the field pattern is symmetric with respect to $x = 0.25$ m plane. As expected, the O-mode field decreases beyond the O-cutoff, where the wave is evanescent. For a plane, which is shifted from the central plane ($z = 0$), the antenna would radiate a mixture of the modes. As shown in Sec. 2.3.1, an obliquely propagating O-mode can couple to the X-mode at O-cutoff. Therefore, in the shifted plane the symmetric pattern of the O-mode would be disturbed and the field would be increased around the UHR. The field distribution of the X-mode is asymmetric, due to the density gradient. This effect had been predicted theoretically in [60] and

further discussed in [62]. It can be seen that the field is amplified at the UHR, where the SX-mode becomes predominantly electrostatic. Since the UHR is located close to the edge, where the electron temperature is low, one may expect strong collisional damping of the EBWs.

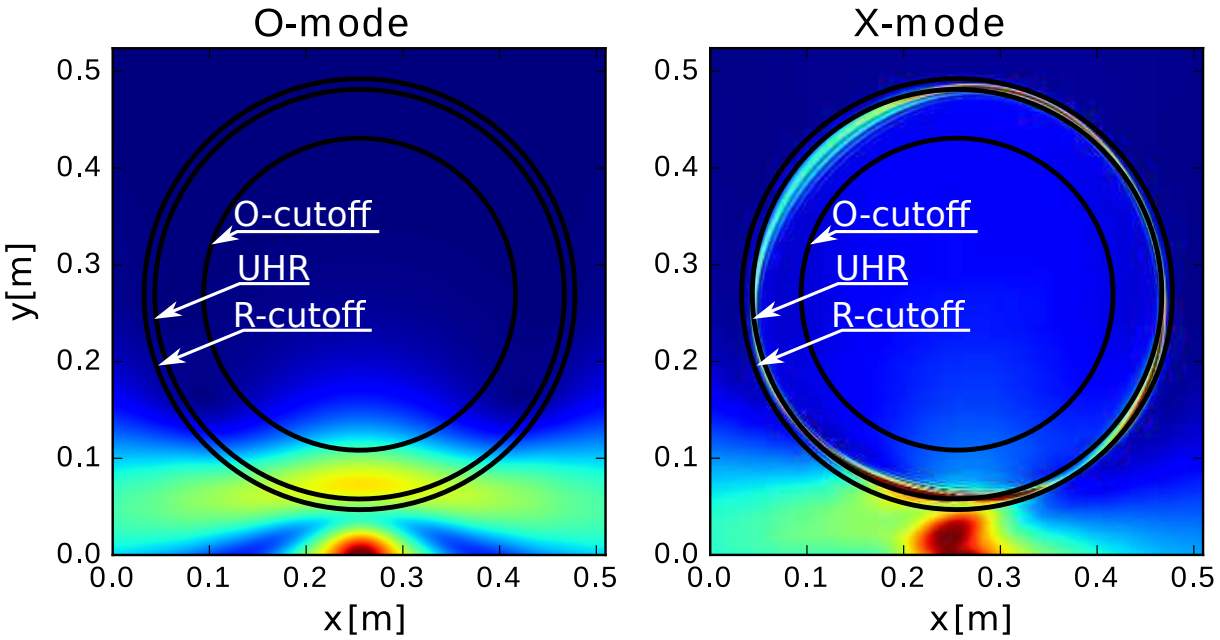

Figure 4.6: FDTD simulations of O-mode (left) and X-mode (right) propagation in FLiPS in the central poloidal plane without the vessel wall.

The absorption obtained from the simulations is compared to the analytical Budden theory in Fig. 4.7. According to Budden formula (4.9), the tunnelling reaches the maximum of 25% while the simulations show the maximum of around 40%. Since the SX-mode passes a second time through the UHR the extended Budden formula (4.10) should be used. Indeed, in this case, the calculations match the simulations more closely. The simulated values lie slightly lower because of the beam divergence, which is neglected in the Budden theory, as well as the X-mode oblique propagation with respect to the density gradient. This confirms that the grid resolution was chosen properly and that the simulations were long enough for the steady state to be achieved.

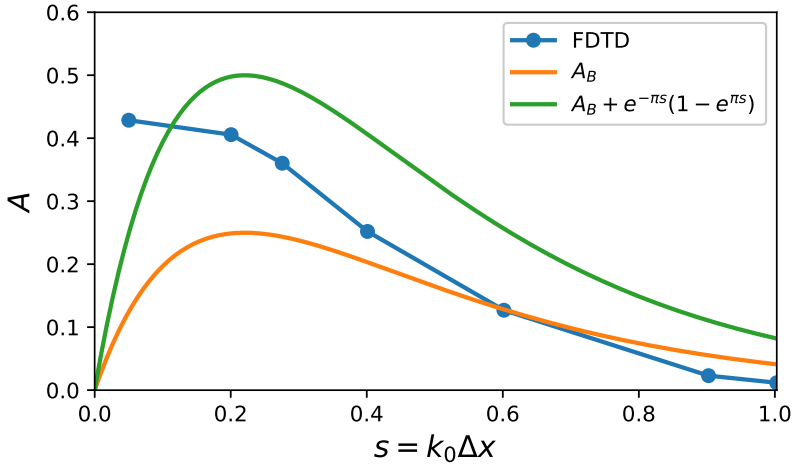

Figure 4.7: Absorption efficiency A of the X-mode by the plasma in the poloidal plane. Δx is the distance between the UHR and R-cutoff. The absorption obtained from the FDTD simulations shows a reasonable match with the extended Budden formula (4.10).

Now the same problem will be considered, but with the vessel wall included as shown in Fig. 4.8. In this case, the O-mode (Fig. 4.8 (left)) is guided between the wall and the O-cutoff, with no propagation inside the overdense plasma. The resulting standing wave pattern is reminiscent of the whispering-gallery mode as well as of the $TM_{10,1}$ mode [63] in a circular waveguide.

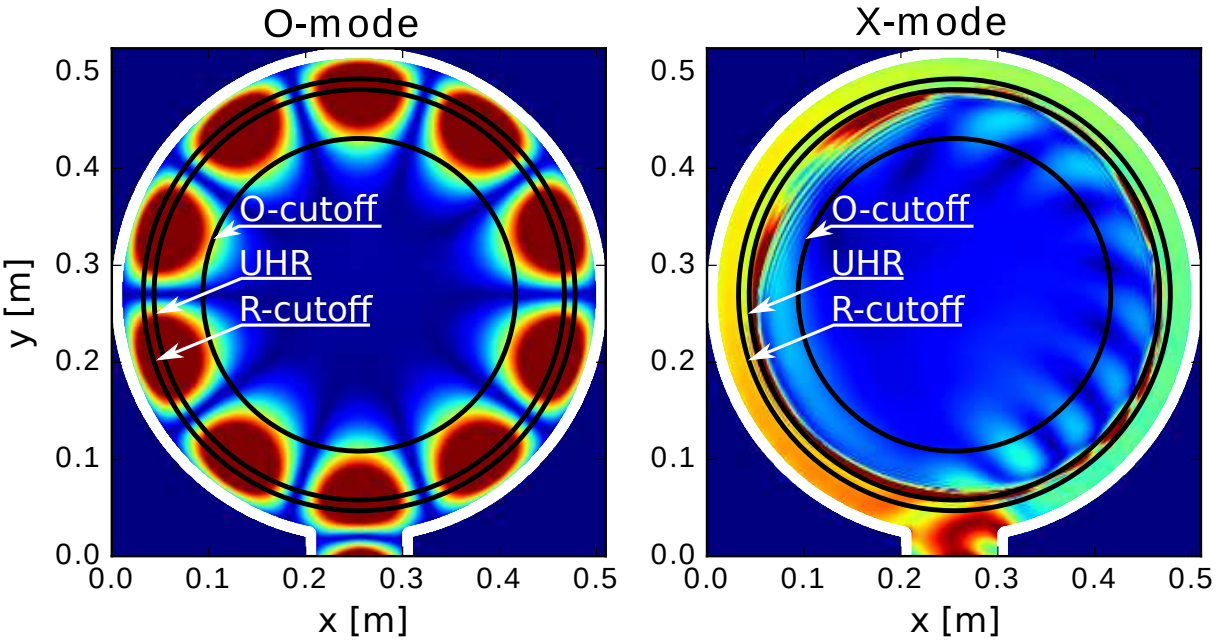

Figure 4.8: FDTD simulations of the wave propagation in FLiPS in the central poloidal plane with the vessel wall. Left: O-mode, right: X-mode.

Now, the X-mode propagation in the plasma bounded by the vessel wall will be discussed. The corresponding field is shown in Fig. 4.8 (right). The field pattern is asymmetric unlike in the case of the O-mode injection, and there is a strong amplification of the field around the UHR layer. There are two wavelength scales inside the plasma enclosed by the UHR layer. The standing wave pattern with the larger wavelength is caused by the SX-mode. The other oscillations have a smaller wavelength, and also present in the simulation without the vessel wall as shown in Fig. 4.6. In the simulations, these osculations propagate towards the dense plasma from the UHR. According to the Budden theory, the SX-mode passing through the UHR is partially absorbed and partially transmitted as the FX-mode without reflection. Thus, these oscillations could be caused by the FX-mode reflected from the walls. However, these small oscillations are also present in the simulations without the vessel wall. Since the simulations were performed for the cold plasma model, there were no EBWs that have a small wavelength compared to the cold plasma waves. Therefore, it is unlikely that these oscillations can be attributed to the plasma waves. It was also observed that the simulations would become unstable after these small scale oscillations spread through the plasma. Thus, these oscillations are likely to be a numerical artefact caused by the FDTD scheme.
The vessel wall strongly affects the conversion efficiency, as was first shown in [56]. Indeed, as depicted in Fig. 4.9, A_{tot} is an oscillating function of the parameter $s = k_0 \Delta x$. A similar phenomenon is discussed in Ch. 5, where the resonance effect arises due to the L-cutoff presence in the plasma. Here, it was shown that even in the absence of the L-cutoff, there is still a resonator effect, due to the wall reflections. Thus, the coupling to the EBWs will be sensitive to the density fluctuations that can be caused by the turbulence. In the case

of the X-mode propagation with the walls included, $A_{tot} \approx 0.5$, which is higher than the value of A_{tot} without the vessel wall.

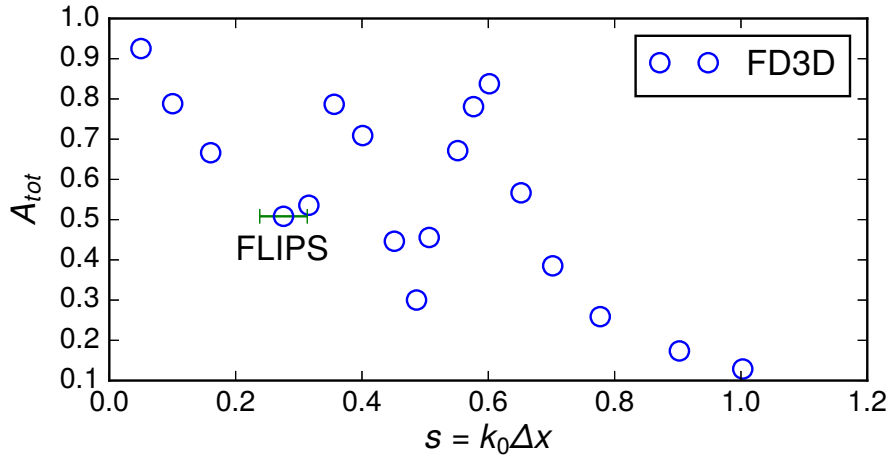

Figure 4.9: A_{tot} of the FX-mode in the FLiPS plasma bounded by the vessel wall as obtained from the FDTD simulations in the poloidal plane. The FLiPS label denotes A_{tot} for FLiPS density gradients. The horizontal error bar shows spread of the value of s due to the central density fluctuations.

4.6.2 Simulations in the axial plane

Fig. 4.10 shows FDTD simulations for the wave propagation in the axial plane of the FLiPS plasma.

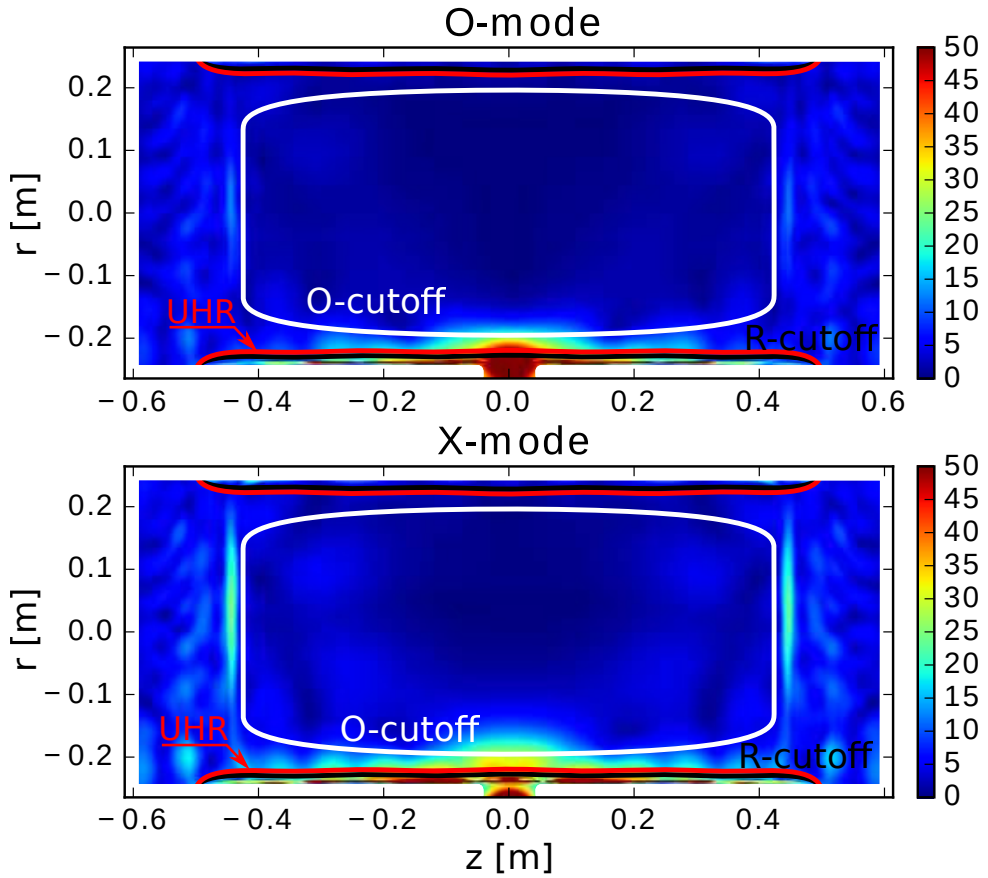

Figure 4.10: rms values of the electric field of the waves propagating in the FLiPS plasma in the axial plane. *Top:* O-mode injection, *Bottom:* X-mode injection.

The radial plasma distribution is the same as in Fig. 4.8. There are a few substantial differences compared to the previous simulations in the $z = 0$ plane. In the $z = 0$ plane, the injected waves can propagate in the space between the vessel and the plasma column, as shown in Fig. 4.8. In the axial plane simulations, the plasma is slab-like and the waves can reach the side opposite to the antenna only by passing through the plasma.
In the previous simulations, the antenna could radiate the pure modes and there was no coupling between them. In the axial simulations, the antenna always radiates a mixture of the modes since the waves propagate obliquely to the background magnetic field owing to the broad angular spectrum of the antenna. Thus, saying that the antenna radiates a particular mode, should be understood as that the antenna radiates predominantly this mode.
Since the modes propagate at oblique angles with respect to the magnetic field, there is a coupling between the modes at the O-cutoff. This explains the observed field amplification around the UHR for the O-mode launch. Since in the axial direction there is also a density gradient, the component $\vec{E}_z \parallel \vec{B}_0$ will lead to the charge separation [17] and the field amplification around the O-cutoff and to a weak absorption by collisions [60, 17]. This absorption of the wave at the O-cutoff can lead to plasma heating and sometimes is referred to as non-resonant heating [64, 65].
Now, the wave propagation will be investigated in the case without the vessel wall to compare the results of the simulations against the analytical theory. It allows finding the proper grid resolution to resolve the different wave scales, and the optimal durations of the simulations.
To perform the comparison the transmission and reflection coefficients are calculated by considering a small enclosure around the UHR, similar to the poloidal case shown in Fig. 4.4 (b). The reflection coefficient R obtained from the simulations is shown in Fig. 4.11 (left). As expected R decreases for small s. The numerically found transmission

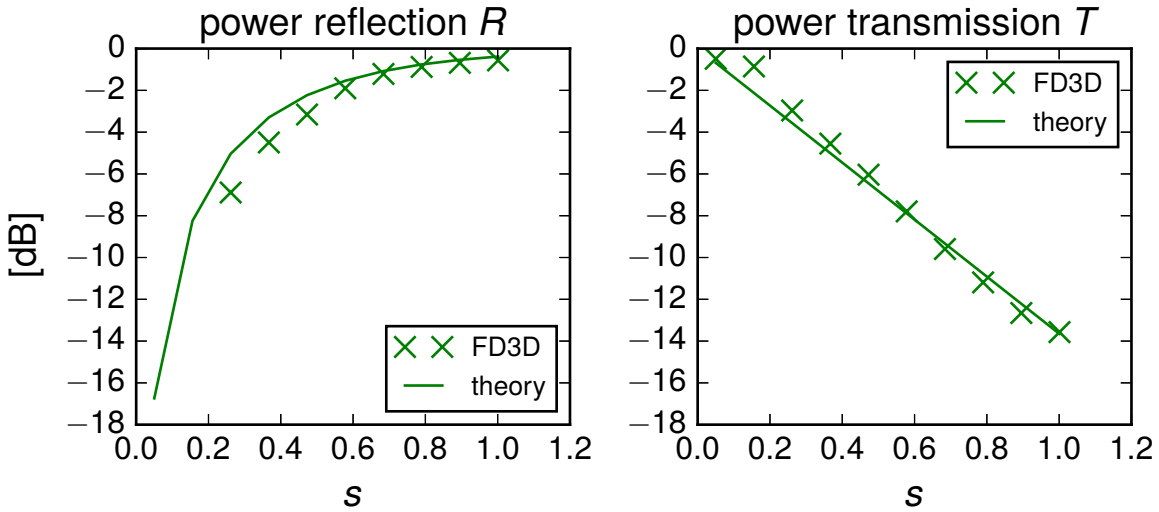

Figure 4.11: Reflection and transmission coefficients of the X-mode propagation in the axial plane without the vessel wall. The largest discrepancy between the theoretical and simulated values is found for the small distance between the UHR and R-cutoff, since in this case the grid resolution is insufficient. Other processes such as the spurious reflection from the boundaries, beam divergence and linear resonance further contribute to the discrepancy. In this simulation the total running time was 290 cycles and $n_{ppc} = 512$, which means that the grid was 2539 by 1076 points. It appears to be that the numerically found transmission coefficient matches the theory more closely than for the reflection.

coefficient T characterises the portion of the wave energy that entered the plasma without being reflected, and is shown in Fig. 4.11 (right). As expected the incoming FX-mode energy is effectively transmitted through the R-cutoff, when s is small. Both R and T

are compared to the theoretical values from [60, 20] to establish that the simulation parameters (grid resolution and the duration) were chosen properly. It can be observed that the value of R diverges from the theoretical values for the steep density gradients, which correspond to the small distances between the R-cutoff and the UHR. For the experimentally measured profile shown in Fig. 3.7 the difference is less than 1 dB.
A comparison of the absorption coefficient for the O-mode and X-mode is shown in Fig. 4.12. The X-mode absorption obtained from the simulations closely matches the prediction by Eq. (4.10), and as expected is much higher than the O-mode absorption. The negative values of the O-mode absorption coefficient are explained by the duration of the simulations, which were not long enough to fully reach the steady state. However, the negative values are small, which shows that steady state was practically achieved. The O-mode absorption also shows a wave matching effect as A_{tot} shows a periodic dependency on s. Thus, the grid resolution was sufficient and the simulation duration was long enough for the steady state to be reached, and the simulations with the vessel wall included can be performed.

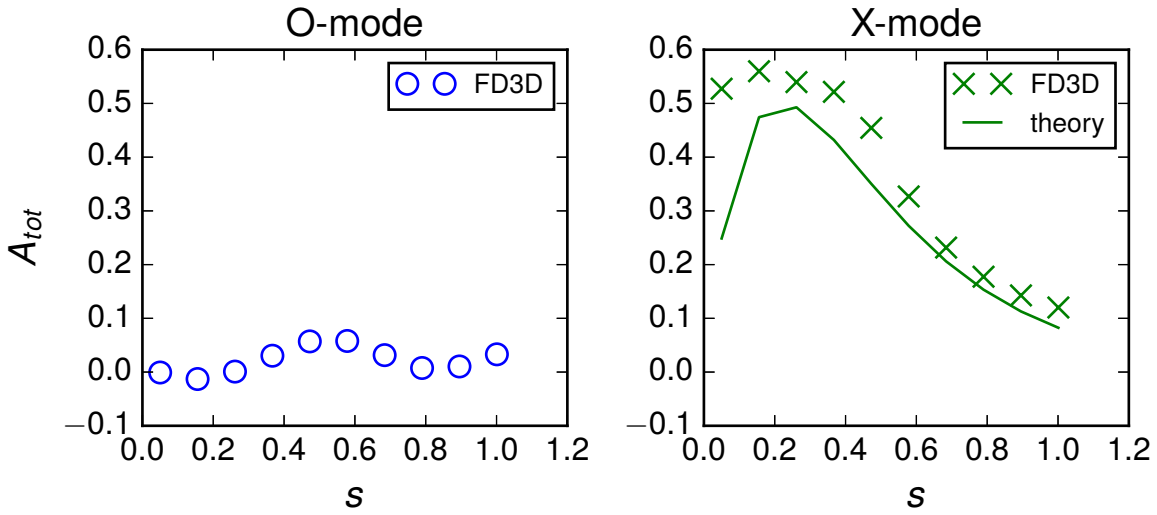

Figure 4.12: The left and right figures show the absorption of the O-mode and X-mode by the plasma without the vessel wall, respectively. As expected in the X-mode case the absorption is much higher than for the O-mode. The O-mode absorption is explained by the coupling between the modes.

When the vessel wall is included A_{tot} is shown in Fig. 4.13. Both modes suffer much higher absorption than in the previous case without the vessel wall. The value of A_{tot} of both modes are similar to each other. This means that in the experiments a noticeable difference between the O- and X-mode is not expected.
For shallow density gradients the O-mode heating can be even more efficient than the heating by the X-mode. The reason is that the R-cutoff is closer to the edge than the O-mode. Thus, the incoming FX-mode will be efficiently reflected back into the waveguide. The O-mode is able to penetrate further into the plasma. And after the multiple reflections and polarisation scrambling, it will be finally absorbed at the UHR. Thus, the difference between the O- and X-mode antenna orientation is not very large due the multiple reflections and the polarisation scrambling. In these simulations, the vessel ports were not taken into account, which could further amplify the polarisation scrambling. Inclusion of the ports requires 3D simulations, which would significantly complicate the simple cylindrical model of the vessel.

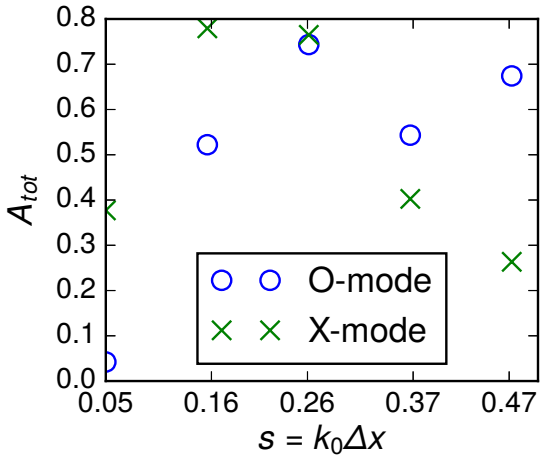

Figure 4.13: Absorption of X- and O-modes in the FLiPS plasma with the vessel wall included in the axial plane obtained from the full-wave simulations as a function of the distance between the R-cutoff and the UHR $k_0 \Delta x$.

4.7 Summary

The auxiliary heating in FLiPS was investigated using the full-wave method FDTD. Despite the fact that the code uses the cold plasma approximation, the coupling efficiency to the EBWs can be obtained from the value of A_{tot} of the SX-mode at the UHR.
The simulations were performed in the $z = 0$ and the axial planes. The absorption at the UHR was found to be in the agreement with the Budden theory, showing that the FDTD method allows simulation of the tunnelling process.
For the first time, the FX-mode absorption by a bounded magnetised plasma was investigated as a function of the plasma density gradient. It allowed a quantitative investigation of the accuracy of the method. The investigation showed that the method can become inaccurate for steep density gradients. However, for the experimentally measured profile, the discrepancy is less than 1 dB. To increase accuracy one could increase the grid resolution even further at the cost of the computational time or implement a local refinement of the grid [66].
It was shown that even in the absence of the L-cutoff the resonator effect still significantly modifies A_{tot} as shown in Fig. 4.9. Thus, the edge density fluctuations may strongly affect the coupling to the EBWs even in the absence of the intrinsic RL-resonator.
The simulations showed that in the $z = 0$ plane the coupling efficiency of the FX-mode to the EBWs is more than 50%. In the axial plane, the existence of the resonant absorption due to the axial density gradient was found. The O-mode and X-mode heating in the axial plane are practically indistinguishable, due to the multiple wall reflections and the polarisation scrambling, with a resulting value of $A_{tot} \approx 0.7$.

Chapter 5

Boundary Value Problem for wave propagation

In the last chapter, the problem of coupling to the EBWs was investigated using the FDTD method. The coupling efficiency to the EBWs was calculated for the O- and X-mode heating scenarios. However, the EBWs were not explicitly included in the previous simulations, and also some disagreement between the theoretical predictions and the FDTD simulations was found. It motivated an application of another numerical scheme to investigate the coupling to the EBWs and the effect of the collisions on them.
In this chapter, the EBW propagation will be investigated, using another full-wave method in the frequency domain. In the frequency domain, all variables oscillate harmonically at the same frequency. A system in this state is said to be in a steady state. When using the FDTD method, as noted in the previous chapter, the simulations must run long enough to ensure that the steady state is achieved and the obtained C_{eff} does not change any further.
In the frequency domain, the EBWs can be included in the simulations using the finite Larmor radius approximation as described in Sec. 2.3.3. The EBW propagation and FX-SX coupling was investigated in the frequency domain in [67, 68, 69]. Inclusion of the EBWs in the FDTD simulation is also possible, but strictly speaking, requires the use of the recursive convolution method to obtain the correct plasma response. However, by mixing the Fourier transformed terms with the terms in the time domain, one still can perform FDTD simulations of EBWs [70].
In this chapter, the O-X and FX-SX coupling will be first investigated in the cold plasma approximation. As in the FDTD simulations, the SX-mode will be damped by collisions at the UHR. The calculations of the conversion efficiency as a function of both launch angle and density-gradient length will be presented. Finally, a system of ordinary differential equations will be developed to describe the EBWs propagation in the UHR vicinity. It will allow investigation of the effect of collisional damping on the EBWs.
A few complications arise, when one works in the frequency domain. First, all resonances must be resolved by including some dissipation process, otherwise there are no steady state solutions. And secondly, in the frequency domain some solutions may be unphysical. To elaborate more on the existence of the unphysical solutions, consider the wave equation in the frequency domain, i.e. the Helmholtz equation

$$\frac{d\phi^2}{dx^2} + k_0^2 \epsilon(x)\phi = 0, \tag{5.1}$$

which is a second order ordinary differential equation. Thus, its general solution can be constructed as a sum of two linearly independent solutions

$$\phi(x) = c_1\phi_1(x) + c_2\phi_2(x), \tag{5.2}$$

where the constants c_1 and c_2 are yet to be determined. As there are two unknown constants, two additional conditions are needed to specify them. If $\phi(0) = \phi_0$ and $\phi'(0) = \phi'_0$ are given, the problem is said to be formulated as the *initial value problem* (IVP). Alternatively, boundary values can be specified $\phi(a) = \phi_a$ and $\phi(b) = \phi_b$, hence the name *boundary value problem* (BVP).
Solving a problem numerically as the initial value problem is usually simpler than as the boundary value problem. But the main disadvantage of the IVP is that one of the linearly independent solutions exhibits non-physical exponentially growing behaviour in the evanescent region, obscuring the physical solution. But posing the problem as a BVP avoids this problem through enforcing proper boundary conditions.
First, the boundary conditions will be derived in order to formulate the BVP for the wave propagation in a cold plasma . Then the coupling efficiency of O-X and FX-SX processes as a function of the launch angle and the density-gradient will be investigated. Comparing the simulations with the analytical model, allows identification of a set of parameters at which the Mjølhus formula breaks down. The FX-SX simulations illustrate how small density fluctuations can significantly affect the conversion efficiency. This effect is especially pronounced for the high magnetic fields.
As the next step, the thermal correction are included, as described in Sec. 2.3.3. The proper boundary conditions are derived and simulations for the whole FX-SX-EBW process will be performed for the case of the exactly perpendicular propagation with respect to the background magnetic field. These simulations show that EBW propagation in low temperature plasmas can be strongly affected by collisions.
The method was implemented in Python with the help of the free numerical packages numpy and scipy [71]. The solutions were obtained using a boundary value problem solver also implemented in Python based on the FORTRAN code COLSYS [72].

5.1 Boundary Value Problem for a cold plasma

In this section, the BVP formulation for simulation of O-X and direct FX-SX conversion schemes is derived based on [10]. The plasma is assumed to be stationary in a constant magnetic field and with the density gradient in the $x-$direction. A density profile shown in Fig. 5.1 was used in the simulation for the O-X and FX-SX coupling and is given by Eq. (4.3) with x-coordinate replaced by $\xi = k_0 x$, where $k_0 = \omega/c$. The plasma slab lies in the region $0 < \xi < \xi_b$. Outside of this region the plasma is homogeneous with the normalised densities X_1 and X_0, respectively.
There are two principally different ways to position the antenna in the simulation domain. If the density at the left boundary $X(\xi_{UHR}) < X(\xi_a)$, where ξ_a is the antenna position, the UHR singularity is excluded from the simulation. It significantly speeds up the simulations and the collisionless plasma can be used. If $X(\xi_{UHR}) > X(\xi_a)$, the UHR singularity must be resolved by using a non-zero normalised collision frequency $Z = \frac{\nu}{\omega}$. In this case, the values of Z were typically in the range of $10^{-4} < Z < 10^{-3}$. Using the fact that the plasma is stationary and that the fields depend only on the $x-$coordinate, Ampere's and

Faraday's laws can be Fourier transformed leading to the following equations

$$\begin{cases} N_y E_z - N_z E_y - cB_x = 0 \\ \dfrac{dE_z}{d\xi} - N_z E_x + icB_y = 0 \\ \dfrac{dE_y}{d\xi} - N_y E_x - icB_z = 0 \\ N_y cB_z - N_z cB_y + (\epsilon_{xx} E_x + \epsilon_{xy} E_y) = 0 \\ \dfrac{d}{d\xi} cB_z - iN_z cB_x - (-\epsilon_{xy} E_x + \epsilon_{xx} E_y) = 0 \\ \dfrac{d}{d\xi} cB_y - iN_y cB_x + i\epsilon_{zz} Ez = 0 \end{cases} \tag{5.3}$$

Solving this system of equations for the derivatives, the system can be written in a compact matrix form

$$\frac{d\vec{F}}{d\xi} = i\bar{\bar{A}}\vec{F}, \tag{5.4}$$

where

$$\bar{\bar{A}} = \begin{bmatrix} -N_y\epsilon_{xy}/\epsilon_{xx} & 0 & N_y N_z/\epsilon_{xx} & 1 - N_y^2/\epsilon_{xx} \\ -N_z\epsilon_{xy}/\epsilon_{xx} & 0 & N_z^2/\epsilon_{xx} - 1 & -N_y N_z/\epsilon_{xx} \\ -N_y N_z & N_y^2 - \epsilon_{zz} & 0 & 0 \\ \epsilon_{xx} + \epsilon_{xy}^2/\epsilon_{xx} - N_z^2 & N_y N_z & -N_z\epsilon_{xy}/\epsilon_{xx} & N_y\epsilon_{xy}/\epsilon_{xx} \end{bmatrix} \tag{5.5}$$

and

$$\vec{F} = \begin{bmatrix} E_y \\ E_z \\ cB_y \\ cB_z \end{bmatrix} \tag{5.6}$$

Equation (5.4) is the full-wave differential equation to be solved subjected to the proper boundary conditions which will be derived in the following. The idea is to place the plasma slab with varying density gradient between the regions where the plasma is homogeneous. If the plasma is also homogeneous in the $x-$direction, Eq. (5.4) can be Fourier transformed leading to a system of equations written in the following form

$$(\bar{\bar{A}} - N_x\mathbf{I})\vec{F} = 0, \tag{5.7}$$

where $\mathbf{I}$ is a unit matrix. To have a solution for matrix equation (5.7), the determinant $\det(\bar{\bar{A}} - N_x\mathbf{I})$ has to vanish. This condition leads to the quadratic equation for N_x^2

$$\epsilon_{xx} N_x^4 + BN_x^2 + C = 0, \tag{5.8}$$

where

$$\begin{aligned} B &= 2N_y^2\epsilon_{xx} + N_z^2(\epsilon_{xx} + \epsilon_{zz}) - \epsilon_{xx}^2 - \epsilon_{zz}\epsilon_{xx} - \epsilon_{xy}^2, \\ C &= N_y^4\epsilon_{xx} + N_y^2 N_z^2\epsilon_{xx} + N_y^2\epsilon_{zz}N_z^2 - N_y^2\epsilon_{xx}^2 - N_y^2\epsilon_{zz}\epsilon_{xx} - N_y^2\epsilon_{xy}^2 \\ &\quad + N_z^4\epsilon_{zz} - 2N_z^2\epsilon_{zz}\epsilon_{xx} + \epsilon_{xx}^2\epsilon_{zz} + \epsilon_{xy}^2\epsilon_{zz}, \end{aligned}$$

where two solutions are given by

$$N_x^2 = \frac{-B \pm \sqrt{B^2 - 4AC}}{2\epsilon_{xx}} \tag{5.9}$$

In Eq. (5.9) the "±" sign corresponds to two possible eigenmodes, thus in total there are four eigenvalues which is consistent with the Appleton-Hartree dispersion relation ginen by Eq. (2.17). To simplify the following algebra it is convenient to introduce the polarisation vectors

$$\vec{P}_i = \frac{\vec{F}_i}{E_y} = \begin{bmatrix} 1 \\ E_z/E_y \\ cB_y/E_y \\ cB_z/E_y \end{bmatrix} = \begin{bmatrix} 1 \\ \alpha_i \\ \beta_i \\ \gamma_i \end{bmatrix} \tag{5.10}$$

As the eigenvectors are linearly independent, any plasma wave can be presented as follows

$$\vec{F} = \sum_{i=0}^{4} c_i \vec{P}_i \tag{5.11}$$

where c_i are complex numbers. The coefficients $c_{1,3}$ and $c_{2,4}$ correspond to the + and − eigenmodes propagating to the right and left respectively.
Having found N_x^2, the boundary conditions can be specified by arguing that at the boundary points the solution of Eq. (5.4) must be continuous. That is, the solutions in the region of the varying density are smoothly connected to the solutions in the regions of the constant density (Fig. 5.1). Having found the vector $\vec{F}$, the remaining components E_x and cB_x can be calculated using Ampere's and Faraday's laws. From Ampere's law the E_x component is

$$E_x = -\frac{\epsilon_{xy}}{\epsilon_{xx}} E_y \tag{5.12}$$

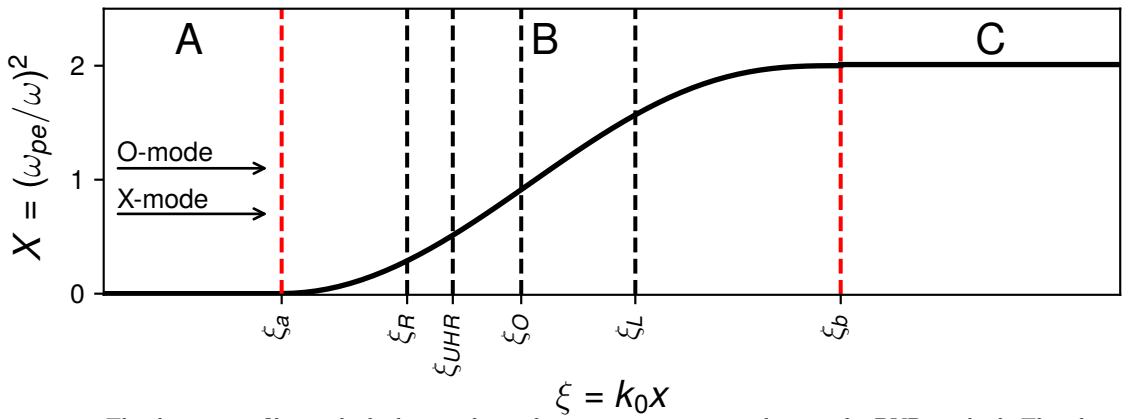

Figure 5.1: The density profile in which the coupling schemes were investigated using the BVP method. The plasma slab with the increasing density lies in the region **B** ($\xi_a < \xi < x_b$). The plasma in the regions **A** and **C** is homogeneous with densities X_1 and X_0, respectively. The density- gradient length L_O can be varied by changing position ξ_b. For larger values of ξ_b the density-gradient length is larger as well.

5.1.1 O-SX conversion scheme

Using the polarisation vectors $\vec{P}_i$ derived above, the BVP for the case of O-mode launching can be formulated. The left boundary is given by the following equation

$$c_1 \begin{bmatrix} 1 \\ \alpha_1 \\ \beta_1 \\ \gamma_1 \end{bmatrix} + c_2 \begin{bmatrix} 1 \\ \alpha_2 \\ \beta_2 \\ \gamma_2 \end{bmatrix} + c_3 \begin{bmatrix} 1 \\ \alpha_3 \\ \beta_3 \\ \gamma_3 \end{bmatrix} + c_4 \begin{bmatrix} 1 \\ \alpha_4 \\ \beta_4 \\ \gamma_4 \end{bmatrix} = \begin{bmatrix} E_y \\ E_z \\ cB_y \\ cB_z \end{bmatrix}, \tag{5.13}$$

where $c_1 = 1$, $c_2 = 0$ and c_3,c_4 are to be determined. Physically, it means that at the left boundary there are an incoming O-mode and reflected O- and X- modes propagating to the left. Eliminating c_3 and c_4 leads to the following equations which determine the left boundary condition

$$\begin{cases} (\alpha_4\beta_3 - \alpha_3\beta_4)E_y + (\beta_4 - \beta_3)E_z + (\alpha_3 - \alpha_4)cB_y + \\ \qquad \beta_1(\alpha_4 - \alpha_3) + \beta_3(\alpha_1 - \alpha_4) + \beta_4(\alpha_3 - \alpha_1) = 0 \\ (\alpha_4\gamma_3 - \alpha_3\gamma_4)E_y + (\gamma_4 - \gamma_3)E_z + (\alpha_3 - \alpha_4)cB_z + \\ \qquad \gamma_1(\alpha_4 - \alpha_3) + \gamma_3(\alpha_1 - \alpha_4) + \gamma_4(\alpha_3 - \alpha_1) = 0 \end{cases} \tag{5.14}$$

At the right boundary there are no incoming waves, only outgoing possibly evanescent X- and O-modes. Thus, the right boundary conditions are given by

$$\begin{cases} (\alpha_2\beta_1 - \alpha_1\beta_2)E_y + (\beta_2 - \beta_1)E_z + (\alpha_1 - \alpha_2)cB_y = 0 \\ (\alpha_2\gamma_1 - \alpha_1\gamma_2)E_y + (\gamma_2 - \gamma_1)E_z + (\alpha_1 - \alpha_2)cB_z = 0 \end{cases} \tag{5.15}$$

With these equations the formulation of the BVP for the O-SX conversion scheme is complete.

5.1.2 Results: O-SX conversion

Figure 5.2 shows the O-X conversion obtained from the simulations and, for comparison, the analytical prediction by the Mjølhus formula (2.27). The simulations were performed for the case of a collisionless (Z=0) and collisional $Z = 10^{-3}$ plasma. The $Z = 0$ simulations show that the code functions properly since it reproduces Mjølhus formula. The $Z = 10^{-3}$ simulations also agree well with Mjølhus formula. In the latter case, the general trend of C_{eff} is preserved and $N_{z,opt}$ position is unaffected. The details on the calculation of the conversion efficiency are described in Appendix A.
The most significant difference is for $N_z \ll N_{z,opt}$. In this case, according to Mjølhus formula $C_{eff} \approx 0$. The collisions elevate the level of C_{eff} obtained from the $Z = 10^{-3}$ simulations to about 5%. This increase is caused by the O-mode collisional absorption. For the $N_z < N_{z,opz}$ the O-mode reaches a denser plasma than for more grazing launch angles corresponding to $N_z > N_{z,opz}$. In the latter case, as shown in Sec. 6.3 the O-mode gets reflected earlier, thus being less affected by the collisions. Figure 5.3 depicts the behaviour of the electric field components in the case of the optimal incidence angle. The longitudinal component E_x increases at the UHR as expected. According to the cold plasma theory, $N_x \longrightarrow \infty$, thus the wave becomes quasi-longitudinal at the UHR. The components E_y and E_z are less affected by the UHR, although the effect of the UHR on these fields is clearly visible. For the densities below the UHR, the fields are created only by the incoming O-mode. Indeed, the O-mode propagates at the optimal angle, thus there are no reflected waves such as the FX-mode or the O-mode. In the region between the UHR and the O-cutoff, the fields are created by the superposition of the incoming O-mode and the SX-mode.
The bottom part of Fig. 5.3 shows the energy flux normalized to the energy flux of the incoming O-mode. For $\xi > \xi_{UHR}$ there is almost no energy flux because all the energy that flows to the right is reflected back. For $\xi < \xi_{UHR}$ the Poynting flux remains constant because the outgoing SX-mode is damped at the UHR. Indeed, $P_x/P_{in} = 1$, which corresponds to $C_{eff} = 1$, means that there is no outgoing Poynting flux, since the total Poynting flux P_x is equal to the incoming Poynting flux P_{in}.

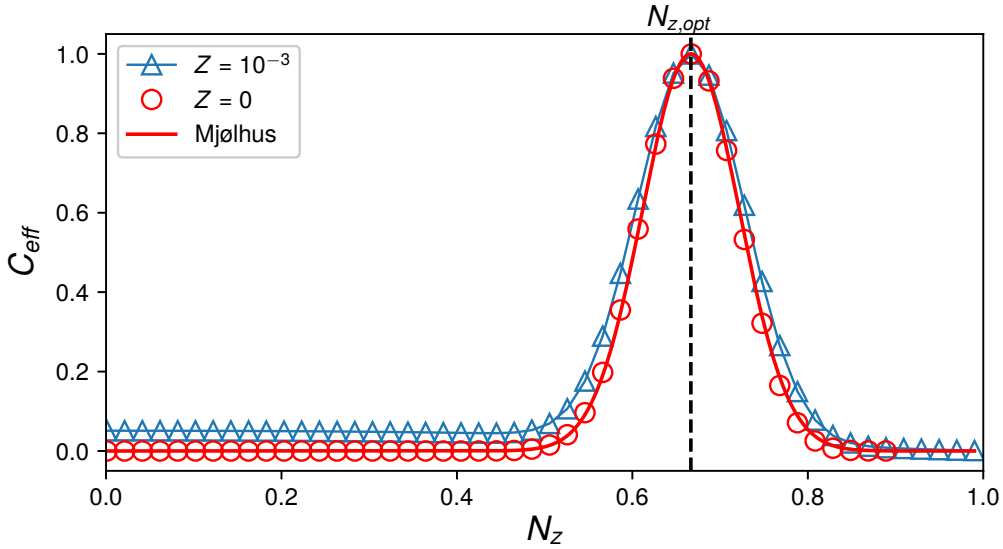

Figure 5.2: Conversion efficiency of the O-X process obtained from the BVP simulations and the analytical prediction by the Mjølhus formula. The calculations were performed for the linear density profile shown in Fig. 5.1 and the background magnetic field $Y = 0.8$. The O-mode propagates exactly perpendicular the magnetic field for $N_z = 0$ and parallel to it for $N_z = 1$. According to the Mjølhus formula, the conversion efficiency C_{eff} depends on the normalised density-gradient length $k_0 L$ and the launch angle θ of the O-mode as discussed in Sec. 2.3.1. At $N_z = N_{z,opt}$ all O-mode energy is transferred into the SX-mode, which corresponds to $C_{eff} = 1$. In the case of $Z = 0$ the antenna was placed at the position $\xi_a > \xi_{UHR}$ to exclude the UHR from the numerical domain.

Figure 5.4 shows that the Mjølhus formula does not exactly reproduce the results of the full-wave simulation for a short L_O since C_{eff} is not 100% for $N_{z,opt}$. It is explained by the fact that in the Mjølhus theory the "leakage" of the SX-mode through the UHR is not taken into account. The shorter L_O, the smaller the distance between the R-cutoff and the UHR that the SX-mode has to traverse to couple to the FX-mode. Indeed, Fig. 5.5 shows separate energy fluxes carried by the O-mode (left) and the X-mode (right). Thus, a perfect O-SX conversion does not always imply good coupling to the EBWs since a large portion of the energy can be carried away by the FX-mode propagating back.

5.1.3 FX-SX coupling

Similarly to the O-SX conversion scheme, the BVP is formulated to investigate the direct FX-SX coupling scheme.
At the left boundary there are an incoming FX-mode and reflected O- and X-modes, thus the left boundary conditions are

$$\begin{cases} (\alpha_3\beta_4 - \alpha_4\beta_3)E_y + (\beta_3 - \beta_4)E_z + (\alpha_4 - \alpha_3)cB_y \\ \qquad + \alpha_3(\beta_2 - \beta_4) + \alpha_4(\beta_3 - \beta_2) + \alpha_2(\beta_4 - \beta_3) = 0 \\ (\alpha_3\gamma_4 - \alpha_4\gamma_3)E_y + (\gamma_3 - \gamma_4)E_y + (\alpha_4 - \alpha_3)cB_z \\ \qquad + \alpha_3(\gamma_2 - \gamma_4) + \alpha_4(\gamma_3 - \gamma_2) + \alpha_2(\gamma_4 - \gamma_3) = 0 \end{cases} \tag{5.16}$$

Assuming that there is no incoming energy from the right, the right boundary conditions are identical to the O-SX conversion case.

5.1.4 Results: FX-SX coupling

Figure 5.6 shows the FX-SX coupling efficiency C_{FX-SX} for the almost perpendicular injection angle obtained by solving the BVP formulated above.

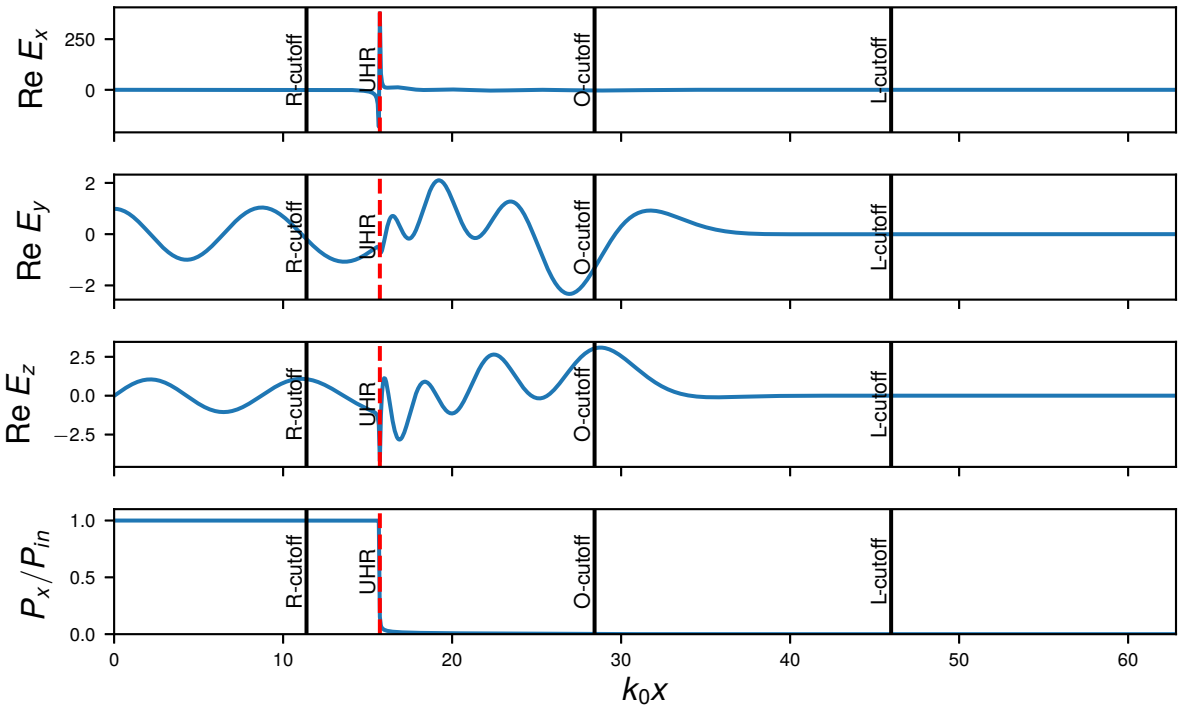

Figure 5.3: The BVP simulation of the O-X conversion process for the optimal injection. The electric field component most affected by the UHR is the longitudinal E_x component which is strongly amplified at the UHR. Between the UHR and the O-cutoff, E_y and E_z components show the presence of a short wavelength wave. This wave is the SX-mode into which the incoming O-mode was converted at the O-cutoff.
The bottom figure shows the total Poynting flux P_x normalised to the incoming Poynting flux P_{in}. Since the incoming O-mode was launched at θ_{opt}, its energy is completely transformed into the SX-mode which is then absorbed at the UHR. Thus, there is no outgoing Poynting flux between the left plasma boundary and the UHR. In this case, the UHR acts as a local "black body" [73]. For the densities above the UHR, the total Poynting flux vanishes since the Poynting flux carried by the O-mode to the right is compensated by the equal Poynting flux of the SX-mode propagating to the left.
For the densities above the L-cutoff all the electric field components are evanescent in agreement with the cold plasma theory.

The results of the simulations are compared to the theoretical prediction given by Eq. (2.31) without the phase factor $\cos\left(\frac{\phi}{2}+\theta\right)$. Without the phase factor, Eq. (2.31) describes the envelope that gives the maximal coupling efficiency. The results show that at low magnetic fields the modulation is smaller. The modulation becomes a problem in turbulent plasmas, where the density fluctuations can significantly modify the plasma density-gradient length L_{UHR} leading to an undesired deterioration of the C_{FX-SX} or difficulties in the interpretation of the experimental results.
The fields and the corresponding Poynting flux for the case of the 100% coupling efficiency are depicted in Fig. 5.7. As in the case of the O-X conversion, E_x is significantly amplified at the UHR. It implies that at the UHR vicinity, the waves become quasi-longitudinal and quasi-electrostatic. The E_y field shows that the field changes significantly over the distance comparable with the wavelength, unlike in the O-X conversion scheme, where the waves change slowly over many wavelengths. The hatched area shows the resonator formed by the R-cutoff and L-cutoff for the SX-mode. The energy flux is normalised to the incoming energy and shows total absence of the reflected wave indicating a perfect conversion. Indeed, for the densities below the UHR, the total Poynting flux $P_x = P_{in}$. It shows a complete absence of the reflected waves.
The incoming FX-mode must be able to traverse the evanescent region between the R-cutoff and the UHR in order to couple to the SX-mode. For oblique injection angles the effective distance between the R-cutoff and the UHR that the FX-mode has to tunnel

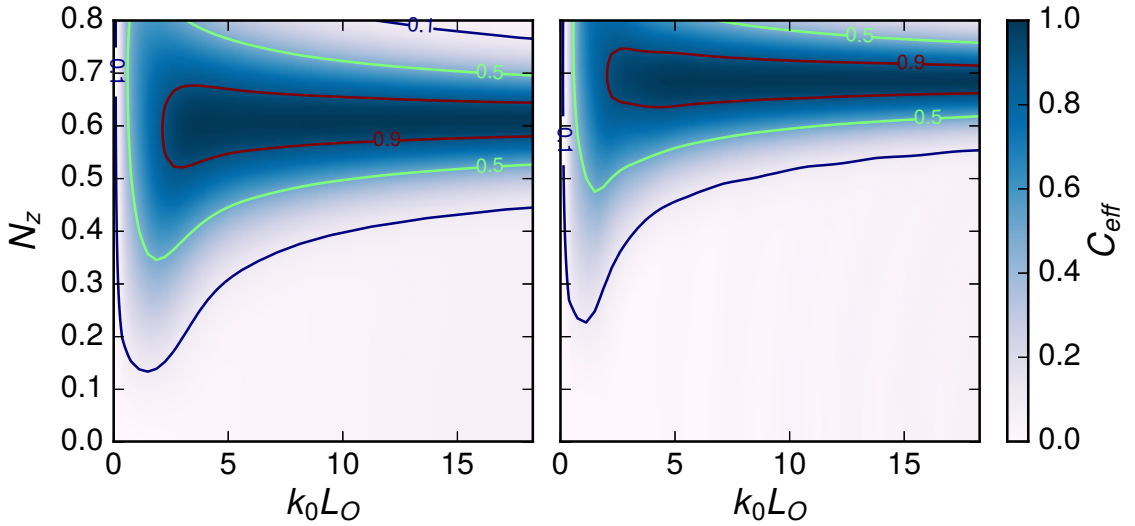

Figure 5.4: Contour plots of the O-X conversion efficiency as a function of the parallel refractive index N_z and the density-gradient length L_O for magnetic fields $Y = 0.6$ (left) and $Y = 0.9$ (right).

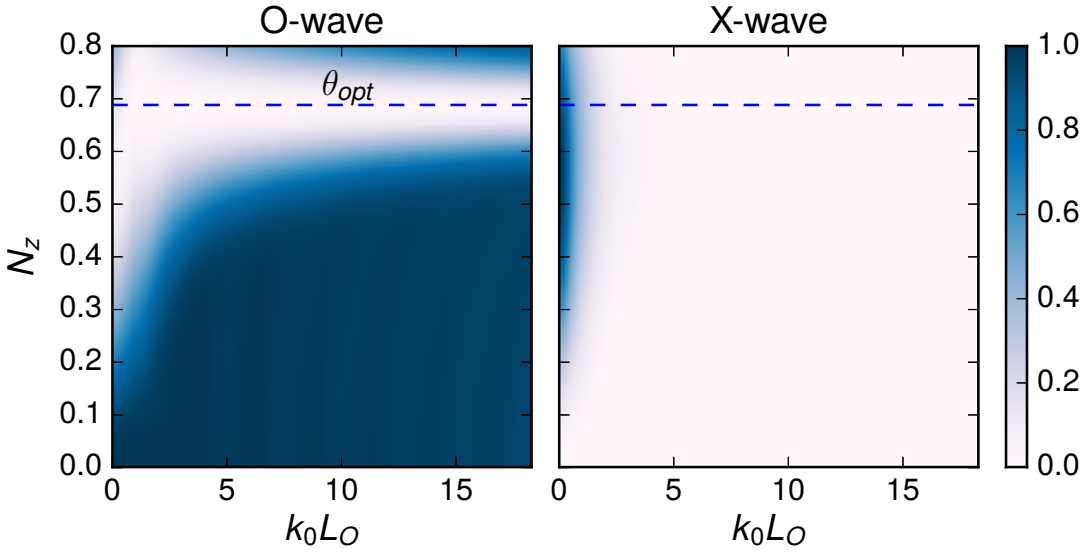

Figure 5.5: Left: normalised reflected energy flux carried by the O-mode. Far from θ_{opt} the O-mode does not couple to the X-mode and is reflected as an O-mode. Right: normalised reflected energy flux carried by the X-mode. For steep density-gradients the O-mode is reflected back as an X-mode due to the leakage of the SX-wave through the UHR.

through increases which decreases the coupling efficiency. The distance between the R-cutoff and the UHR depends on the density-gradient length. For steep density gradients, the distance is smaller compared to the case with shallow density gradients, which leads to an efficient tunnelling of the FX-mode through the region between the R-cutoff and the UHR.

To study C_{FX-SX} as a function of both injection angle given by N_z and the density-gradient length L_{UHR}, multiple simulations were performed for different values of N_z and fixed values of L_{UHR}. The result is a 2D plot of the coupling efficiency shown in Fig. 5.8. As expected C_{FX-SX} in general decreases for larger N_z. The modulation of C_{FX-SX} caused by varying N_z is much smaller than due to varying L_{UHR}. In the case of $Y = 0.9$ the increase of N_z can lead to a slight improvement of C_{FX-SX}.

A significant coupling of the SX-mode to the O-mode can occur in the case of FX-mode injection when the density gradient is very steep. Decomposing the field at the antenna plane into the O- and X-mode, the result shown in Fig. 5.9 is obtained. The SX-O cou-

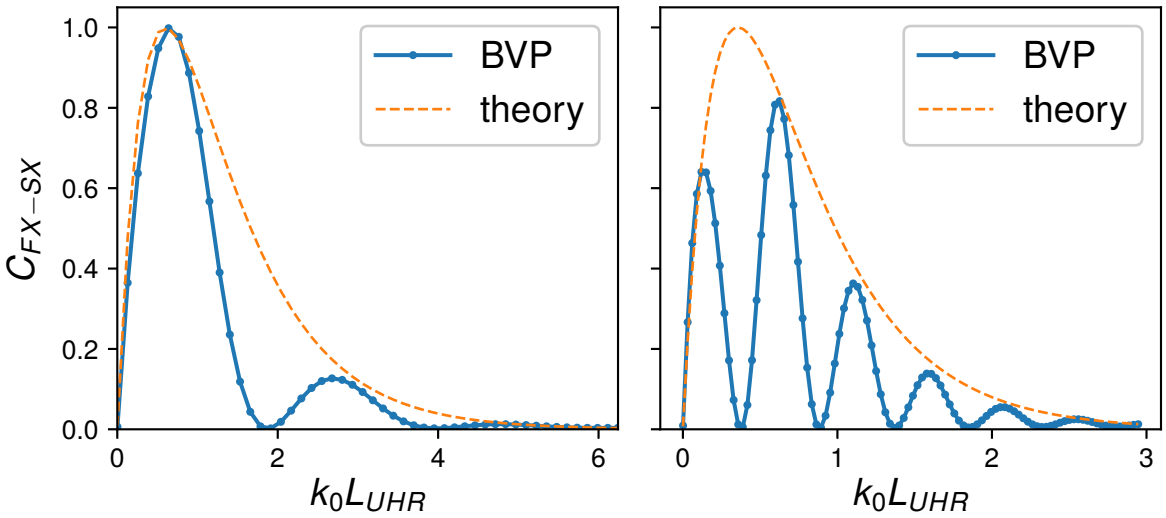

Figure 5.6: The coupling efficiency C_{FX-SX} of the FX-SX coupling for two magnetic fields. Plasma parameters are: (left) $Y = 0.6$, $Z = 10^{-4}$, (right) $Y = 0.9$, $Z = 10^{-4}$. Notice a strong modulation of C_{FX-SX} efficiency for $Y = 0.9$. The theoretical prediction is given by Eq. (2.31) without the phase factor.

pling for steep density gradients has the maximum at $N_z \approx 0.69$, which is the optimal N_z for the O-SX conversion scheme for the given magnetic field. When the density-gradient length increases, the SX-O coupling drops sharply. The SX-O coupling efficiency is higher for the steep density gradients due to the smaller spacing between the O- and L- cutoff. Indeed, as was shown in Sec. 2.3.1, the O- and X-mode refractive indices coincide whenever $N_z = N_{z,opt}$ and $N_x = 0$. Thus, when the SX-mode reflects close to the O-cutoff, an efficient coupling between the two modes occurs.

5.2 Comparison of O-SX and FX-SX schemes

In the previous discussion, the FX-SX coupling was investigated as a function of the density-gradient length at the UHR. To be able to compare the O-FX and FX-SX schemes, the efficiency of both schemes was plotted as a function of the density-gradient length at the O-cutoff in Fig. 5.10. Here, a brief summary of the main differences between the schemes is given. FX-SX scheme is more sensitive to gradient length changes than the O-X coupling scheme. The magnetic field strength also affects the coupling efficiency of the FX-SX scheme. The only significant effect of the magnetic field on the O-FX conversion scheme is the change of the optimal injection angle θ_{opt}. Both schemes are ineffective for very short density-gradient length $k_0 L_O < 1$, due to the SX-wave "leakage" through the UHR.

The FX-SX scheme is efficient for a perpendicular injection ($N_z = 0$). An antenna that launches the FX-mode is easier to implement technically than an antenna for the O-X heating since a simple open waveguide can be used as an antenna for the FX-mode injection which is a typical set-up in some FX-SX experiments [74, 75].

For the FLiPS density-gradient lengths, which were estimated to be $k_0 L_O \lesssim 3$, the O-SX conversion occurs over a broad range of N_z. Thus, both schemes are likely to heat the FLiPS plasma equally well. This conclusion is further supported by the FDTD simulations in the previous chapter.

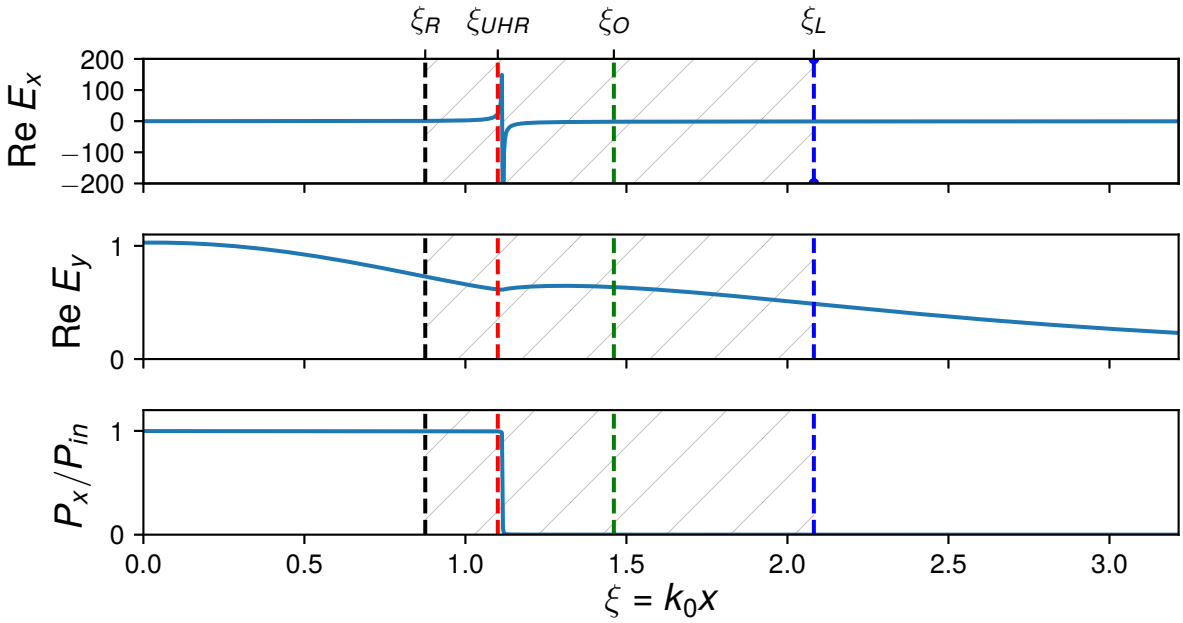

Figure 5.7: BVP simulations of the FX-SX tunnelling. The incoming FX-mode was launched perpendicularly to the background magnetic field. The corresponding electric field components are shown versus $k_0 x$. The longitudinal E_x component shows a resonant behaviour at the UHR. The bottom figure shows the Poynting flux normalised to the incoming Poynting flux P_{in}. The normalised Poyning flux demonstrates a perfect absorption of the incoming FX-mode. Plasma parameters are: $Y = 0.6$, $Z = 10^{-4}$. The hatched area indicates the boundaries of the RL-resonator.

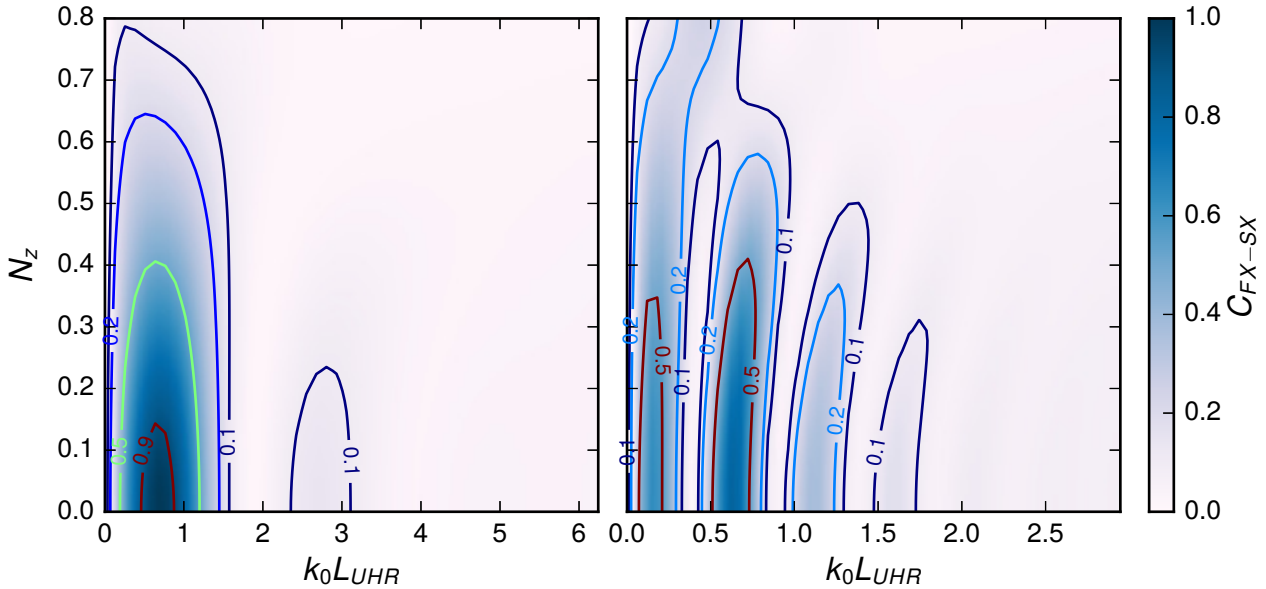

Figure 5.8: Efficiency of the direct coupling for two magnetic fields $Y = 0.6$ (left) and $Y = 0.9$ (right) as a function of the parallel refractive index N_z and the normalised density-gradient length $k_0 L_{UHR}$ at the UHR.

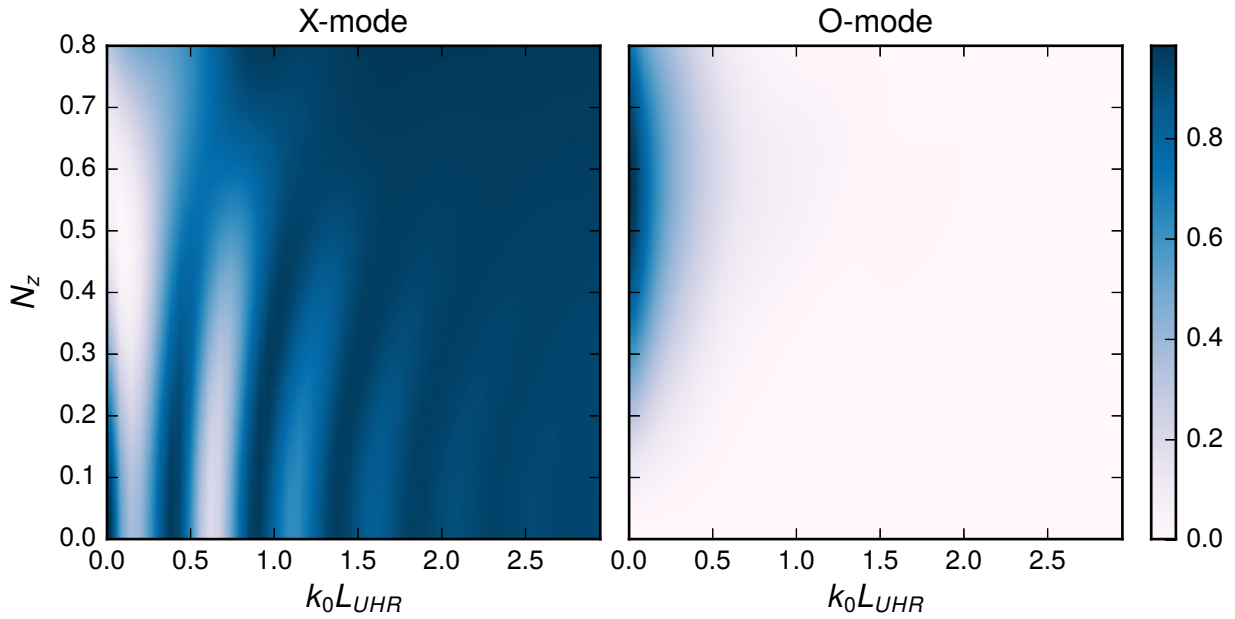

Figure 5.9: Mode decomposition of the time-averaged outgoing energy-flux carried by the X-mode (left) and the O-mode (right) in the plasma with $Y = 0.9$, $Z = 10^{-3}$. The mode decomposition shows that for very steep density gradients the incoming FX-mode injected at θ_{opt} will be reflected as an O-mode. Compare with Fig. 5.5 where the incoming O-mode was reflected as an X-mode.

5.3 Boundary Value Problem with the spatial dispersion included

In this section, the full-wave simulations of the EBWs will be carried out. To do it exactly, one would have to replace the cold dielectric tensor by the integral operator to take into account the non-locality of the response (see Eq. (2.4)). Within this approach, one calculates the plasma response, which is a rather mathematically involved task [76]. Another approach to simulate EBWs is the particle-in-cell method, where particles and interactions between them are treated explicitly [77]. This approach has received much attention recently [78, 79], since it allows a consistent inclusion of all physical processes occurring in the plasma at the cost of very demanding numerical simulations.
In this study, the EBWs will be treated approximately using a BVP formulation. The EBWs can be included into the simulations as briefly described in the following. Firstly, decomposing ϵ_{xx} given by Eq. (2.22) in ascending powers of $\lambda = \frac{1}{2}(N_x \gamma q)^2$ and taking the first two terms, the ϵ_{xx} term of the hot dielectric tensor becomes

$$\epsilon_{xx} = \epsilon_{xx}^{cold} + \chi N_x^2, \tag{5.17}$$

where

$$\chi = -\frac{3X}{(1-Y^2)(1-4Y^2)}\gamma^2 \tag{5.18}$$

The modified component of the plasma dielectric tensor ϵ_{xx} depends now on N_x, which is a consequence of the spatial dispersion or non-locality [20, 3]. As was first discussed in [32], a full-wave equation that also includes the EBWs can be obtained using the following correspondence

$$N_x^2 \longleftrightarrow -\frac{1}{k_0^2}\frac{\partial^2}{\partial x^2} \tag{5.19}$$

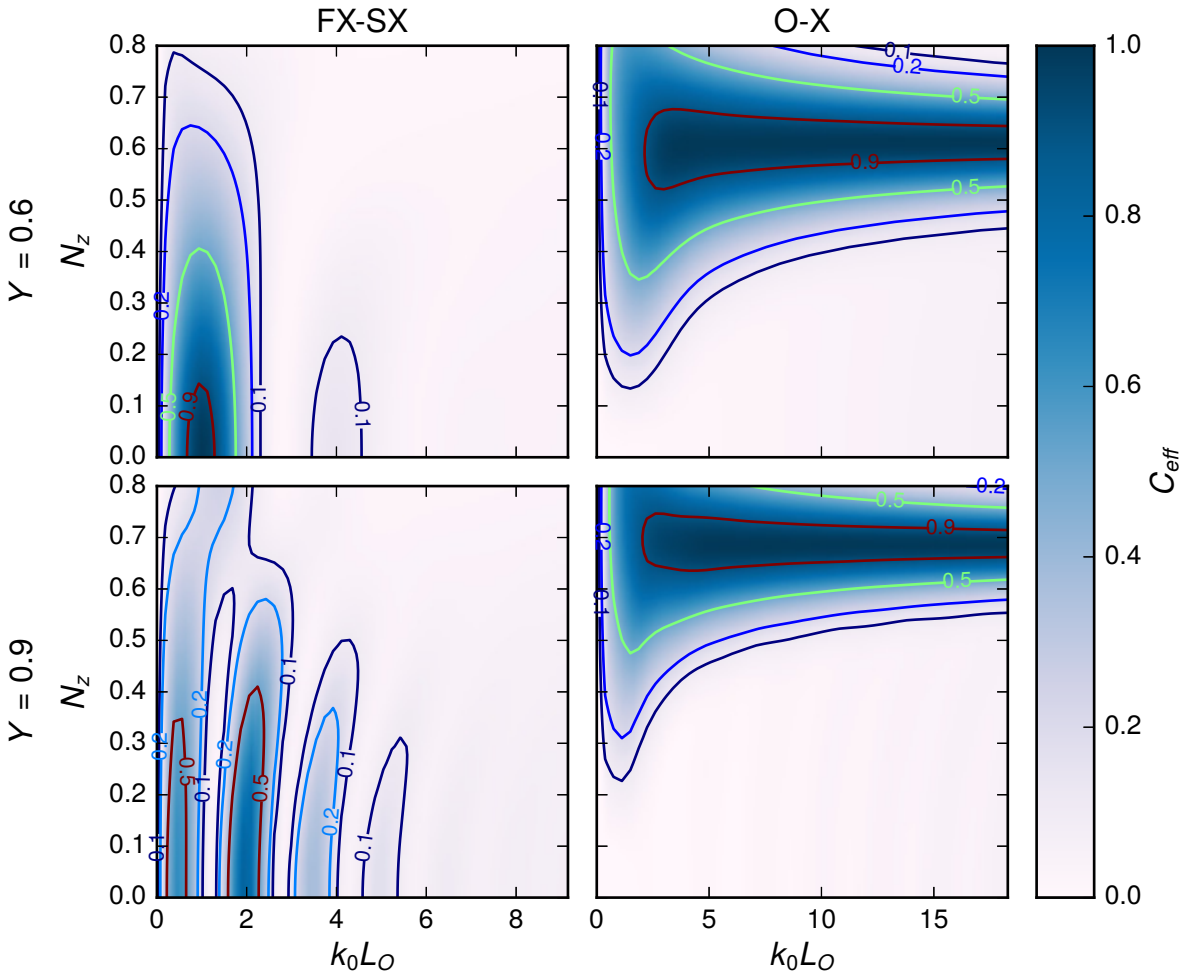

Figure 5.10: The efficiency of FX-SX and O-X schemes. The top and bottom rows show the simulations for $Y = 0.6$ and $Y = 0.9$ magnetic fields, respectively. The coupling efficiency for both schemes is plotted as a function of the normalised density-gradient length at the O-cutoff $k_0 L_O$ defined by Eq. (3.5).

As will be shown later, this increases the order of Maxwell's equations, and an additional component must be added to the field vector $\vec{F}$. This approach has already been used [32, 67, 68] to perform full-wave simulations of EBWs and allows description of the fundamental EBWs at the UHR vicinity. Indeed, as the EBWs propagate away from the UHR the refractive index keeps increasing and at some point the next term in the λ series must be included to correctly describe the wave. In this approximation the Landau damping and the cyclotron absorption are not included.

As shown in Fig. 2.13 from Ch. 2, the refractive index obtained within this model will be in general smaller than predicted by the exact hot dispersion relation. The higher EBW harmonics can be included in the simulations in the similar fashion by including the next terms of λ series, which will increase the order of Maxwell's equations further. In this thesis, only the fundamental EBWs will be simulated.

The case that will be investigated is the FX-mode propagating perpendicularly to the background magnetic field. In this case, the derivation of the boundary conditions is simplified. Indeed, when a FX-mode launched perpendicularly to the magnetic field, it will be decoupled from the O-mode, and when the EBWs are included as described above, the total number of separated modes will be two, simplifying the derivation of the boundary conditions and speeding up the calculations.

When the EBWs are included their collisional absorption can be investigated. The main

interest is the collisional absorption, since FLiPS plasma is relatively cold with $T_e \approx 10$ eV. Therefore, the EBWs are not strongly absorbed due to the Landau damping, and the collisions are the main damping mechanism. Collisional absorption can be included as the collisional frequency ν, in the same way as done in the previous sections to remove the singularity at the UHR.
Since the EBWs have a small wavelength compared to the cold plasma waves, the solver must use a very fine numerical grid to resolve the waves which makes simulations run slowly. In the worst case, the solver will not be able to find a suitable grid, when the machine precision is exceeded [80].

5.3.1 Derivation

The derivation is similar to the procedure from the previous sections, where the BVP was formulated to describe the O-SX conversion and the FX-SX tunnelling. First, a system of differential equations that describe the X-mode and EBW propagation is derived. Using Stix' notation the system of equations describing only the X-mode and EBW propagation is obtained by setting N_y and N_z to zero in Eq. (5.3)

$$\begin{cases} \dfrac{dE_y}{d\xi} = icB_z \\ \dfrac{d^2E_x}{d\xi^2} = \dfrac{1}{\chi}(SE_x - \dfrac{d\chi}{d\xi}\dfrac{dE_x}{d\xi} - iDE_y) \\ \dfrac{d}{d\xi}cB_z = iDE_x + SE_y \end{cases} \tag{5.20}$$

Compared to the cold plasma case, now there is an additional term $\frac{d^2E_x}{d\xi^2}$ due to the spatial dispersion. The system is transformed into a system of differential equations of the first order by introducing the variable e such that $e = \frac{dE_x}{d\xi}$. Its sole purpose is to re-cast the system of equations (5.20) into the system of the first order differential equations that can be solved by the same method that was applied to investigate the cold plasma case. It is convenient to re-write the system in the matrix form as follows

$$\frac{d}{d\xi}\begin{bmatrix} E_y \\ cB_z \\ E_x \\ e \end{bmatrix} = \begin{bmatrix} 0 & i & 0 & 0 \\ iS & 0 & -D & 0 \\ 0 & 0 & 0 & 1 \\ -iD/\chi & 0 & S/\chi & -\frac{1}{\chi}\frac{d\chi}{d\xi} \end{bmatrix}\begin{bmatrix} E_y \\ cB_z \\ E_x \\ e \end{bmatrix} \tag{5.21}$$

where

$$\chi = \frac{-3X}{(1-Y^2)(1-4Y^2)}\gamma^2,$$

$$\gamma = \frac{v_{th}}{c},$$

where c is the speed of light and v_{th} is the electron thermal velocity. This system of differential equations has in total four eigenvalues. After doing some algebra, it can be shown that the eigenvalues of this matrix equation correspond to the EBW and X-mode. Having the full-wave equation, the boundary conditions can be derived. The polarisation

vector is defined now as follows

$$\vec{P}_i = \frac{\vec{F}_i}{E_y} = \begin{bmatrix} 1 \\ E_z/E_y \\ cB_z/E_y \\ E_x \\ e \end{bmatrix} = \begin{bmatrix} 1 \\ \alpha_i \\ \beta_i \\ \tilde{\gamma}_i \end{bmatrix}, \tag{5.22}$$

where

$$\alpha = N_x, \tag{5.23}$$

$$\beta = i\frac{S - N_x^2}{D}, \tag{5.24}$$

$$\tilde{\gamma} = iN_x\beta \tag{5.25}$$

At the left boundary there are an incoming and an outgoing X-mode and an evanescent EBW. Skipping the algebra, the boundary conditions at the left are given by

$$\begin{cases} E_x - (\beta_1 + c_4\beta_4 + c_2\beta_2) = 0 \\ e - (\tilde{\gamma}_1 + c_4\tilde{\gamma}_4 + c_2\tilde{\gamma}_2) = 0, \end{cases} \tag{5.26}$$

where

$$c_4 = \frac{cB_z - \alpha_1 - \alpha_2(E_y - 1)}{\alpha_4 - \alpha_2}, \tag{5.27}$$

$$c_2 = E_y - 1 - c_4 \tag{5.28}$$

At the right boundary there are an evanescent X-mode and a propagating EBW. Thus, the right boundary is

$$\begin{cases} c_1\beta_{EBW} + c_3\beta_X - E_x = 0 \\ c_1\tilde{\gamma}_{EBW} + c_3\tilde{\gamma}_X - e = 0, \end{cases} \tag{5.29}$$

where

$$c_3 = \frac{E_y\alpha_{EBW} - cB_z}{\alpha_{EBW} - \alpha_X}, \tag{5.30}$$

$$c_1 = E_y - c_3 \tag{5.31}$$

The BVP has been formulated and full-wave equation (5.20) can be solved numerically.

5.3.2 Results

Figure 5.11 shows the efficiency C_{FX-B} of the complete FX-SX-EBW process obtained from the BVP simulations.
Comparing with the result obtained in Sec. 5.1.3, where only the FX-SX coupling was considered, it can be concluded that the thermal effects do not strongly modify C_{FX-SX} even for large values of γ. There exists a temperature-dependent effect which is clearly seen in the enlarged areas of Fig. 5.11. However, since the difference is marginal, Budden formula (2.31) can be used to calculate coupling efficiency to the EBWs. Now, the EBW fields in the UHR vicinity will be discussed to investigate the effects of the collisions. The

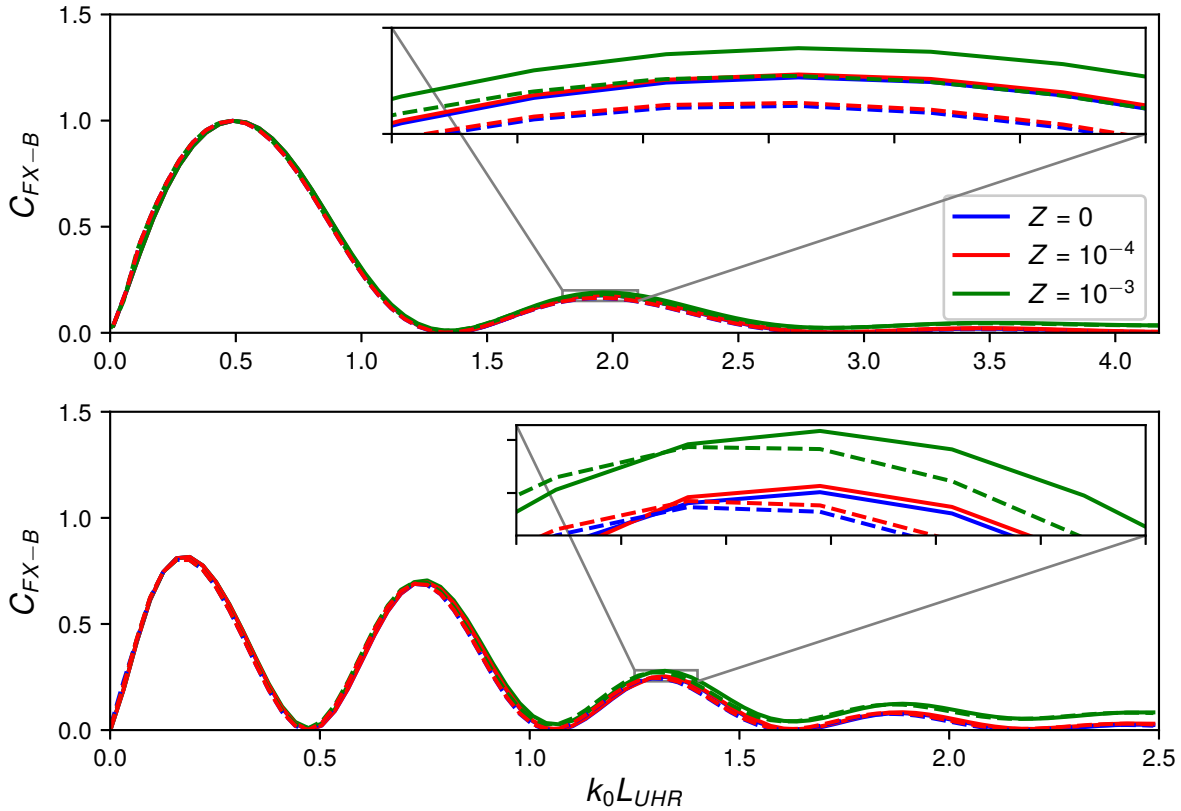

Figure 5.11: The efficiency of the complete FX-SX-EBW conversion for $Y = 0.7$ (top) and $Y = 0.9$ (bottom). The solid and dashed lines correspond to $\gamma = 0.006$ and $\gamma = 0.06$ respectively. The same color corresponds to the same normalised collisional frequency Z.

simulations were performed for plasmas with different Y, electron temperatures characterised by the parameter $\gamma = \frac{v_{th}}{c}$, and normalised collisional frequencies Z. Figures 5.12 and 5.13 show the fields that propagate in the plasmas with $Y = 0.7$ and $Y = 0.9$. The density gradients were chosen such that C_{FX-B} attains its maximum.

The effect of EBWs reveals itself most clearly in the E_x component, which is perpendicular to the background magnetic field and is the dominant component of EBWs. The other components of the field tend to decrease because the SX-wave becomes evanescent, whereas the amplitude of E_x remains almost constant well beyond the L-cutoff, as the wave propagates towards the higher density. It agrees with the fact that EBWs have no high-density cutoff as described in Sec. 2.3. The position of the maximum of the E_x component can be identified as the turning point of the SX-wave close to the UHR, where the SX-wave turns into the EBW. For the higher temperatures, the turning point is shifted further towards the higher density in agreement with the ray-tracing simulations (see Ch. 6).

In the region between the UHR and the L-cutoff there exists a fast modulation of the field for cB_z and E_x components. This modulation is created by the interference between the SX-wave and the EBW. Indeed, the typical length of the oscillations in the pattern can be estimated as follows

$$|F_S \exp(ik_S x) + F_E \exp(ik_E x)|^2 \approx F_S^2 + F_E^2 + 2F_E F_S \cos(k_E x), \tag{5.32}$$

where terms F_S and F_E are the amplitudes of the SX-wave and EBW, respectively. It was assumed that the EBW wavevector k_E is much larger than the wavevector k_S of the SX-wave. Since both F_E and F_S change slowly over the EBW wavelength, it can

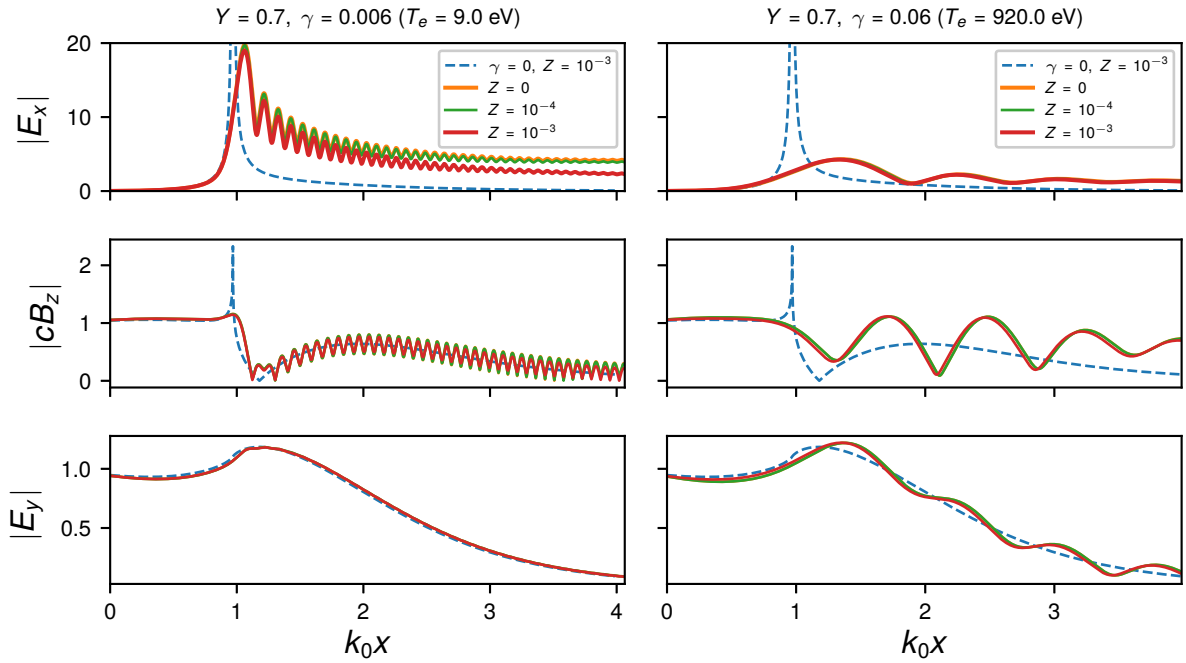

Figure 5.12: Fields of plasma waves in the plasma density profile with $k_0 L_{UHR} = 0.5$, in the magnetic field $Y = 0.7$. The left side corresponds to the low T_e case $\gamma = 0.006$, and the right side to $\gamma = 0.06$. The most interesting component is E_x, since it is the dominant component of EBWs. The simulations also show that EBWs have non-zero magnetic component cB_z. The cold plasma $\gamma = 0$ calculation (dashed line) is also shown for comparison.

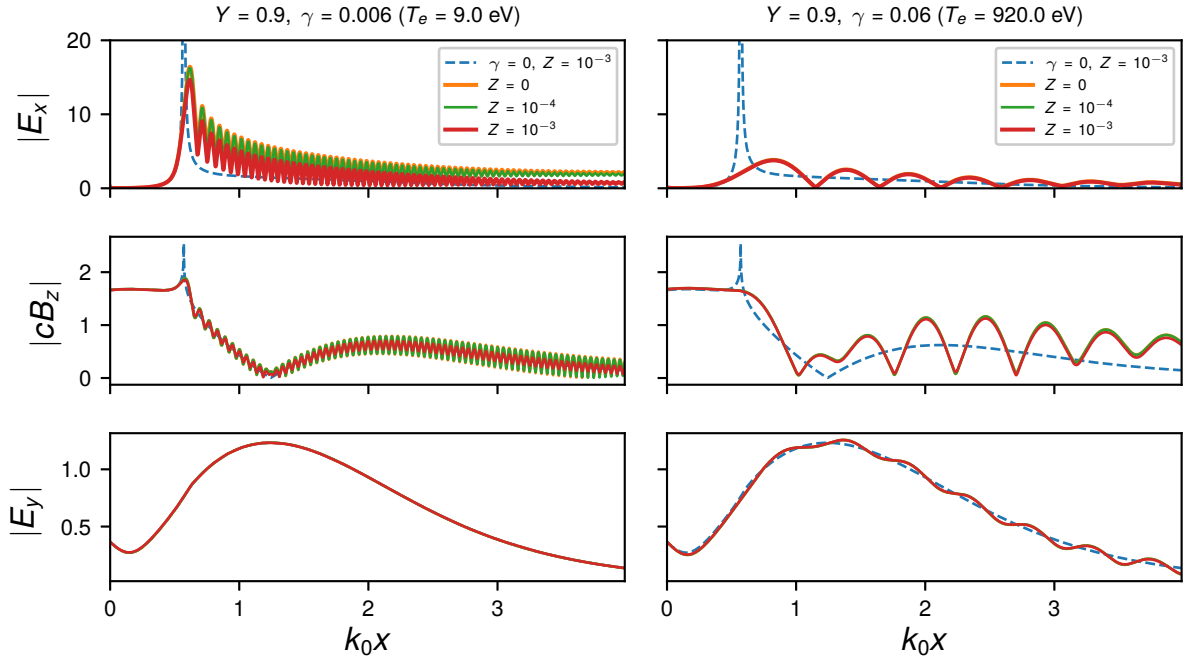

Figure 5.13: Fields of plasma waves in the plasma density profile with $k_0 L_{UHR} = 0.5$, in the magnetic field $Y = 0.9$. The left side corresponds to the low T_e case $\gamma = 0.006$, and the right side to $\gamma = 0.06$. In case of $Y = 0.9$, the EBW wavelength is shorter than for $Y = 0.7$, which can be clearly seen from the E_x component. The cold plasma $\gamma = 0$ calculation (dashed line) is also shown for comparison.

be concluded that the oscillation period is determined mostly by $\cos(k_E x)$. Thus, the typical oscillation length in the interference pattern equals to the EBW wavelength. As the magnetic field increases, the EBW wavelength decreases, which can be seen in Fig. 5.12 from the interference pattern between the EBWs and the SX-wave. The decrease of the EBW wavelength is consistent with the EBW dispersion relation since $Y = 0.9$ is closer to the magnetic field of the fundamental harmonic of the cyclotron resonance. When the spatial dispersion is included, the UHR will not be a singularity even in a collisionless plasma since the energy is effectively carried away from the UHR by the EBWs. This can be important for the consideration of the non-linear effects that arise when the electric field exceeds a particular threshold [42]. The inclusion of EBWs reduces the amplitude of the electric field at the UHR which can prevent possible non-linear effects.
In the case of the low electron temperatures, collisions appear to play a significant role only close to the UHR. The EBW group velocity is very small at the UHR, thus it is understandable that collisions may dissipate a significant part of the wave energy. For the higher temperatures, the wave appears to be insensitive to the collisions even at the UHR. For higher temperatures the wave propagates faster, thus, being less affected by the collisions. Hence, for the low temperatures, the dissipation processes at the UHR can significantly alter the EBW propagation.

Chapter 6

Phase-Space methods

6.1 Introduction

In the previous chapter, the full-wave simulations of EBWs were carried out only at the UHR vicinity. The main goal of this chapter is to investigate the EBW propagation further away from the UHR in the FLiPS plasma using the so-called phase-space methods. Applying these methods it is possible to investigate the EBW field in the bulk plasma, thus obtaining a complete theoretical description of the EBW propagation in the FLiPS plasma. The application of the phase-space methods will also help to understand further the plasma wave propagation.

Within the phase-space approach, waves are simultaneously described as a function of both coordinate $\vec{r}$ and wavevector $\vec{k}$ [12]. In general, such a description is not possible due to the uncertainty principle [81]. For instance, each point of a plane wave is characterized by $\vec{k}$. But a plane wave is infinitely extended in space, thus having no well-defined location.

The phase-space methods are a family of methods with the eikonal approximation described in Sec. 6.2 being the most widely used. The eikonal approximation or the geometrical optics (GO) approximation is valid, when the wavelength is small compared to the characteristic scales of the medium [11]. In this case, it is possible to approximately describe the wave simultaneously in terms of $\vec{r}$ and $\vec{k}$.

To understand the idea behind the eikonal method consider again a plane wave. A plane wave can exist only in a homogeneous medium. Indeed, a plane wave by definition has the same wavelength everywhere in space. However, when there is an inhomogeneity, the wavelength will vary depending on the medium properties. However, when the inhomogeneity is moderate, $\vec{k}$ will not change significantly over the length of many wavelengths. Thus, it is still approximately valid to assign to each point in space a wavevector $\vec{k}$, whose value can be found from the corresponding dispersion relation.

When $\vec{k}$ is known, it becomes possible to construct an approximate solution [11]. This approximation allows investigation of wave propagation when the full-wave methods are numerically too demanding. Solving the exact wave equation numerically in the case of a very small wavelength would be almost impossible as it requires either an extremely fine numerical grid to resolve the wavelength scale or a large numerical domain. Additionally, if such a simulation had been carried out, the wave effects such as the diffraction would have likely be negligible. In the eikonal approximation, the wave effects are neglected altogether and the primary goal is to find where and how fast the wave energy flows.

The rate at which the energy propagates is called the group velocity and defined as fol-

lows [20]

$$\vec{v}_g W = \vec{P}, \tag{6.1}$$

where W is the energy density of the wave and $\vec{P}$ is the Poynting vector defined by Eq. (A.1). Note that this definition is analogous to the definition of particle flux. Here $\vec{P}$ corresponds to the particle flux, W to the local particle density and $\vec{v}_g$ to their velocity. This similarity is not a coincidence and is due to the connection between the GO and classical mechanics [11]. Indeed, Hamilton established Eq. (6.6) that govern the ray propagation and showed that their dynamics is exactly the same as that of a particle with the momentum $\vec{p}$ in a force field.
The process of obtaining a ray-trajectory using the eikonal approximation is called ray-tracing. Ray-tracing is widely used in fusion plasma physics [82, 83], in space plasma physics [27], as well as in computer graphics to create highly realistic images [84]. In this thesis, the application of the ray-tracing is confined to the investigation of the SX-mode and EBWs since their expected wavelength fulfils the eikonal approximation in FLiPS plasma. Ray-tracing can be coupled with full-wave simulations to describe systems where the waves with very different scales and behaviours co-exist [85, 86].
After investigating the plasma waves using the standard ray-tracing approach, another phase-space method based on the so-called Wigner function [11] will be applied. This approach can be seen as an extension of the standard eikonal approximation and allows capturing wave effects such as the beam broadening due to the diffraction [61]. The method is based on the eikonal method, but instead of tracing only a single ray, a family of rays is traced. Each of the rays has a "weight" given by the Wigner function. A single ray propagation can be pictured as a point moving in the coordinate-wave vector 6D space, called the phase-space. Tracing a family of rays results in a cloud of points, similarly to an ensemble of particles that evolves as the rays propagate. One then can introduce the Wigner function [12] on the phase-space that represents the cloud density. Using the Wigner function, it then becomes possible to capture wave effects using the ray-tracing. The Wigner function can be applied to study wave propagation in turbulent plasmas of large fusion devices such as ITER [61, 87, 88, 89], where the full-wave methods are numerically too demanding.
Other methods to describe the full-wave effects also exist such as the beam-tracing method. The method can capture diffraction effects using the paraxial Wentzel-Kramers-Brillouin method [90]. Beam-tracing was, for example, implemented in the widely used code TORBEAM [91].

6.2 Standard Eikonal approximation

The main assumption of the eikonal approximation is that for a medium with slowly varying properties the solution locally looks like a plane wave. This fact is reflected in the ansatz solution $\phi(x) = A(x)e^{i\theta(x)/\epsilon}$, where ϵ is a small parameter. Then the amplitude and the phase are expanded into power series in ϵ

$$A(x) = \sum_{n=0}^{M} A_n \epsilon^n \tag{6.2}$$

$$\theta(x) = \sum_{n=0}^{M} \theta_n \epsilon^n \tag{6.3}$$

These power series are asymptotic, which means that the series are non-convergent for any non-zero ϵ and $M \to \infty$. However, an asymptotic series is a good approximation, when the series are truncated at some M [25]. Collecting the powers of ϵ will lead to the eikonal equation and the amplitude transfer equation [11, 50].
In order to illustrate the ideas of the eikonal method and problems that arise within its framework consider the 1D Helmholtz equation. Substituting this ansatz and collecting the powers of ϵ, the eikonal equation for the phase is obtained

$$\frac{d\theta}{dx} = k_0 N(x) \tag{6.4}$$

where $N(x)$ is the index of refraction. This equation belongs to the class of non-linear, partial differential equations. If the local wavevector is introduced as $k(x) = \frac{d\theta}{dx}$ then $k(x) - k_0 N(x) = 0$ can be interpreted as a local dispersion relation. It reflects the fact that the eikonal ansatz locally represents a plane wave. Introducing the function $D(x,k) = k - k_0 N(x)$ on the phase space, the solution of the eikonal equation are the points where $D(x,k) = 0$. Note that k is assumed to be independent of x. Hence, a ray is defined as a trajectory where $D(x,k) = 0$. If a ray is parametrized with the variable τ then the total derivative of $D(x,k)$ must be zero

$$\frac{dD}{d\tau} = \frac{\partial D}{\partial k}\frac{dk}{d\tau} + \frac{\partial D}{\partial x}\frac{dx}{d\tau} = 0 \tag{6.5}$$

It is easy to see that the total derivative vanishes when

$$\begin{cases} \dfrac{dx}{d\tau} = \dfrac{\partial D}{\partial k} \\ \dfrac{dk}{d\tau} = -\dfrac{\partial D}{\partial x} \end{cases} \tag{6.6}$$

Thus, the non-linear, partial differential equation can be replaced by an equivalent non-linear system of ordinary differential equations which is easier to solve. Equations (6.6) are the famous Hamilton's equations which are also found in the Hamiltonian formulation of classical mechanics.
Often the function $D(x,k)$ is referred to as the Hamiltonian. However, in the wave context it does not have the meaning of energy as in the mechanical context.
Considering the next order in the small parameter ϵ leads to:

$$\frac{\partial J(x)}{\partial t} + \nabla \cdot J(x) v_g = 0, \tag{6.7}$$

where v_g is the group velocity, t is time, and $J = A^2 \frac{\partial D}{\partial \omega}$. Equation (6.7) is the transport equation for the quantity J. Thus, first v_g is found from Hamilton's equations for a family of rays satisfying particular initial conditions and then the quantity J is found from the transport equation from which the amplitude can be calculated [11].
When $\frac{\partial J}{\partial t} = 0$, the product $J v_g$ will remain constant. Thus, when $v_g = 0$ the amplitude $A(x)$ becomes infinite, assuming that $\frac{\partial D}{\partial \omega} \neq 0$. Points where the amplitude blows up are called caustics and at these points the eikonal approximation breaks down. The theory of caustics is a rich topic that has received a lot of attention [92] and a detailed discussion is well-beyond the scope of this study. However, some general remarks that aid understanding of the eikonal methods can be made. Recall Liouville's theorem which

states that the phase-space density remains constant along the trajectories of the system. That is, there is a quantity $\rho(\vec{r}, \vec{k}; t)$ which satisfies the following continuity equation

$$\frac{d\rho}{dt} = \frac{\partial \rho}{\partial t} + \nabla_{\vec{r}} \cdot \frac{d\vec{r}}{dt}\rho + \nabla_{\vec{k}} \cdot \frac{d\vec{k}}{dt}\rho = 0 \tag{6.8}$$

Equation (6.8) shows that whenever there is focusing in the $x-$space there is de-focusing in the the $k-$space such that the phase-density remains constant. Thus, Eq. (6.7) may have infinite solutions because of the absence of a dependency on $\vec{k}$.
Thus, if the wave equation is first cast from the configuration space into the phase-space representation, then well-behaved solutions on the phase-space can be found using the eikonal method. Then solutions can be projected back onto the configuration space, with the projected solution being also well-behaved due to Liouville's theorem. In order to proceed with this approach, the concept of a distribution and the Wigner function will be introduced in Sec. 6.4.

6.3 Ray-Tracing in Plasmas

To gain understanding of plasma wave phenomena it is useful to start with the most basic non-trivial plasma model, namely a 2D plasma slab where the constant magnetic field is along the $z-$axis and the density gradient $\nabla n_e \parallel x$. The corresponding coordinate system is depicted in Fig. 6.1.

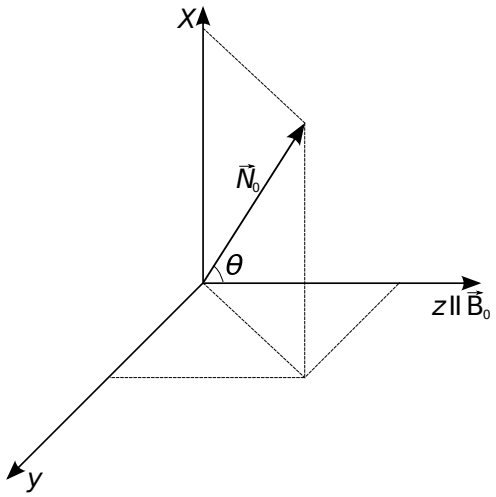

Figure 6.1: The geometry of the plasma slab model. The gradient of the normalised plasma density ∇X is along x-direction. In 2D ray-tracing simulations, the refractive index $\vec{N}$ is assumed to lie in the $x - z$ plane.

As the plasma properties do not vary in the z-direction the refractive index N_z will remain constant as seen from Hamilton's equations

$$\frac{dN_z}{dt} = c\frac{\partial D}{\partial z}/\omega\frac{\partial D}{\partial \omega} = 0 \tag{6.9}$$

Thus, the value of N_z is fixed by the antenna's structure. For the purpose of explanation of some features of the ray propagation, the cold plasma dispersion relation can be written in the following form:

$$A(X, Y)N_x^4 + B(N_z, X, Y)N_x^2 + C(N_z, X, Y) = 0, \tag{6.10}$$

where

$$A = S(X, Y), \tag{6.11}$$
$$B = (PS + RL) + (P + S)N_z^2, \tag{6.12}$$
$$C = PN_z^4 + PRL - (2PS)N_z^2 \tag{6.13}$$

with S, R, L and P given by Eqs. (2.13). The perpendicular refractive index can be found as follows

$$N_x^2 = \frac{-B \pm \sqrt{B^2 - 4AC}}{2A} \tag{6.14}$$

The solutions $N_{x,+}^2$ and $N_{x,-}^2$ correspond to the plus-minus sign in Eq. (6.14), and are

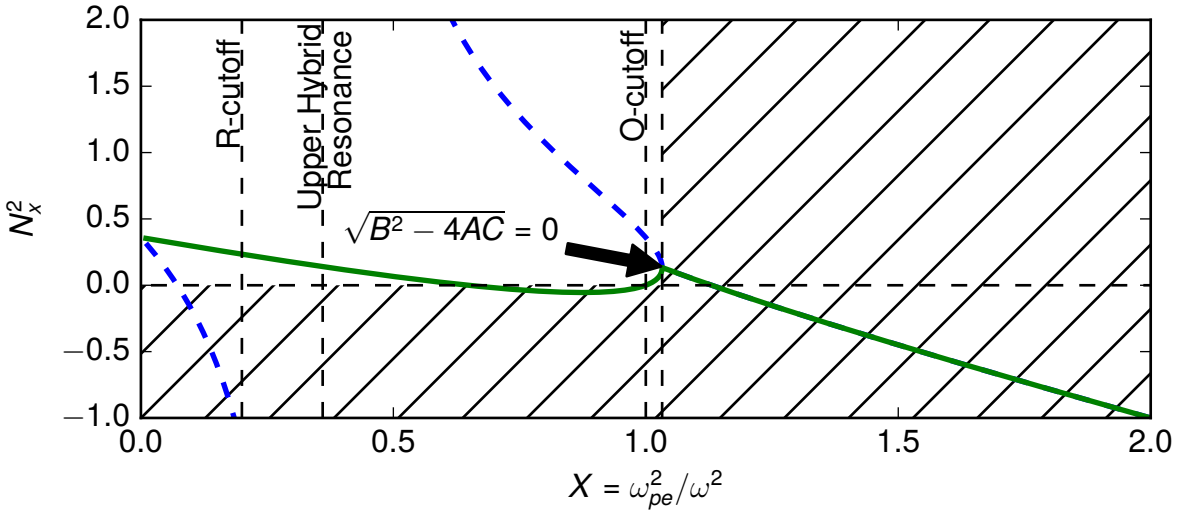

Figure 6.2: The solid and dashed lines correspond to $N_{+,x}^2$, $N_{-,x}^2$ modes (eigenvalues), respectively. The magnetic field is $Y = 0.8$, and the parallel refractive index is $N_z = 0.8$. In the hatched area, there are no propagating solutions, since N_x^2 has an imaginary part. Thus, in the hatched area, both eigenvalues are complex conjugated, and their real parts are equal. The arrow indicates the point, where both eigenvalues start to coincide.

plotted in Fig. 6.2 for an oblique angle with respect to the background magnetic field. The propagating plasma waves exist only for $N_x^2 > 0$. When $B^2 - 4AC \leqslant 0$, $Re(N_{+,x}^2) = Re(N_{-,x}^2)$ and $Im(N_{+,x}^2) = -Im(N_{-,x}^2)$.
Figure 6.3 shows results of ray-tracing in the cold plasma slab immersed in the magnetic field with $Y = 0.8$. The arrows show $\vec{k}/|\vec{k}|$, and as a consequence of the anisotropy are not in general parallel to the group velocity. The distance between the arrows along the ray is given by $\vec{v}_g \Delta t$, where Δt is a constant time interval. In the vicinity of the UHR, the distance between the arrows is small because $\vec{v}_g$ decreases, which is one of the main characteristic of a resonance.
An interesting feature of the O-mode propagation is a cusp at the O-cutoff. The cusp can be explained based on Eq. (6.14). At the O-cutoff vicinity C is small thus the square root in Eq. (6.14) can be expanded, resulting in the following expression

$$N_{+,x}^2 \approx \frac{-B + B(1 - \frac{2AC}{B^2})}{2A} = -\frac{C}{B} \tag{6.15}$$

The ratio of the components of the group velocity at the O-cutoff vicinity can be written as

$$\frac{v_{g,z}}{v_{g,x}} = \frac{\partial D/\partial N_z}{\partial D/\partial N_x}\Big|_{D=0} = \frac{1}{2N_{+,x}} \frac{\partial N_{+,x}^2}{\partial N_{+,z}} \tag{6.16}$$

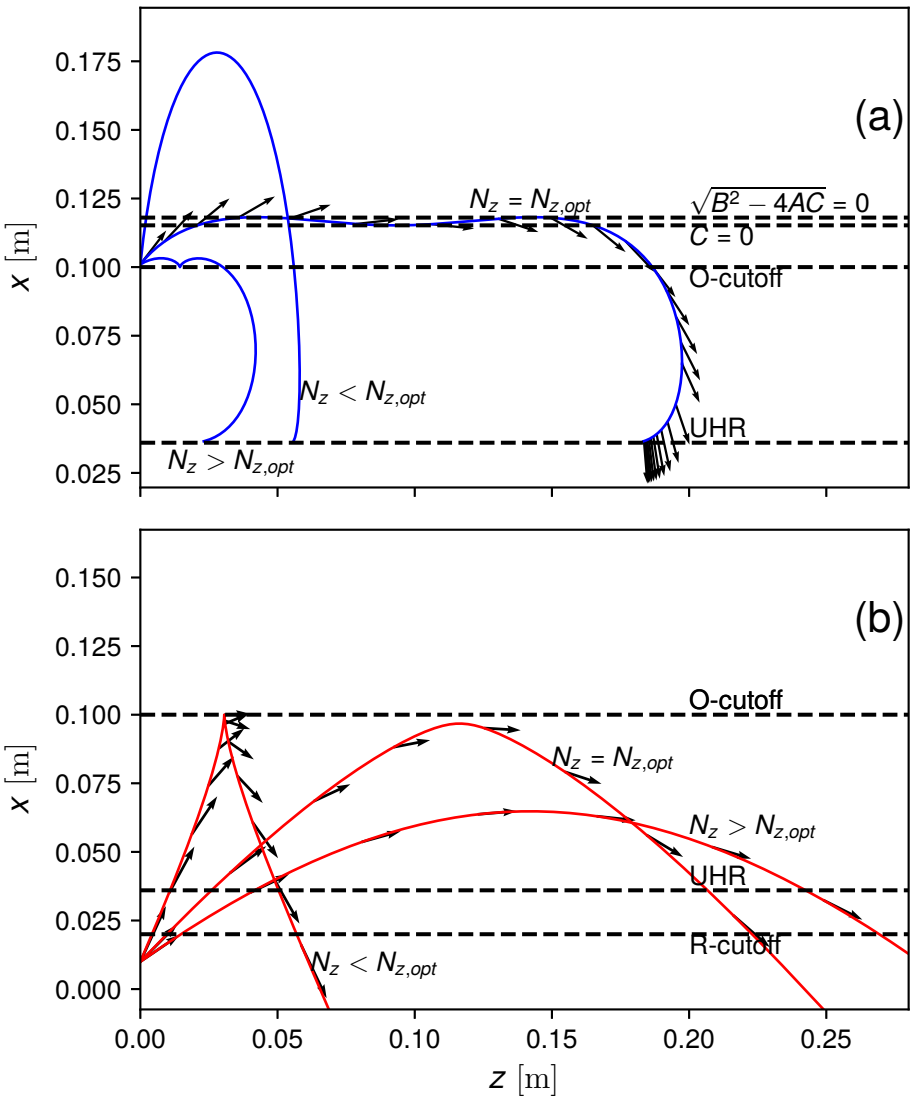

Figure 6.3: Ray-tracing of O- and X-modes in a cold plasma slab. (a) shows the ray-tracing of X-mode and (b) shows the ray-tracing of O-mode. With the increasing angle of incidence, the O-mode reflects before the O-cutoff. The O-mode passes through the UHR and R-cutoff without being affected. As the SX-mode approaches the UHR, $\vec{v}_g$ becomes predominantly parallel to $\vec{B}_0$ due to the presence of the UHR. For $N_z < N_{z,opt}$ the SX-mode is guided along the z-direction in the narrow region close to the O-cutoff. The guiding becomes significant in the case of the suffciently large angle between $\vec{B}_0$ and ∇n_e [93].

Substituting $N^2_{+,x}$ from Eq.(6.15) into the previous equation and treating P as a small parameter

$$\frac{v_{g,z}}{v_{g,x}} \sim \frac{1-X}{\sqrt{1-X}} \to 0, \tag{6.17}$$

which explains the cusp.

Another interesting aspect is guiding of the SX-mode along the $\vec{B}_0$, which is seen in Fig. 6.3. The wave suffers three consecutive reflections before starting to propagate towards the UHR. The behaviour can be explained based on Fig. 6.2. As shown in Fig. 6.2, the ray has two turning points. One of them corresponds to the point where $N^2_{+,x}$ and $N^2_{-,x}$ coincide which is marked with an arrow. Interestingly, at this turning point $N_x \neq 0$. The second turning point is where $C = 0$. The ray behaviour in cold magnetised stratified plasmas is discussed, in detail, in [94].

6.3.1 Hot Plasma Ray-Tracing

Up to now, the waves were investigated in a cold plasma. In the following, the SX-mode and EBW propagation will studied in a hot non-relativistic magnetised plasma. One of the implemented ray-tracing codes within the course of the thesis is named RiP (Rays in Plasma). The code is based on the full hot non-relativistic plasma dielectric tensor [20, 95]. It is possible to include the relativistic effects by using the relativistic dispersion relation for the EBWs [96]. However, the relativistic effects are estimated to play a significant role only for $T_e > 1$ keV [97, 98]. The RiP code is capable of tracing all possible high frequency[1] plasma modes for arbitrary electron temperatures, magnetic and density profiles. The code is based on [99], where the EBW propagation was investigated in a tokamak plasma. The dispersion relation that is used for the ray-tracing is defined in the system of coordinates where $z \parallel \vec{B_0}$ and the wavevector $\vec{k}$ lies in the x-z plane, whereas the magnetic field and density profiles are defined in the laboratory system of coordinates. All the following results of the ray-tracing are depicted in the laboratory system of coordinates. Thus, the code must perform transformation between these two system of coordinates as described in Appendix B.1.
As a basic test of the code validity, the ray-tracing of O- and FX-mode was performed with the RiP code and the results were compared with the predictions obtained within the cold plasma approximation. As expected, their propagation was practically unaffected by T_e in FLiPS plasma, where $T_e \approx 10$ eV. The T_e is expected to play a significant role only when the phase velocity of a wave is comparable to the thermal motion of the electrons [20]. This occurs for the slow branch of the X-mode (SX-mode) near the UHR. As discussed in the previous chapters, the UHR is not a "true" resonance, as predicted by the cold plasma theory, but the point, where the SX-mode becomes quasi-electrostatic and turns into the EBW.
In the following section, the trajectories of the SX-mode are investigated with the RiP code for different plasma and magnetic field geometries in the slab model, with the aim to identify the most important plasma parameters that influence the EBW propagation. For the slab model, the ray-tracing simulations are performed for two distinct magnetic field ranges, which correspond to the fundamental and the first cyclotron harmonics [2].
Then, the ray-tracing simulations for the FLiPS relevant plasma geometry is presented. To increase the numerical precision of the calculations, a simplified geometry of the background magnetic field is used. Only the B_z component is included, whereas the radial magnetic field component B_r is neglected since $B_z \gg B_r$. Indeed, for the experimentally relevant magnetic field configurations, the magnetic field lines are almost parallel to FLiPS axis. To further simplify the magnetic field model, the dependency of $B(z, r)$ on the radial coordinate r is also neglected. Within this approximation, the magnetic field is given by a simple function, whose derivatives can be found analytically. Note that this magnetic field is not divergence-free, which is not physical. However, the magnetic field enters into the simulations only as a background plasma parameter, and is not required to be divergence-free.

[1] High frequency means that the ion motion can be neglected

[2] A harmonic number is an integer that characterises the magnetic field strength. The $n-$harmonic is defined as $\frac{1}{n+2} < Y < \frac{1}{n+1}$. The harmonic with $n = 0$ is usually called the fundamental harmonic and EBWs are strongly damped at the values of $Y = \frac{1}{n}$. EBWs cannot propagate to a region with a different harmonic number without being absorbed since the wave would have to pass through the cyclotron resonance.

6.3.2 Ray-Tracing in a Hot Plasma Slab

In the following, the propagation of the SX-mode and its transformation into the EBWs will be investigated with the RiP code. The SX-mode is created by the incoming electromagnetic radiation through the conversion (O-SX) or tunnelling (FX-SX). When the ray-tracing of the SX-mode is shown, the SX-mode is assumed to be created by either incoming O- or FX-mode. The ray-tracing of the waves involved in the O-SX conversion can be directly compared to the full-wave simulations since the involved waves fulfil the eikonal approximation with the exception of the conversion region. Within the ray-tracing approach, it is impossible to investigate the conversion processes self-consistently, however, outside of the conversion region each of the waves involved in the process can be well described by the ray-tracing.
An example of O-X-B conversion simulated with the ray-tracing is demonstrated in Fig. 6.4 shown together with the corresponding cold plasma full-wave simulation. In

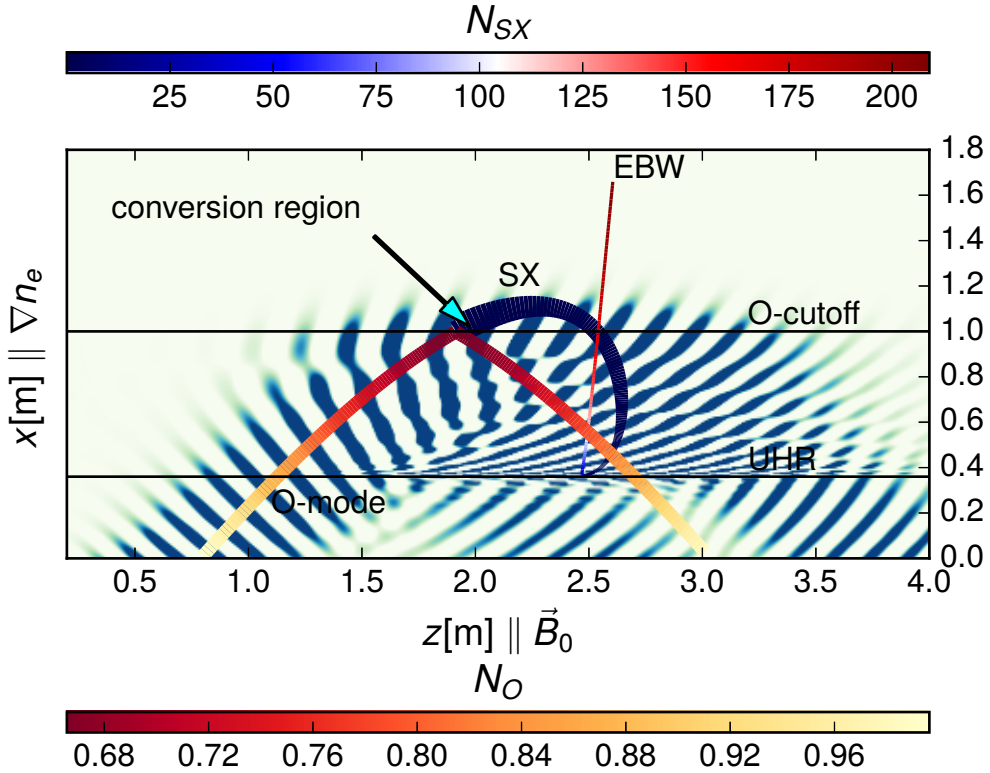

Figure 6.4: A comparison of the ray-tracing calculations with the corresponding FDTD simulation of the O-X-B conversion for the optimal launching angle. The comparison shows that the ray-tracing is a simplified description of the wave propagation. In the ray-tracing waves are replaced by the ray-trajectories which are the trajectories along which the wave energy propagates. Each point of the trajectories is characterised by the group velocity $\vec{v}_g$ and the refractive index $\vec{N}$. In the figure the magnitude of $\vec{v}_g$ is represented by the line thickness of the trajectories and the magnitude of $\vec{N}$ is shown by the colorbars. The SX-mode $\vec{v}_g$ decreases as the wave approaches the UHR and the $\vec{N}$ increases.
The coupling of the O-mode with the SX-mode cannot be simulated within the eikonal approach. Therefore, the outgoing O-mode in the ray-tracing simulations is unaffected by the plasma. Whereas, the FDTD simulation shows that the intensity of the outgoing O-mode at the beam center is reduced due to the strong O-SX coupling. See Fig. 2.8 for the comments on the effects of the beam divergence on the conversion efficiency. The SX-mode ray was initialised close to the O-cutoff, where the strongest coupling between the O-cutoff and the SX-mode is expected based on the full-wave analysis. Since the FDTD simulations were performed in a cold plasma, the SX-mode is completely absorbed by the collisional damping at the UHR. In the presented ray-tracing simulation, the SX-mode ray turns into an EBW ray, which then propagates towards the higher plasma density.

the full-wave simulation, the direction of the incoming O-wave corresponds to that obtained with the ray-tracing. When the coupling between the O- and SX-mode is strong, which happens around the optimal injection angle, a significant part of the O-mode is

transformed into the SX-mode. Thus, in the full-wave simulation, the central part of the outgoing O-mode beam is strongly reduced unlike in the ray-tracing simulations, where the reflected O-mode seems to be unaffected by the plasma. As seen from the full-wave simulations, the outgoing O-mode beam has pronounced side lobes which appear due to the finite k-spectrum of the O-beam as described in Sec. 2.3.1.
Unlike the O-X-B conversion, the FX-SX tunnelling cannot be calculated using the ray-tracing method since the incoming FX-mode wavelength is much larger than the typical density inhomogeneity scale. But the SX-mode and the EBW propagation can be studied with the ray-tracing since their wavelengths fulfil the eikonal approximation.
In the following ray-tracing simulations, only the SX-mode will be shown and the O-mode and FX-mode will be omitted for clarity. As noted before, the initial N_z is fixed by the antenna. Thus, the initial N_x must be chosen such that the hot dispersion relation is satisfied, namely $D(x, z, N_x, N_z) = 0$ at the starting point (see Sec. 6.2). This condition can be seen as an equation for N_x, since N_z and the plasma parameters are fixed at the starting position. The equation can be solved only numerically due to the complexity of D. A root searching routine from the scipy open source package was used, with the initial guess for N_x found from the cold dispersion relation. With these measures, the residue of the hot dispersion relation D was less than 10^{-12} at the starting point.
Ideally, a dispersion relation D should be zero along the rays. The accumulation of the numerical and round-off errors unavoidably causes a gradual increase of D, and eventually, the simulations become unphysical, which results, for instance, in $v_g > c$. The situation is analogous to the energy drift over time in the simulations of mechanical systems. The energy drift becomes especially pronounced for the EBWs when values of the refractive index $N \gg 1$. As described in Appendix B.2, by modifying the hot dispersion relation it is possible to reduce the dispersion relation drift and avoid possibly unphysical results. The unphysical results can be also caused by floating-point arithmetic. For instance, for small N_z, the derivatives of the plasma dispersion function require a careful treatment as described in Appendix B.3.
Figure 6.5 shows the rays of the SX-mode initiated close to the O-cutoff for different magnetic field strengths that correspond to the fundamental harmonic.

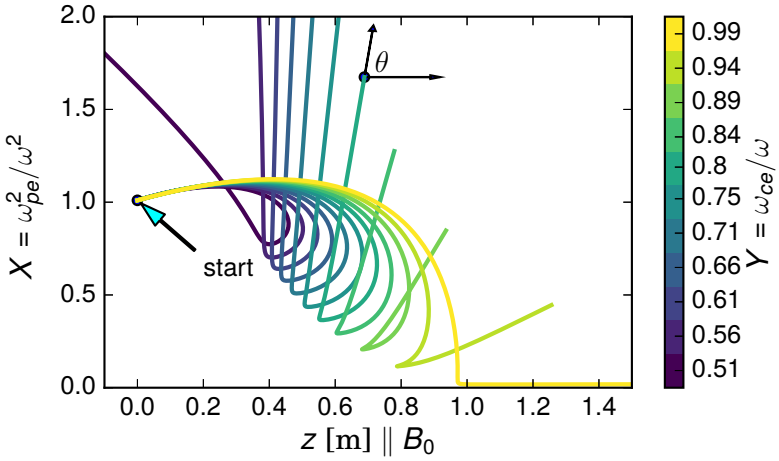

Figure 6.5: Ray-tracing of the SX-mode at the fundamental harmonic. Each ray is traced in the constant magnetic field Y, shown by the colorbar. The initial $N_z = N_{z,opt}$ corresponds to the O-X conversion. The subsequent EBW rays change its direction depending on Y. The angle θ is the angle between EBWs $\vec{v}_g$ and the background magnetic field.

These rays are assumed to be created by the incoming O-wave at the optimal injection angle. Each ray was traced in the plasma with a different constant background magnetic

field in order to investigate the effects of the magnetic field of the SX-mode rays. At each magnetic field the rays have two turning points. The upper turning point is caused by the reflection from the dense plasma and is also present in the ray-tracing in the cold plasma (see Fig. 6.3). The lower turning point is in the UHR vicinity and its position depends on Y. In accordance with $X_{UHR} = 1 - Y^2$, the UHR is at the higher plasma density for the lower magnetic fields. As the EBW rays keep propagating into the overdense plasma, their direction of propagation does not change significantly. It allows introduction of the angle θ defined as the angle between the EBW $\vec{v}_g$ and $\vec{B}_0$. This angle spans the whole range from 180° to 0°, as the magnetic field changes from $Y = 0.5$ to $Y = 1$. At the ends of the Y range, $\vec{v}_g$ of the EBWs is predominantly along the magnetic field. Figure 6.6 shows how the EBW propagation direction depends on the magnetic field for different N_z. The negative angles correspond to the rays with $v_{g,\parallel} < 0$, which means that the rays

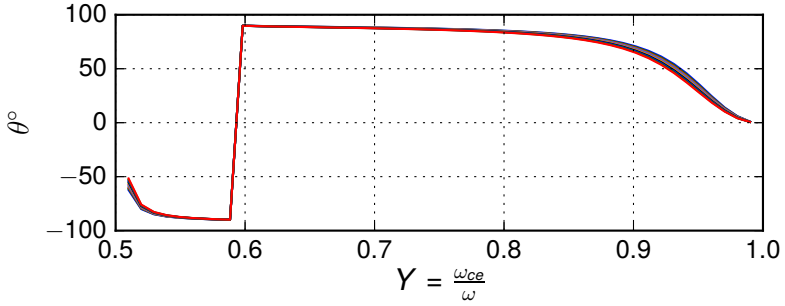

Figure 6.6: Dependency of angle θ on the magnetic field strength Y. The simulations were performed for 50 magnetic field values within the rage $0.51 < Y < 0.99$ and plasma with $T_e = 10$ eV. For each magnetic field from the range, 10 rays were initiated with different N_z, around the optimal $N_{z,opt} \pm 0.1$. The figure shows that the EBW rays are only weakly affected by the initial choice of N_z. The function $\theta(Y)$ has a discontinuity at $Y \approx 0.6$. At this magnetic field the EBW rays propagate exactly across the magnetic field.

propagate in the opposite direction to the magnetic field. At $Y = 0.6$, the EBW rays propagate exactly across the background magnetic field. The figure shows that θ is a weak function of N_z. It can be concluded that the EBW propagation in the overdense plasma is mostly determined by the background magnetic field.

An example of SX-mode rays that would be created in the FX-SX tunnelling is shown in Fig. 6.7. The rays were initiated with a small $N_z < 0.1$, which means that the SX-mode propagates predominantly perpendicular to the magnetic field. Such SX-mode rays would be created in the direct tunnelling by an incoming FX-mode. The SX-mode penetrates further inside the plasma before being reflected at the L-cutoff. But the subsequent EBW rays behave similarly to the case described above, where the SX-mode rays were initiated with $N_{z,opt}$ at the O-cutoff vicinity. This further confirms that the initial choice of the refractive index or of the coupling scheme has a weak effect on the EBW propagation in low temperature plasmas.

Figure 6.8 shows the rays for the magnetic fields in the range $\frac{1}{3} < Y < \frac{1}{2}$, which corresponds to the first harmonic. The EBW parallel group velocity again changes its direction as a function of Y. The main difference between the first harmonic and the fundamental harmonic EBW is that the wave propagates further towards the low-density plasma before turning back. The turning point can be found from the analysis of the EBW dispersion relation as presented in [20] and is explained by the bell like shapes of the EBW dispersion curves at higher harmonics as shown in Fig. 2.5. Thus, the higher harmonics EBW are more susceptible to the edge plasma turbulence and can be collisionally damped in the edge region. Indeed, the FLiPS edge plasma is turbulent as was shown in Sec. 3, and has low T_e, which causes a significant collisional damping. Thus, the fundamental harmonic

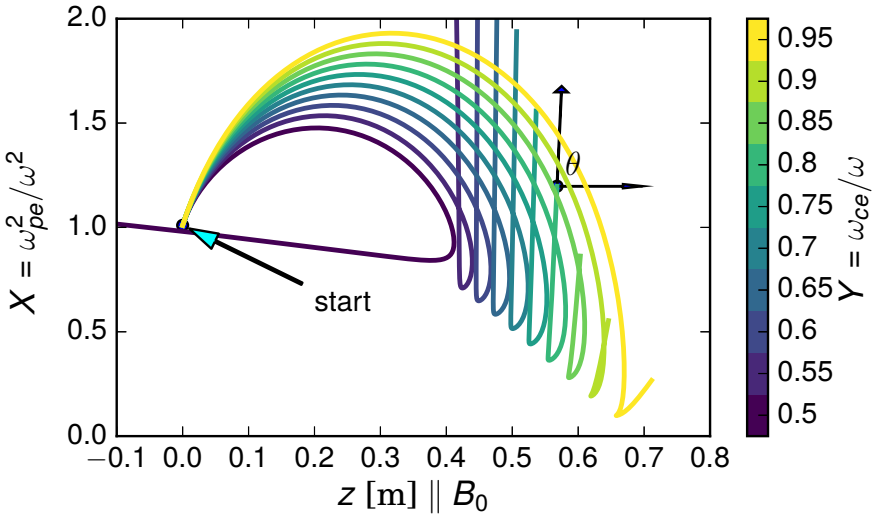

Figure 6.7: The same as Fig. 6.5, but with the SX-mode rays initiated with small N_z. This initial N_z corresponds to the direct FX-SX-EBW coupling since the FX-SX coupling is the most efficient for near perpendicular injection as shown in Fig. 5.8.

EBWs are of a greater practical interest in the FLiPS experiments, because the EBWs do not propagate as far to the plasma edge as in the case of the higher cyclotron harmonics. From the discussion above it can be conclude that the magnetic field has the strongest influence on the EBW propagation. The ray-tracing can be extended to arbitrary geometries that satisfy the eikonal approximation. Therefore, as the next step the SX-mode and EBW propagation will be investigated in the FLiPS relevant geometry.

6.3.3 Ray-Tracing in FLiPS Plasma Geometry

The ray-tracing of SX-mode will be carried out in the FLiPS mid-horizontal plane. In the mid-horizontal plane there is an inhomogeneity in the radial direction caused by the density gradient ∇n_e, and in the axial z-direction caused by the axial magnetic field gradient ∇B_z. The axial density gradient was not measured experimentally as it would require a long supporting structure for the Langmuir probe inside the plasma that would disturb the plasma. However, it is expected that the plasma density stays relatively constant along the magnetic field lines due to the high mobility of the charged particles along the field lines. Such a density model was also used in [94], where the ray-tracing of plasma waves was performed in a magnetic mirror configuration. As it will be shown, taking into account the axial density gradient in weakly overdense plasmas is important for correct simulations of the O-X-EBW coupling scheme. Here, the weakly overdense plasmas are understood as plasmas with the densities significantly below the L-cutoff. In this case, as it is well known [27, 32], the X-EBW coupling efficiency is max. 25% since the intrinsic RL-resonator is absent (see discussion in Sec. 4.4). When the plasma is weakly overdense, the O-X-EBW conversion will be also affected since the SX-mode rays must have a sufficiently large parallel refractive index $N_\parallel$ to reflect towards the UHR where they turn into EBWs. Indeed, the position of the SX-mode cutoff depends on $N_\parallel$, and for the larger $N_\parallel$ the SX-mode reflects at the lower plasma densities. Previously, the O-X conversion in weakly overdense plasmas has not been discussed in the literature on the O-X-B conversion. To investigate the effect of the density profile on the waves, the ray-tracing simulations were performed for two profiles. One of the profiles is the experimentally measured density profile shown in Fig. 3.7 with the steep edge density gradient. This profile is difficult

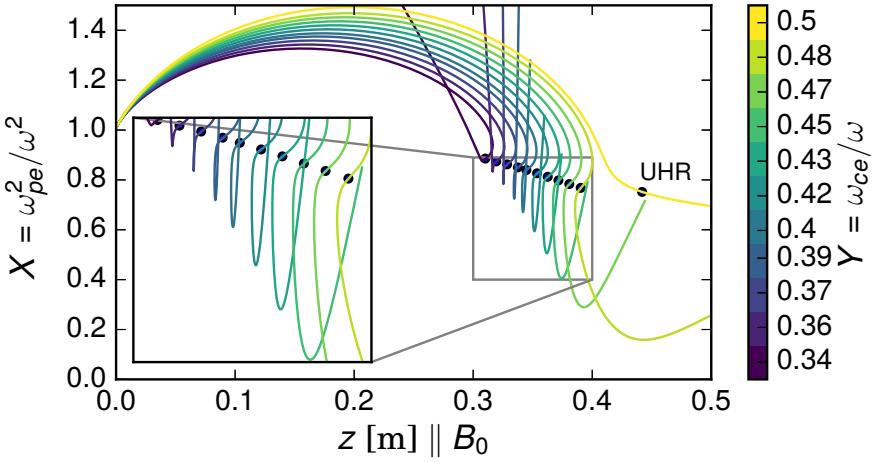

Figure 6.8: The ray-tracing of the first harmonic EBW for different magnetic fields in the range $0.333 < Y < 0.5$. At the UHR the SX-mode becomes the EBW as in the case of the fundamental harmonic. Unlike the fundamental harmonic (Fig. 6.7), the UHR is not a turning point in this case. After passing the UHR resonance, the wave propagates further towards the plasma edge. This behaviour can be understood from dispersion curves in Fig. 2.5 and their bell-like shape. The $\vec{v}_{g,\parallel}$ depends on the magnetic field similarly to the fundamental harmonic. As $Y \to 0.5$ the EBW rays propagate predominantly along the magnetic field.

to use in the ray-tracing simulations due to its steep density gradient at the edge where the eikonal approximation can be violated, which also leads to the numerical problems. To study the EBW rays in the case of the measured density profile, the EBW rays can be initiated directly at the UHR vicinity. This approach will be used in Sec. 6.4 where EBW rays are traced with an electrostatic code. The other n_e profile having a bell curve was used to investigate SX-mode propagation is sufficiently overdense that the L-cutoff is inside the plasma. Thus, the injected SX-mode rays will eventually reflect at the L-cutoff and turn into EBW at the UHR.

The ray-tracing in a plasma with the L-cutoff is shown Fig. 6.9. The EBW ray trajectories are not straight as in the plasma slab (Fig. 6.5) since now there is the axial magnetic field gradient, which creates the axial inhomogeneity that affects the rays. The EBW rays do not propagate indefinitely in the z-direction, instead, they are bouncing back-and-forth, which leads to the foci formation. Thus, the plasma acts as a waveguide or a wavechannel on the EBWs, restricting the wave propagation in the z-direction. The wavechannel phenomenon arises for different types of waves, not only in plasmas but also in the field of acoustics [100] where the properties of the underwater wavechannel were investigated using the ray-tracing as well. The intensity of a wave, propagating in a wavechannel decreases much less than in the case of free-space propagation since the beam divergence is limited by the wavechannel. Thus, the waves that propagate in a waveguide are easier to measure experimentally.

To further examine the EBW trajectories inside the wavechannel, another code was developed, based on the electrostatic dispersion relation. A similar approach was used in [101], where EBW trajectories in a plasma within inhomogeneous magnetic field were also studied using a ray-tracing code based on the electrostatic EBW dispersion relation. The main advantage of this approach is the speed-up of the simulation and increase of the numerical precision. The disadvantage is that the SX-mode is not included in the simulations. The second code will be applied in Sec. 6.5 to investigate the EBW focusing in the FLiPS plasma.

The SX-mode created in the O-X-B conversion can be investigated, using the ray-tracing method. Figure 6.10 shows a bundle of SX-mode rays initiated close to the O-cutoff. The

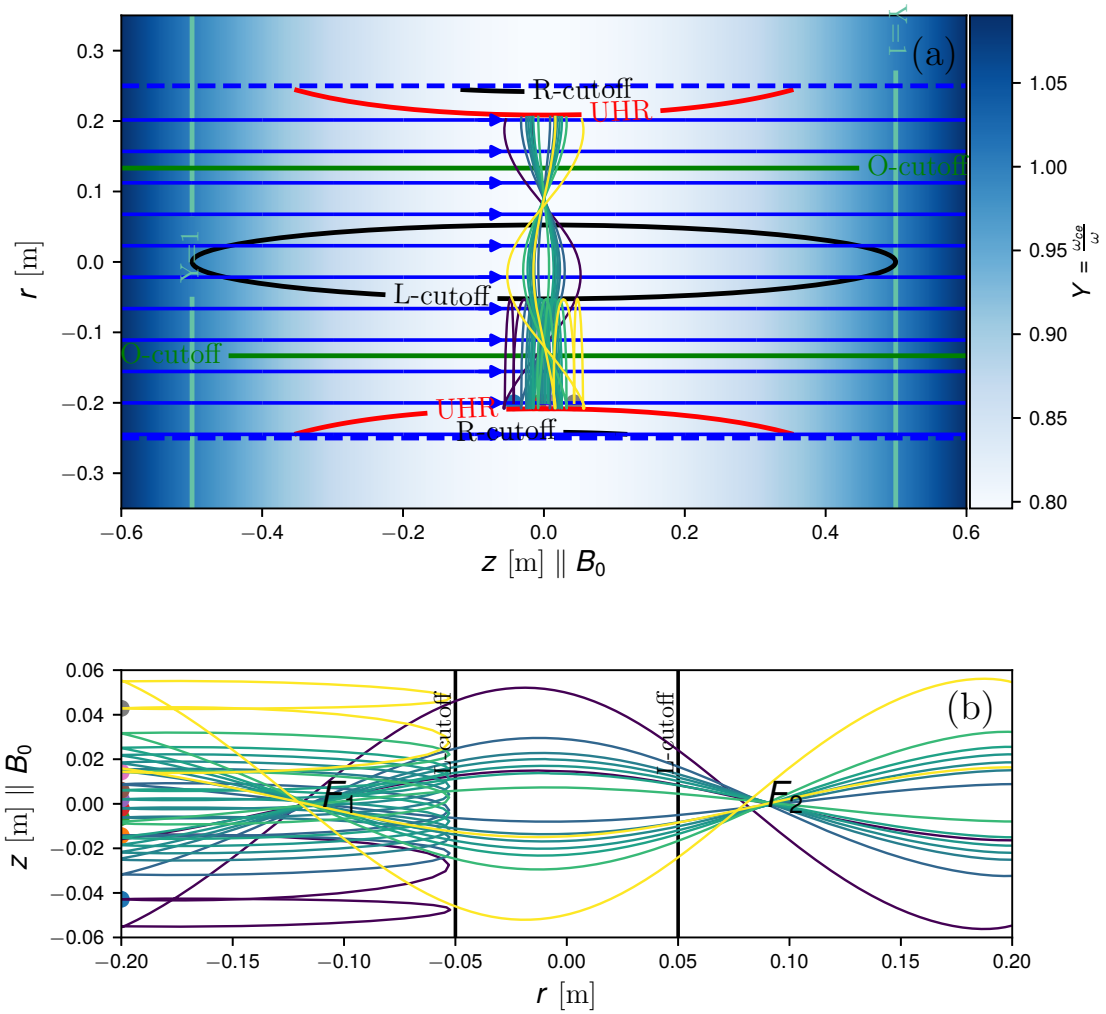

Figure 6.9: a): Ray-tracing simulations of the SX-mode in the FLiPS magnetic field geometry. The L-cutoff is in the plasma since the plasma density was chosen to be sufficiently high. The SX-mode antenna plane is placed slightly above the UHR. The antenna radiates SX-mode and is aligned with $\vec{B}_0$. This corresponds to the direct SX-EBW coupling scheme. At each point on the antenna, two SX-mode rays propagating predominantly in the radial direction were initiated with $N_{\parallel} = \pm 0.03$. b) shows the detailed view of the rays. In the region $-0.2 < x < -0.05$ the SX-mode co-exists with the EBWs, which causes the interference pattern in the full-wave simulations shown in Fig. 5.12. The SX-mode rays propagate toward the L-cutoff, where they are reflected towards the UHR. The subsequent EBW rays clearly form two foci F_1 and F_2. In these foci a higher EBW intensity is expected.

bundle approximately describes SX-mode into which the incoming O-mode is converted at the O-cutoff. The initial parallel refractive index is $N_{\parallel} = N_{\parallel,opt}$ at each initial z-position, thus the incoming O-mode would be completely converted to the SX-mode in the corresponding full-wave simulations. As in the previous case of the propagation perpendicular to the magnetic field, the EBW trajectory has the characteristic bouncing back-and-forth along the z-direction. It is also in agreement with the results from previous section, where it was shown that also in the slab model, the initial choice of the refractive index does not significantly affect the subsequent EBW trajectories. The behaviour of the refractive indices of the rays in Fig. 6.10 is shown in Fig. 6.11. The initial SX-mode refractive index increases at the UHR, where the SX-mode becomes the EBW. The EBW perpendicular refractive index $N_{\perp}$ reaches its maximum at the plasma center, where the density has its maximum.

The parallel refractive index $N_{\parallel}$ changes its sign periodically, which is in agreement with Fig. 6.10, where EBW $\vec{v}_{g,\parallel}$ changes periodically its direction. Such a periodic change of

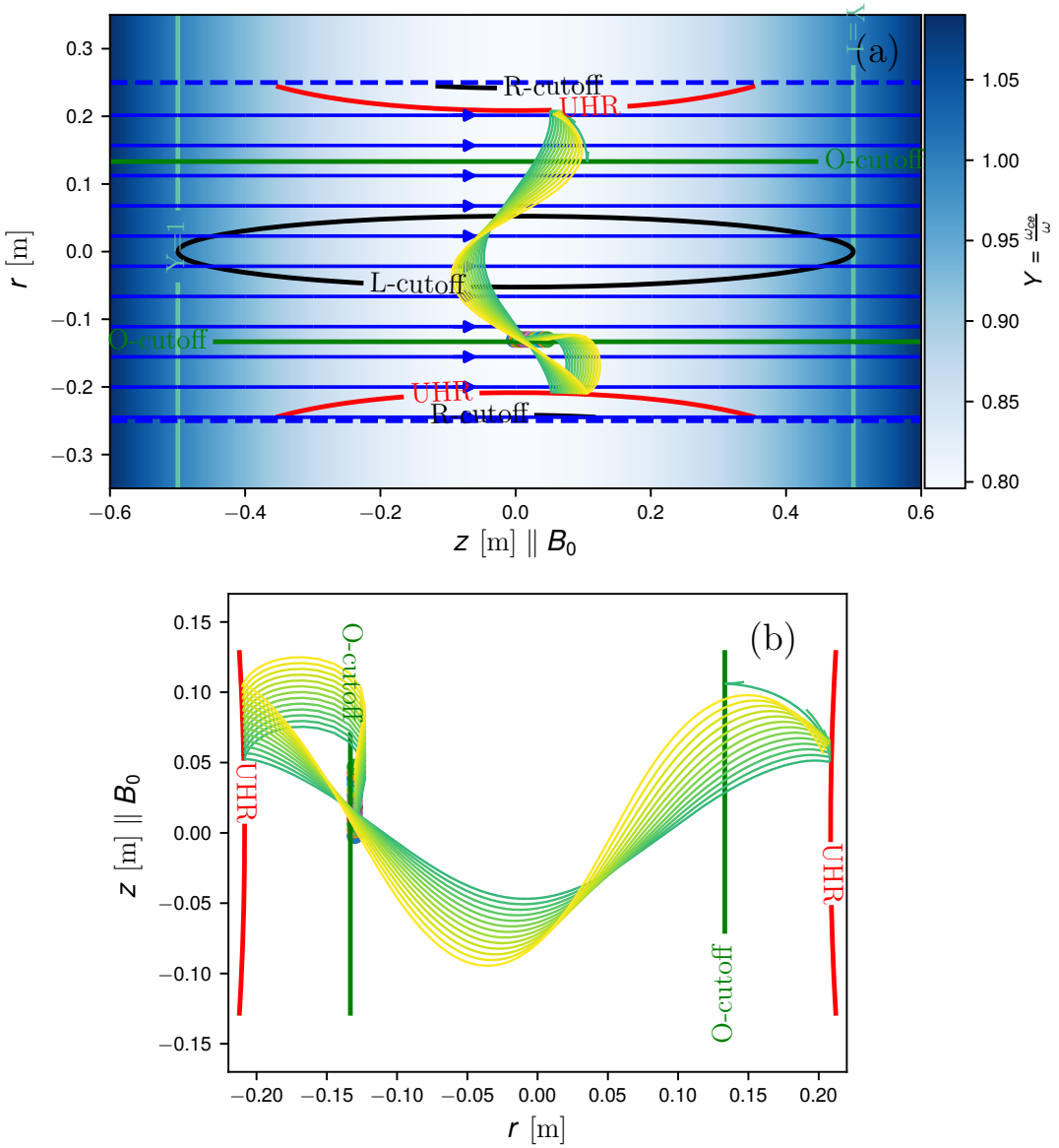

Figure 6.10: a): A bundle of SX-mode rays initiated at the O-cutoff at θ_{opt} in the FLiPS plasma with $T_e = 10$ eV. b) is the detailed view of the rays. The rays were launched at the optimal angle in the magnetic field with the axial gradient along z-axis. The gradient creates a plasma wavechannel within which the EBW rays are guided.

$N_\parallel$ was also reported for Ion Bernstein Waves[3] in [102, 103] in toroidal plasmas, where rapid oscillations of $N_\parallel$ were studied. This effect is important for understanding the effect of Landau damping on the EBWs and IBWs. Indeed, when $N_\parallel$ is large, the waves can be strongly Landau damped. However, the Landau damping should not be significant in the FLiPS plasma due to low T_e as discussed in Ch. 3.

As the EBWs reach the UHR on the opposite side ($r \approx 0.2$ m) the wave turns back into the SX-mode and $N_\perp$ decreases. There the wave will be partially damped by collisions or decayed through the parametric decay. The remaining energy of the SX-mode can tunnel outside as the FX-mode. It can be concluded that both O-X-B and direct X-B coupling scheme produce EBWs, which can be trapped in the plasma wavechannel.

Now the propagation of SX-mode will be investigated in the FLiPS experimentally measured profile shown in Fig. 3.7. The FLiPS plasma was normally not strongly overdense

[3]IBW physics is almost identical to the EBW physics. Thus, many results of IBWs can be directly applied to EBWs.

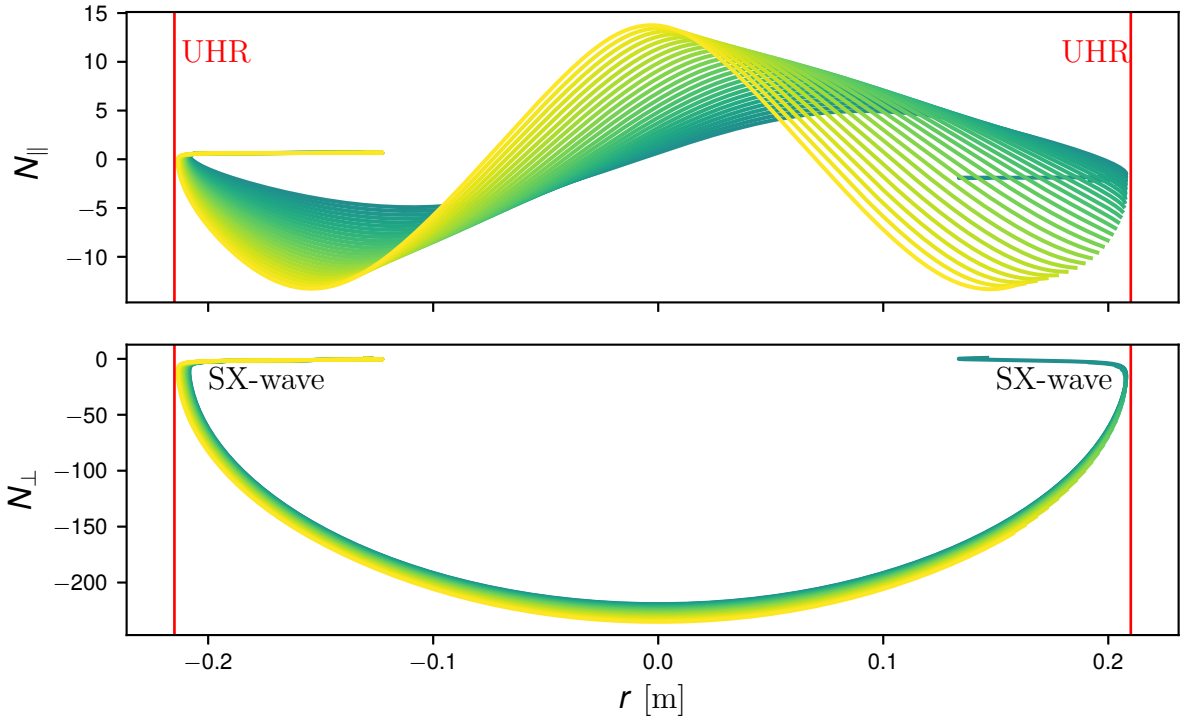

Figure 6.11: Behaviour of the refractive indices of the SX-mode rays shown in Fig. 6.10. $N_\parallel$ and $N_\perp$ refractive indices significantly increase when the rays reach the UHR, where the SX-mode becomes an EBW. When the rays reach the other UHR at $x_0 \approx 0.2$m the refractive indices decrease again, meaning that the wave turns back into SX-mode. In reality, the collisional damping, parametric decay and coupling to the FX-wave will be also significant.

with the peak density $X = 1.1$ at the plasma center, which means that the L-cutoff was not present in the plasma. The SX-mode will traverse the plasma in the radial direction and then be absorbed at the UHR on the opposite side, as discussed in Ch. 4.
In the case of the O-X coupling, the SX-mode propagates at a sufficiently large angle to the magnetic field which means that even without the L-cutoff the SX-mode can be reflected from the dense plasma. In this case, the ray behaviour is somewhat more complicated and will be analysed in the following. The main idea is that the turning point, which is the confluence point of the eigenvalues $N_{+,\perp}$ and $N_{-,\perp}$ that describe the SX-mode, can be absent from the plasma at the FLiPS densities for some values of $N_\parallel$. Because of that the SX-mode will not "turn" towards the UHR, where the EBWs are formed. Thus, it can result in the decreased coupling to the EBWs.
Assume a constant magnetic field in the z-direction and the density gradient ∇n_e. Only the SX-mode can propagate in an overdense plasma and its perpendicular refractive index is described by two eigenvalues $N_{\perp,\pm}$. These two eigenvalues are smoothly connected at the turning point as discussed in Sec. 6.3 and shown in Fig. 6.12.
In the O-X coupling, the created SX-mode is initially described by the $N_{\perp,+}$ eigenvalue. After it reaches the turning point, it is described by the $N_{\perp,-}$ eigenvalue. This eigenvalue has a singularity at the UHR. Thus, the created SX-mode will reach the UHR resonance only if the density is high enough that the turning point is in the plasma. Figure 6.12 (a) demonstrates the case when the turning point is not in the plasma. In this case, the SX-mode will never reach the UHR in the ray-tracing simulations, when the plasma is homogeneous along the magnetic field lines. In reality, the eigenmodes can interact with each other. The energy can be coupled from one mode into the other. This coupling process should be analysed using full-wave methods such as FDTD and BVP. Figure 6.12 can be considered as a trivial example of ray-tracing in a plasma with the inhomogene-

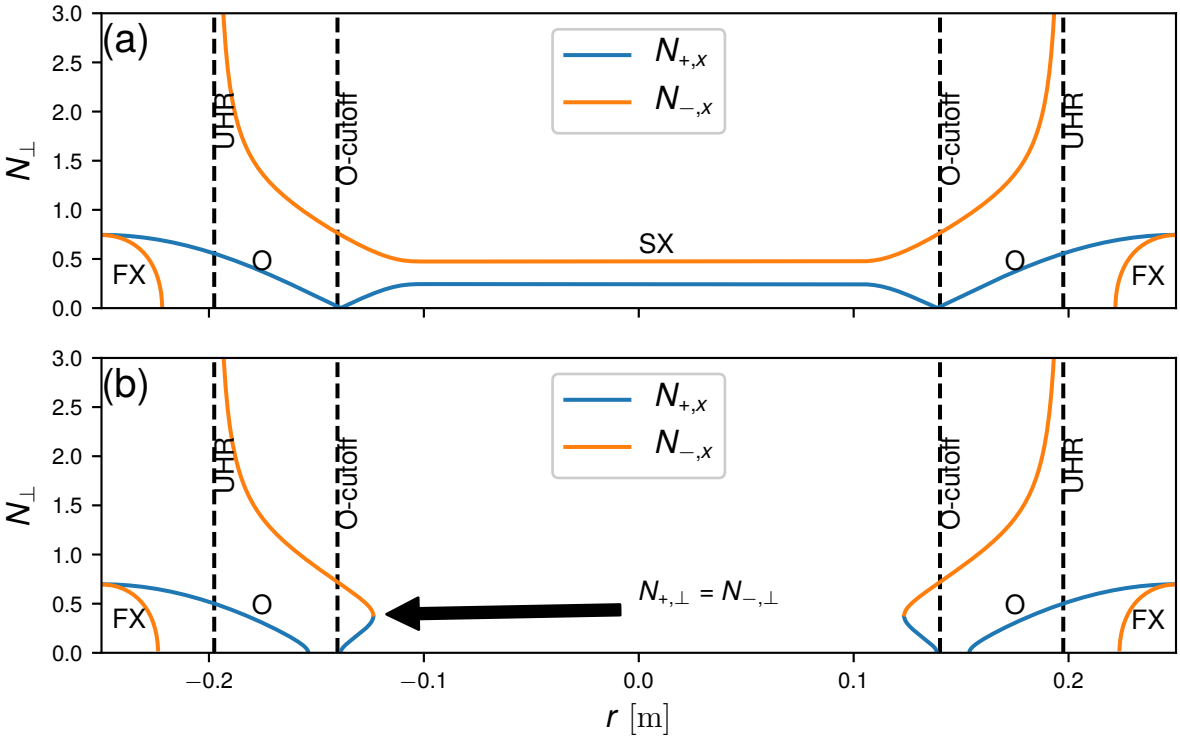

Figure 6.12: $N_\perp$ in the FLiPS plasma as a function of the radial position. (a): $N_\parallel = N_{\parallel,opt}$, in this case, the eigenvalues $N_{\perp,+}$ and $N_{\perp,-}$ are separated and the UHR is not accessible. (b): $N_\parallel > N_{\parallel,opt}$, both eigenvalues have a confluence points, which is a turning point for the SX-mode. In this case, the SX-mode can access the UHR.

ity only in the radial direction. The ray-tracing simulations in the presence of the axial density and magnetic gradient are shown in Fig. 6.13. These simulations were performed using the cold plasma model. Therefore, the SX-mode rays that reached the UHR do not turn into the EBW. The lowest value of $N_\parallel$ indicated by the colorbar corresponds to $N_{\parallel,opt}$. The rays were initiated as + eigenmode. The rays that start propagating with $N_\parallel$ close to $N_{\parallel,opt}$ propagate further inside the plasma. The axial density gradient changes the SX-mode $N_\parallel$. At some point the initial " + "-mode turns into the " − "-mode and starts propagating towards the UHR, where it will resonate in the cold plasma approximation and turn into the EBWs, when the thermal effects are included. When the initial $N_\parallel$ increases, eventually the turning point appears and the SX-mode rays turn towards the UHR. Thus, the axial density gradient can play a significant role in the O-X-EBW conversion.

To see how the EBW rays will be affected by the position of the turning point, the ray-tracing simulations were performed as in Fig. 6.13, but with $T_e \approx 10$ eV. Figure 6.14 shows results of the ray-tracing simulations for two SX-mode rays (I, II). The rays I, II were initiated with $N_\parallel = 0.7$ and $N_\parallel = 0.68$, respectively. The ray I has a larger $N_\parallel$, thus for this ray there is the turning point immediately near the O-cutoff. The ray II having a smaller $N_\parallel$ propagates further into the plasma, but eventually turns towards the UHR. Despite very different trajectories of the SX-mode rays, the subsequently formed EBW rays have similar trajectories. Both EBW rays are confined close to the FLiPS mid-plane. The only difference is that the ray II has a larger amplitude of the oscillations in the z-direction. It shows that even in the weakly overdense plasma the EBWs propagate in a guided fashion. Thus, it can be concluded that the trapping of the EBWs in the linear mirror magnetic field occurs for both O-X and direct X-EBW coupling schemes.

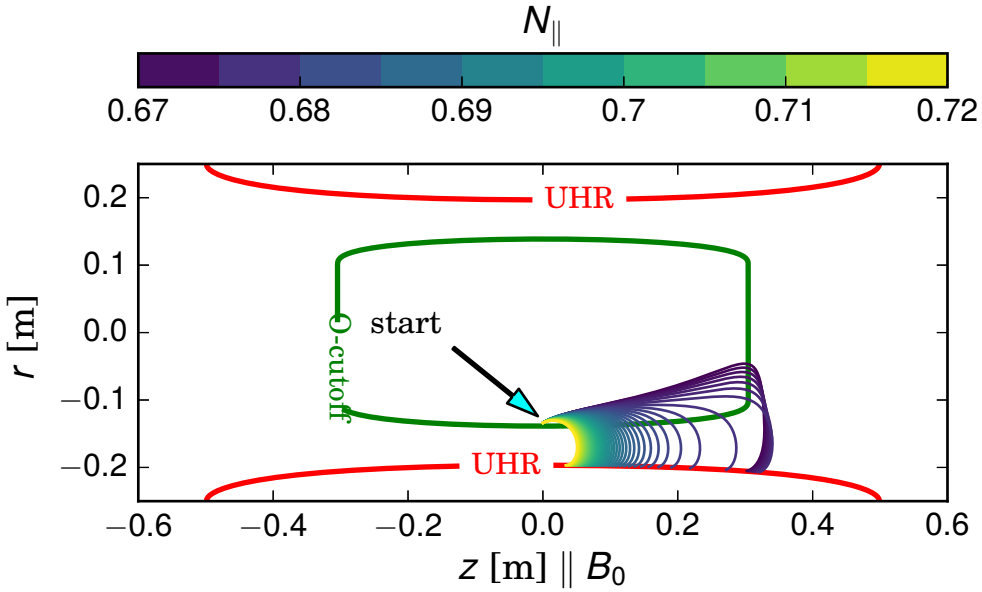

Figure 6.13: Ray-tracing of SX-mode in the plasma with the experimentally measured radial density profile shown in Fig. 3.7. The rays were initiated around $N_{\parallel,opt}$. In these simulations, it was assumed that there was an axial density gradient. The colorbar shows the values of the initial parallel refractive index $N_{\parallel}$. The SX-mode rays that initiated with a larger $N_{\parallel}$ reflect from the plasma at the O-cutoff vicinity. The reflection point as shown in Fig. 6.12 is a confluence point of $N_{\perp,+}$ and $N_{\perp,-}$. If the peak density is too low or $N_{\parallel}$ is not sufficiently large, this point will be absent and the SX-mode rays will not turn towards the UHR. However, the axial density gradient can significantly alter the SX-mode rays trajectories and cause the reflection.

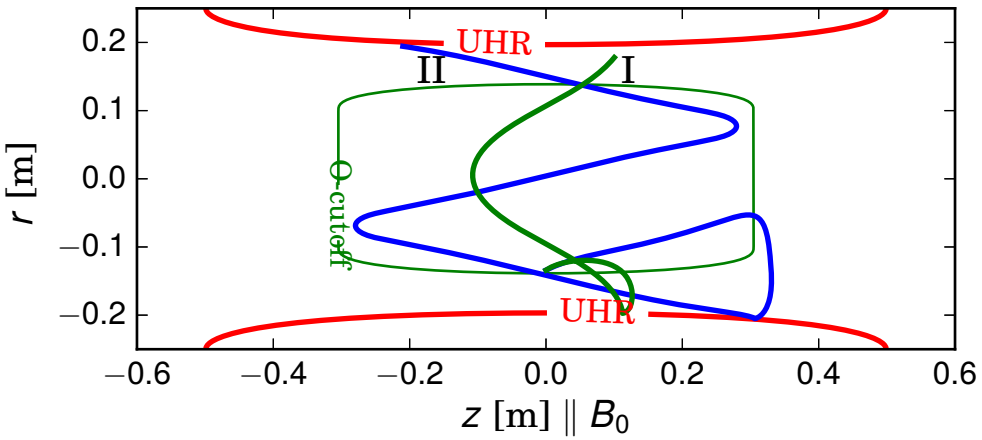

Figure 6.14: Ray-tracing of the SX-mode in the plasma as in Fig. 6.13, but with $T_e = 10$ eV. The ray I was launched with $N_{\parallel} = 0.7$, thus it reflects near the O-cutoff. The ray II was launched with $N_{\parallel} = 0.68$, thus this ray reflects later than the ray I. Since the simulations were preformed in the plasma with $T_e = 10$ eV unlike in Fig. 6.13, the SX-mode becomes an EBW at the UHR. Despite very different SX-mode trajectories, the corresponding EBW rays propagate in a similar fashion caused by the axial inhomogeneous magnetic field.

6.3.4 Summary

In this section, the ray-tracing code RiP was applied to investigate the SX-mode propagation using the classical eikonal approximation. Since the code is based on the hot dispersion relation, the SX-mode turns into an EBW at the UHR. It was shown that the EBW ray propagation direction is mostly affected by the magnetic field in the slab model, for both O-X-B and FX-SX conversion schemes and the EBW ray trajectories only weakly depend on N_z.
The modelling of the SX-mode propagation in the FLiPS relevant geometry revealed that the subsequent EBW rays are guided in a wavechannel formed by the inhomogeneous axial magnetic field forming foci. The ray-tracing investigation of the O-X-B conversion showed the importance of the axial density gradient in the weakly overdense plasmas since in this case some SX-mode rays need the axial density gradient to reach the UHR.
To investigate further the EBW trajectories in the wave channel and to find the corresponding EBW field inside the channel, another ray-tracing code was developed based on the quasi-electrostatic approximation. To obtain the field in the channel, the Wigner function technique will be used. The brief introduction of the method is given in the next section.

6.4 Wigner Function

6.4.1 Distribution

In classical mechanics the velocity and the position of a particle can be both measured simultaneously with arbitrary precision. In quantum mechanics, there is a fundamental limitation due to the "uncertainty principle" $\Delta p \cdot \Delta x \geqslant \hbar$. When the position is known exactly, then $\Delta x = 0$, and in this case, the information about the momentum is completely lost, namely $\Delta p \to \infty$. Similarly, in the eikonal approximation position and the wavevector are known simultaneously along the rays, whereas in the physical optics knowing one of the Fourier-conjugated variables leads to the loss of the information about the other. However, it more intuitive to describe fields or signals simultaneously in terms of its Fourier-conjugated variables. Consider, for instance, a music score. The score specifies occurrence of a tune at a particular time interval, which is perceived as a melody.
A bit more sophisticated example is a spectrogram. Assume that there is a time series of some signal $V(t)$ as shown in Fig. 6.15 (a). In order to the frequency spectrum at each time, a window function can be used. The window function slides along the signal picking only a particular time interval. At each interval the selected piece of the signal is Fourier transformed and the result is shown in Fig. 6.15 (b). The window function's role is to select a particular time-slice of the signal by taking the product of the signal and the window function $V(t')g(t-t')$. Then this product is Fourier transformed to obtain the frequency spectrum around t

$$s(t,\omega) = \int_{-\infty}^{+\infty} V(t')g(t-t')e^{-i\omega t'}dt' \tag{6.18}$$

Obviously, the result will depend on the choice of the window function. To get a better time resolution the window must be more narrow. However, the cost is the decreased frequency resolution.

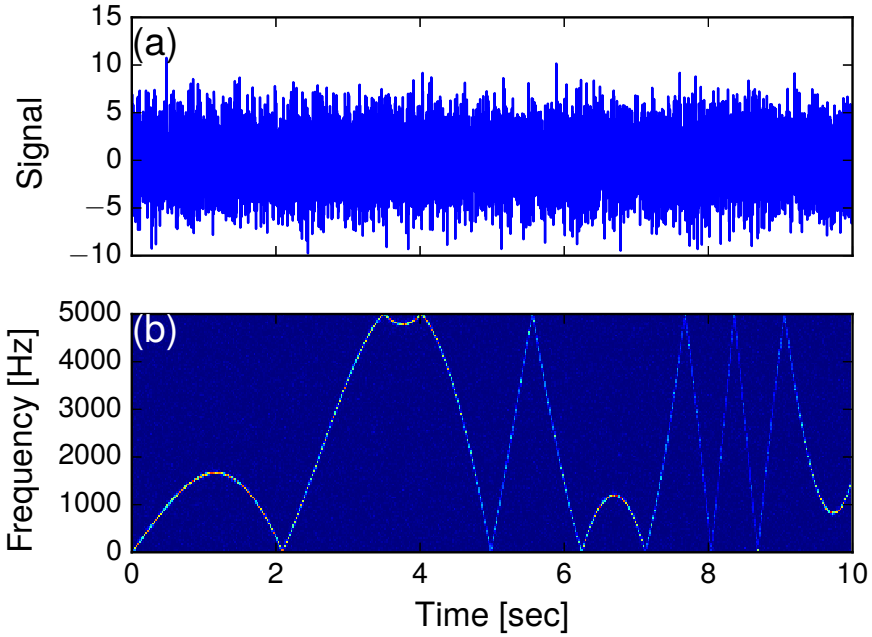

Figure 6.15: (a): An example of a noisy time-dependent signal, (b): corresponding spectrogram shows the dominant frequency at each time. The spectrogram was created with using the Tukey window function [104].

As a motivation to introduce the Wigner function consider again the spectrogram transformation given by Eq. (6.18). Introducing the new variable $q = t - t'$ leads to the integral

$$s \sim \int_{-\infty}^{+\infty} V(t-q)g(q)e^{-i\omega q}dq \tag{6.19}$$

It can be seen that $V(t-q)$ looks like a window function. It implies that the roles of the signal and the window function are equivalent. Naturally, it leads to the idea to use the signal itself as the window function. This idea is reflected in the definition of the Wigner function [11]

$$W(q,p) = \int_{-\infty}^{+\infty} \widehat{f}(q-q'/2)f(q+q'/2)e^{-ipq'}dq' \tag{6.20}$$

where $\widehat{f}$ is the complex conjugate of f. Therefore, the Fourier transform in Eq. (6.20) is "symmetrized" as compared to Eq. (6.18). The variables q, p were used instead of t and ω to emphasize that this method is general and can be applied to any types of signals.

6.4.2 Properties of the Wigner function

As seen from Eq. (6.20) the Wigner function is always real and can be negative. The square modulus of the signal can be recovered from the corresponding Wigner function as follows

$$\begin{aligned} |f(q)| &= \int W(q,p)dp^N \\ |\widehat{f}(p)| &= \int W(q,p)dq^N \end{aligned} \tag{6.21}$$

It is tempting to interpret the Wigner function as a density on the phase-space. But due to its possible negativity the Wigner function is referred to as a quasi-distribution.
Another important property that makes it useful is conservation along the Hamiltonian trajectories. Thus, a procedure can be devised to calculate the field intensity as follows, when the initial field is given at the antenna plane. This initial field is transformed into the Wigner function. For the numerical calculations, the Wigner function can be sampled over the antenna plane. Each sample provides an initial condition for Hamilton's equation. Along each ray the value of the Wigner function will stay constant. Tracing the corresponding rays, the evolved Wigner function can be obtained at the other positions. Using marginal properties given by Eq. (6.21), the corresponding field intensity can be found. The application of this procedure will be demonstrated by the following examples.

6.4.3 Examples

Here, examples of the application of the method of the Wigner function are shown to calculate the field intensity for some simple cases. The first example is the propagation of a plane wave limited by an infinite obstacle with a slit of width $2a$. The field $F(x)$ at the slit is given by

$$F(x) = \begin{cases} Ae^{-ik_0x}, & -a < x < a \\ 0, & \text{otherwise} \end{cases} \tag{6.22}$$

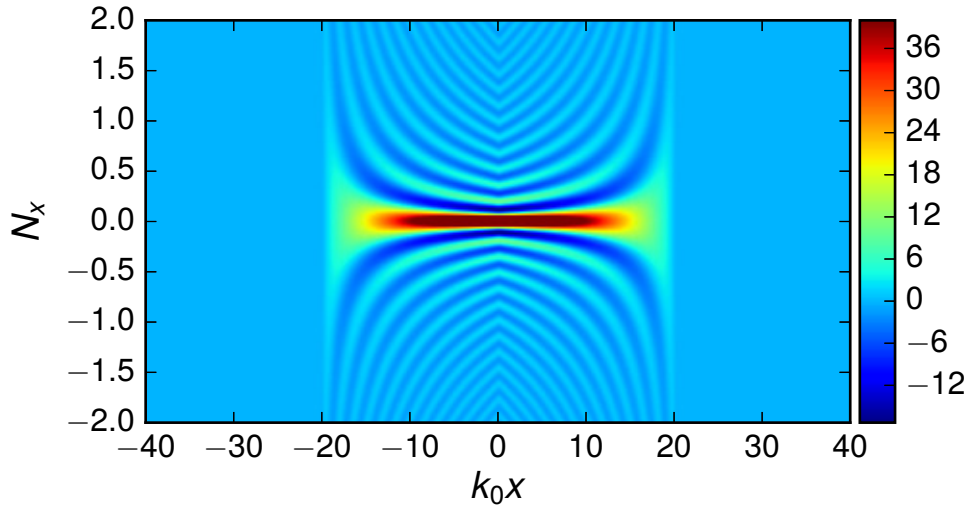

Figure 6.16: The initial Wigner function at the slit with the width $k_0x = 40$ shows an oscillatory behaviour. Note that the Wigner function can be negative, showing that it is not a proper distribution in a strict sense. As expected, outside the slit the function is exactly zero since these points do not contribute to the field intensity.

The initial Wigner function at the slit can be easily found according to Eq. (6.20) and is given by

$$W(x, k_x) = \begin{cases} 2/k_x \sin(2k_x(x-a)), & -a < x < 0 \\ 2/k_x \sin(2k_x(a+x)), & 0 < x < a \\ 0, \quad \text{otherwise} \end{cases} \tag{6.23}$$

Figure 6.16 shows the initial Wigner function on the phase-space. As demonstrated by the figure, the Wigner function is oscillating and is non-positive. Note that the Wigner function is most significant around $N_x = 0$. In the plane of the obstacle, the Wigner function outside the slit is exactly zero. Tracing the rays and using the marginal relations (6.21), the field intensity is found as shown in Fig. 6.17. Despite the loss of the phase information, the resulting field intensity captured the wave effects. For instance, one can see the dark Arago spot [105].

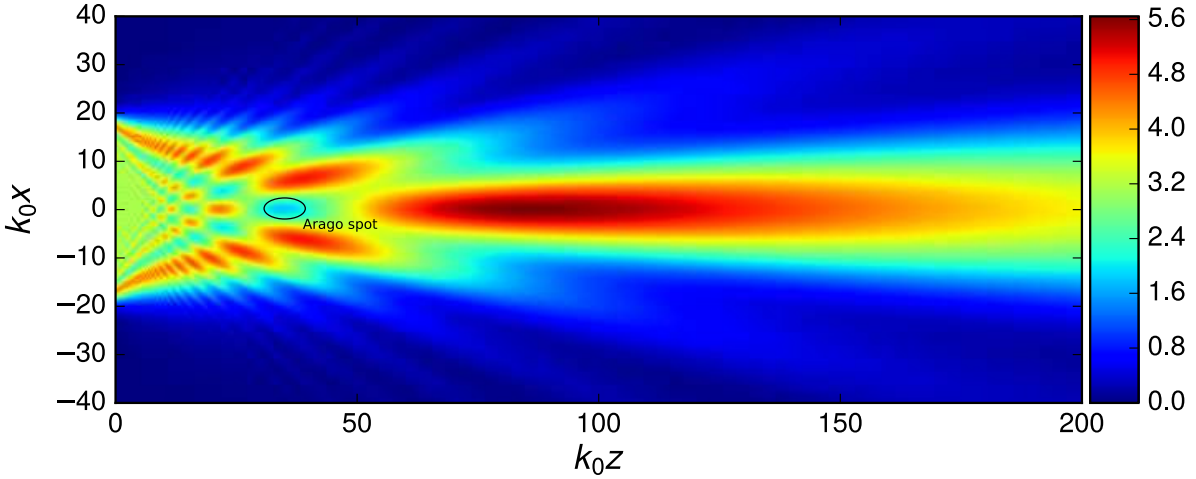

Figure 6.17: The field intensity of the plane wave after passing through the slit located at $k_0z = 0$, obtained using the Wigner function method.

The second example demonstrates the Gaussian beam propagation in a lense-like medium. A lens-like medium is characterised by a parabolic refractive index dependency. As illustrated in Fig. 6.18 the rays do not diverge indefinitely, but are confined near the direction

of propagation as the divergence due to the diffraction effects is balanced out by the focusing effects. Figure 6.18 shows the strip of the region where the intensity was calculated using the Wigner function method. The figure also shows the superimposed gray rays

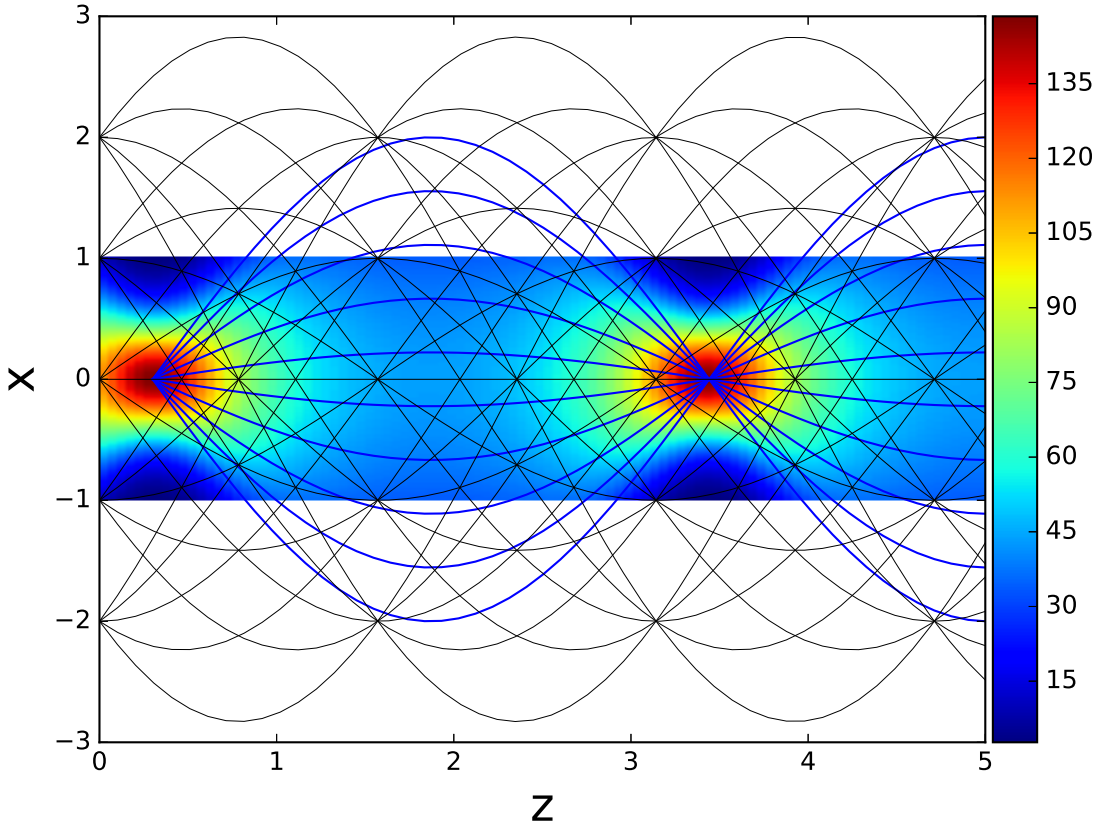

Figure 6.18: The field intensity of a wave propagating in the medium with $n(x) = 1 - \alpha x^2$. Due to the periodic focusing caused by the medium, the medium is often referred to as a lens-like medium. The superimposed rays were used to propagate the Wigner function (only some rays are shown).

that were used to calculate the Wigner function. To compare the ray-tracing with the results obtained with the method of the Wigner function, the rays (shown in blue) were traced with the origin in the left focus. As expected, the rays trajectories diverge, and then focus again at the right focus.
The solutions of the presented examples can be also found analytically [15]. The results of the analytical predictions agree with the numerical solutions obtained with the implemented method of the Wigner function confirming the validity of the code. In the following, the Wigner function method will be applied to the EBW propagation in the FLiPS plasma.

6.5 Results

The results of the ray-tracing calculations in the FLiPS plasma showed that the EBW rays are guided in a wavechannel formed by the inhomogeneous magnetic mirror field as described in Sec. 6.3. Since the guiding effect limits the spread of the wave, it leads to the EBW focusing. To determine the shape of the foci, their size and dependency on the plasma parameters, the ray-tracing alone is not sufficient, and the EBW field intensity

is required. In general, it is not possible to obtain the field intensity from ray-tracing calculations due to caustics such as foci as described in Sec. 6.2, since the ray-tracing calculations predict that in focal regions the field intensity is infinite. This difficulty can be overcome by applying the theory of the Wigner function described in the previous section to the EBW propagation in the FLiPS plasma.
The Wigner function requires tracing of multiple EBW rays. In the following simulations, up to 10000 rays were traced. Since the rays are independent of each other, the simulations can be easily parallelized. The simulations were carried on a computational server with 40 cores. However, even when the simulations are parallelized, using the full-hot dispersion relation to trace the rays leads to very long simulation runs which is impractical. Also, the high complexity of the full-hot dispersion relation can cause unforeseen numerical problems. This motivated the implementation of another code that is based on the electrostatic approximation to trace EBW rays.
The use of the electrostatic approximation brings two limitations. First, only the EBW rays can be traced and secondly, close to the UHR the electrostatic approximation breaks down since the EBWs turn back into the SX-mode which is not included in the electrostatic dispersion relation. However, tracing only EBW rays was sufficient to study the focusing properties of the wavechannel.
The investigation of the EBW propagation was carried out for two magnetic field configurations to study how the foci are affected by the magnetic field. The first magnetic field configuration is the one that was normally used in the experiments as described in Ch. 3. The second magnetic configuration has a larger mirror ratio $\beta = B_{max}/B_{min} = 3.9$ which is created by the currents $I_{out} = 1800$ A and $I_{in} = 10$ A in the outer and inner coils, respectively. Both configurations correspond to the fundamental EBW harmonic.
In the simulations, it was assumed that the initial EBW beam had a Gaussian shape similarly to the example shown in Fig. 6.18. It is convenient to use the Gaussian distribution for the initial EBW field since in this case, the initial Wigner function can be easily found analytically [12]. This choice of the initial form of the EBW beam is further justified by the argument that the FX-SX tunnelling is the most efficient for the perpendicular ($N_{\|} = 0$) FX-mode injection. Since the axial inhomogeneity in the FLiPS plasma is mild, the parallel refractive index of the EBWs will be also small with $N_{\|} \approx 0$, and the EBWs will propagate predominantly perpendicular to the magnetic field. Thus, the initial EBW distribution should have its maximum in the center ($z = 0$) and gradually decrease as $|z|$ increases, which can be conveniently modelled by the Gaussian distribution.
However, the initial field of the EBWs could be calculated using the boundary value problem or the FDTD method. This would allow a consistent coupling of the full-wave simulations of the electromagnetic waves such as X- and O-mode with the simulations of the EBWs performed with the Wigner function method. Such an approach was used, for example, in [85] to couple the full-wave and the ray-tracing simulations to investigate waves with very different wavelength scales.
For the magnetic field used in the experiments the calculated intensity of the EBWs is shown in Fig. 6.19.

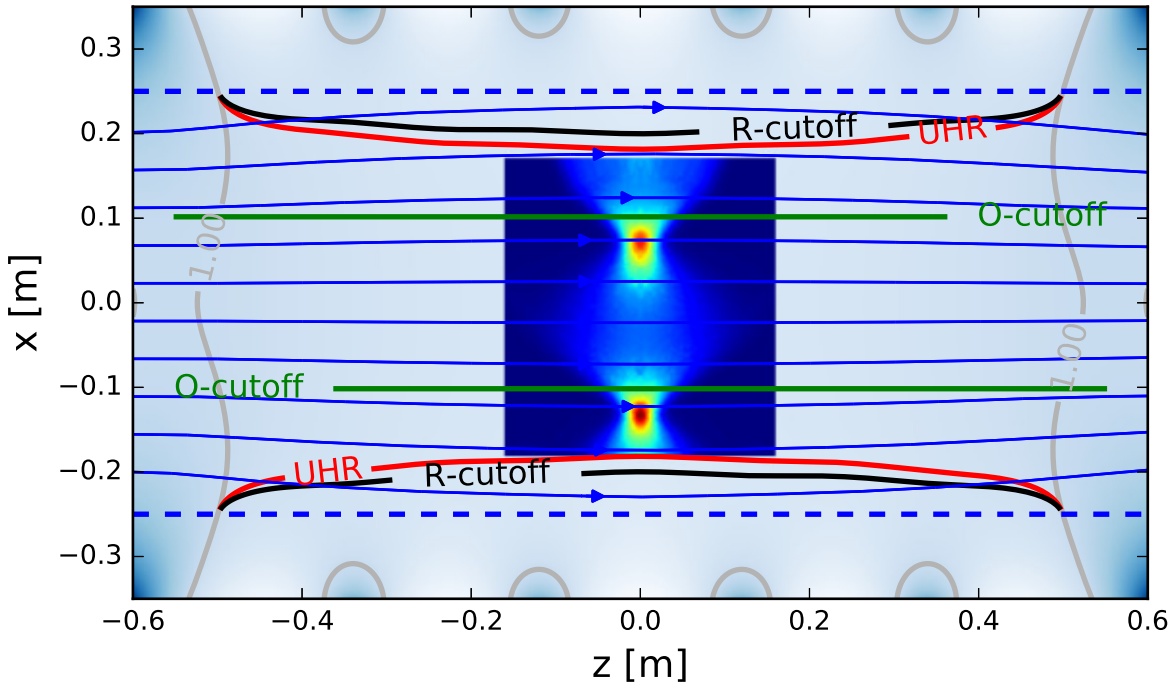

Figure 6.19: Field intensity of the EBWs in the wave channel calculated using the Wigner function approach. The used density profile was measured experimentally and shown in Fig. 3.7. The magnetic field was created by 500A in the outer coils and 320A in the inner coils. This magnetic field configuration was normally used during the experiments.

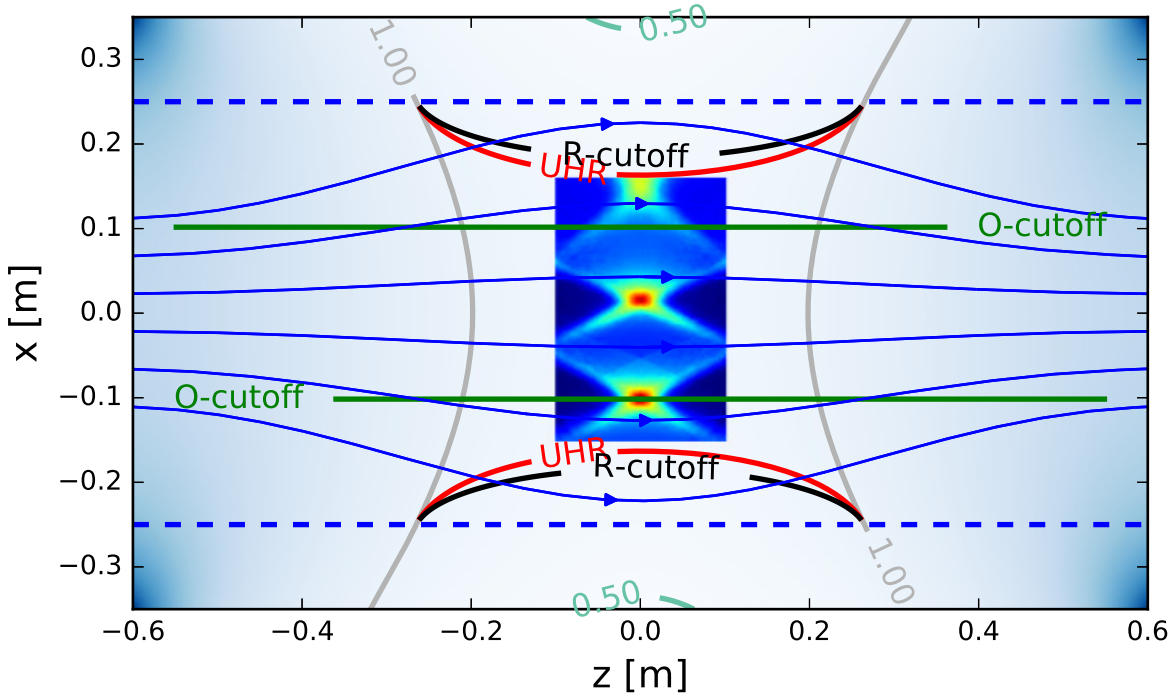

Figure 6.20: Field intensity of EBWs in a magnetised plasma with the magnetic field ratio $\beta = 3.9$. Three focal regions can be identified. Note, this configuration was not experimentally possible.

As expected from the ray-tracing simulations, there are two regions of amplified intensity. The field intensity is similar to the field intensity distribution shown in Fig. 6.18. It shows that for this magnetic field, the plasma acts as a lens-like medium on the EBWs.
The implemented method was used to investigate the EBW propagation in a magnetic field with a stronger axial inhomogeneity as shown in Fig. 6.20. The EBWs were launched as a Gaussian beam at $x = -0.15$ m at UHR vicinity. In this case, the EBWs form

three foci with amplified intensity. For the presented magnetic field configuration, one of the foci occurs at the UHR at $x = 0.15$ m. In the case of the larger magnetic field ratio the EBW field intensity distribution is not completely identical to the field intensity distribution found in a lens-like medium with the foci having four-pointed star-like shapes. It shows that the plasma properties deviate from a lens-like medium for the magnetic field configurations with higher magnetic field ratios.
Using the Wigner function method, it is possible to calculate the EBW field intensity in the foci of the wavechannel, where according to the standard ray-tracing approach the field is infinite. The calculations with the Wigner function confirm that there are two foci in the wavechannel for the magnetic field used in the experiments.
The number of foci was shown to dependent on the axial magnetic field. For stronger magnetic field gradients there are more foci. This can be attributed to the fact that the width of the formed wavechannel is smaller in the case of the strong axial magnetic field gradient. The existence of the different EBW foci locations and as a consequence the strong variation of the EBW intensity should allow the experimental verification of the focusing of the EBWs in the wavechannel. The EBWs in the focal regions can be measured experimentally with a movable monopole antenna [106]. The dedicated experimental set-up and the results will be discussed in the next chapter.

Chapter 7

EBW experiments

7.1 Introduction

The previous chapters were dealing with the simulations of the wave propagation in the FLiPS plasma for the experimentally measured plasma parameters presented in Ch. 3. Using the ray-tracing method, it was shown that it should be possible to measure experimentally the effect of inhomogeneity of the axial magnetic field on the EBW propagation. Extending the ray-tracing results using the Wigner function method, the EBW field intensity was obtained. The spatial regions of the amplified EBW intensity due to the axial inhomogeneity of the magnetic field were identified. This effect can be thought of as a focusing of the EBWs by the plasma. This chapter deals with the results of the experiment that was devised to investigate the possible focusing of EBWs in the central mid-plane of FLiPS.

7.2 Monopole antennas

The microwave field in FLiPS was investigated using the so-called monopole antennas [107, 108]. Monopole antennas were used to detect EBWs indirectly measuring the signal of daughter waves created in the parametric decay [109]. There are also reports, where monopole antennas were used to directly detect EBWs in toroidal plasmas [110] and in stellarators [111]. In [112] the antennas were used to detect the parametric decay in a magnetic mirror plasma, which is a FLiPS relevant case. The authors reported on their unsuccessful attempts to carry out the phase measurements using two monopole antennas. The phase measurements allow calculation of the wavevector of the plasma waves. Since the frequency of the signal is known (given by the signal generator), it becomes possible to identify the type of plasma waves based on the dispersion relation. The authors proposed that the turbulence significantly decreased the coherence length of the waves, which made the phase measurements impossible. For such measurements to be performed successfully, a quiescent plasma is required that can be produced by the so-called Q-machines [113].
In this study, an antenna that is similar to the one described in [56] was used. The antenna is made of a semi-rigid coaxial cable (SUCOFORM_47_CU). At the end the shield and the insulator are both removed over a length of 1 mm, allowing the exposed inner conductor to pick up the microwave signal. The cable is inserted into a ceramic tube with the end closed to avoid the tip damage and to electrically isolate it from the plasma.

Otherwise, the antenna measures not only the electric field but also the plasma density fluctuations, similarly to a Langmuir probe.
Figure 7.1 depicts a schematic of the experimental set-up to investigate the EBW propagation in FLiPS. The probing signal frequency was 2.31 GHz to avoid interference with the 2.45 GHz main heating frequency. The 2.31 GHz X-mode or O-mode could be launched through the open waveguide antenna. The output of the signal generator was amplified resulting in a 20 W output signal. Opposite to the launcher a monopole antenna was installed as a receiver. The DC break capacitor (C) was installed as a high-pass filter. The 2.45 GHz notch filter (NF) was introduced before the amplifier (A) to protect the signal analyser from the stray power of the main heating source. Finally, the received signal was measured by the spectrum analyser (SA).

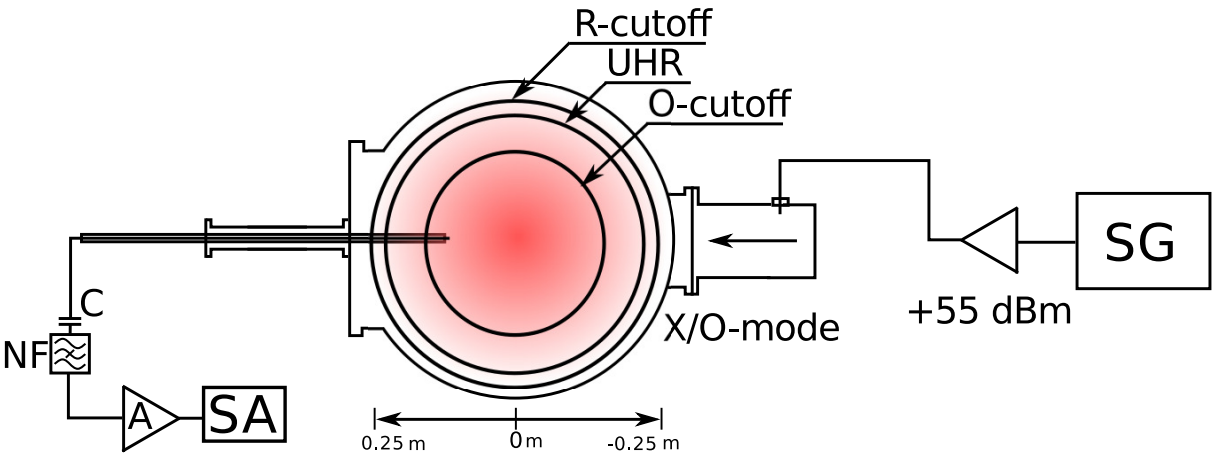

Figure 7.1: Experimental set-up to detect EBWs in FLiPS. The transmitter circuit contained the signal generator (SG) and a power amplifier. The amplified signal was fed into the open waveguide antenna. The monopole receiving antenna was installed opposite to the transmitter. The capacitor (C) served as a high-pass filter and was placed to insulate the spectrum analyser from the plasma. The 2.45 GHz notch filter (NF) was placed before the amplifier (A) to protect the the spectrum analyser from the power of the main plasma heating system. The received signals was then amplified by the amplifier (A) and measured by the spectrum analyser (SA). The monopole antenna scanning range in the radial direction was from the edge $r = 0.25$ m to the plasma center $r = 0$ m.

The antenna tip length L was $\lesssim 1$ mm and the diameter was $d = 0.31$ mm. Thus, the antenna did not have good polarisation selectivity. According to [114], the possible wave vector spectrum produced by such an antenna has $k_{max} \approx \frac{2\pi}{L}$. The wave refractive index surfaces [115], shown in Fig. 7.2, determine the possible directions of the wavevector and its magnitude in the FLiPS plasma. The open parabolic refractive index surface with the large refractive index corresponds to EBWs. The surface in the enlarged area belongs to the SX-wave. Note a significant difference between the EBW and SX-refractive indices due to the small T_e. Indeed, as discussed in Ch. 5, the EBW wavelength decreases with T_e. The gray area has a radius of $N_{max} = \frac{ck_{max}}{\omega}$. All the waves with the refractive indices inside the circle could couple to the antenna. Therefore, the constructed monopole antenna could be used to detect the EBWs in FLiPS.

7.3 Results

To ensure that the diagnostic system works properly, first measurements were performed without the plasma. A radial scan of microwave field of the auxiliary signal without the plasma is shown in Fig. 7.3. The expected standing wave pattern with the half-wavelength separation between the maxima can be seen as expected.

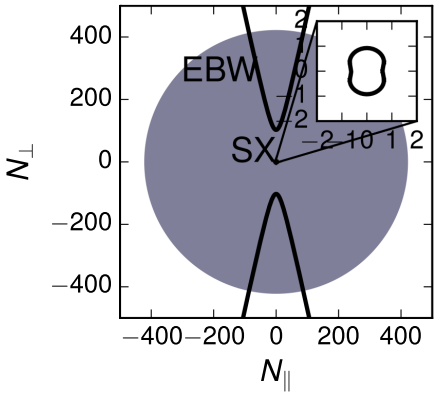

Figure 7.2: The refractive index surfaces of the waves in the FLiPS plasma. A refractive index surface gives the magnitude of the components of the vector $\vec{N} = c\vec{k}/\omega$. Due to low T_e the EBW refractive index is much larger than the refractive index of the SX-mode. The waves with the refractive indices inside the gray area can be detected by the monopole antenna.

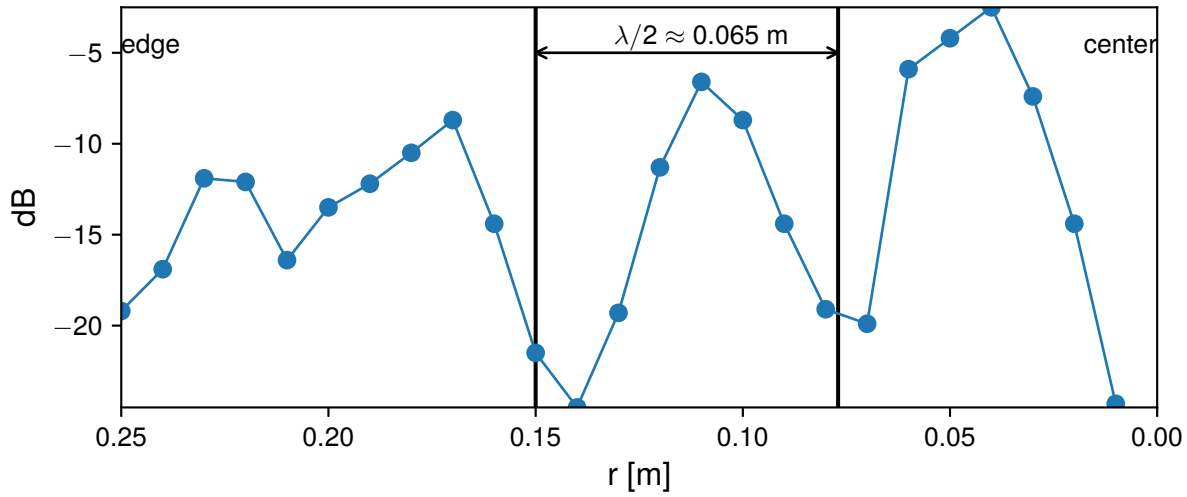

Figure 7.3: The measured 2.31 GHz microwave signal without the plasma. The standing wave pattern is clearly visible.

Figure 7.4 shows the radial scan with the monopole antenna when plasma is present for two shots. In both shots, the plasma was under the same conditions. The signals are shown together with the assumed density profile presented in Ch. 3. The corresponding R-cutoff and the UHR are also shown. The amplitude of both signals is significantly decreased compared to the case without the plasma. However, at the UHR there is no expected amplification of the electric field.

7.4 Discussion

When an antenna is immersed into a plasma, the antenna radiation pattern will be strongly affected [20] compared to the radiation pattern in vacuum. A magnetised plasma can limit the antenna radiation to only the so-called resonance cones as discussed in Sec. 2.2. The reciprocity theorem states that when an antenna is used as a receiver, the antenna will pick up the signal from the directions given by its radiation pattern. Thus, in a magnetised plasma a monopole antenna can in general pick up signals from the directions given by the resonance cone. However, in the overdense region of the FLiPS plasma, the resonance cones cease to exist. Indeed, the resonance cones exist only, when

both P and S have different signs as seen from Eq. (2.21). The FLiPS plasma has a large overdense region where $P < 0$. Additionally, at the monopole antenna position the inequality $\omega_{ce} < \omega$ was fulfilled, from which follows that $S < 0$. Thus, the only type of electrostatic waves that can be measured by the monopole antenna in the plasma bulk are the EBWs.
The FDTD simulations showed the strongest field amplification right on the front of the antenna as can be seen in Fig. 4.10. One of the possible explanations of the lack of the expected field amplification at the UHR in the experimentally measured signals in Fig. 7.4 is that the monopole antenna was placed on front of the open waveguide transmitter as shown in Fig. 7.1. Thus, the incoming 2.31 GHz signal traversing the plasma in the ra-

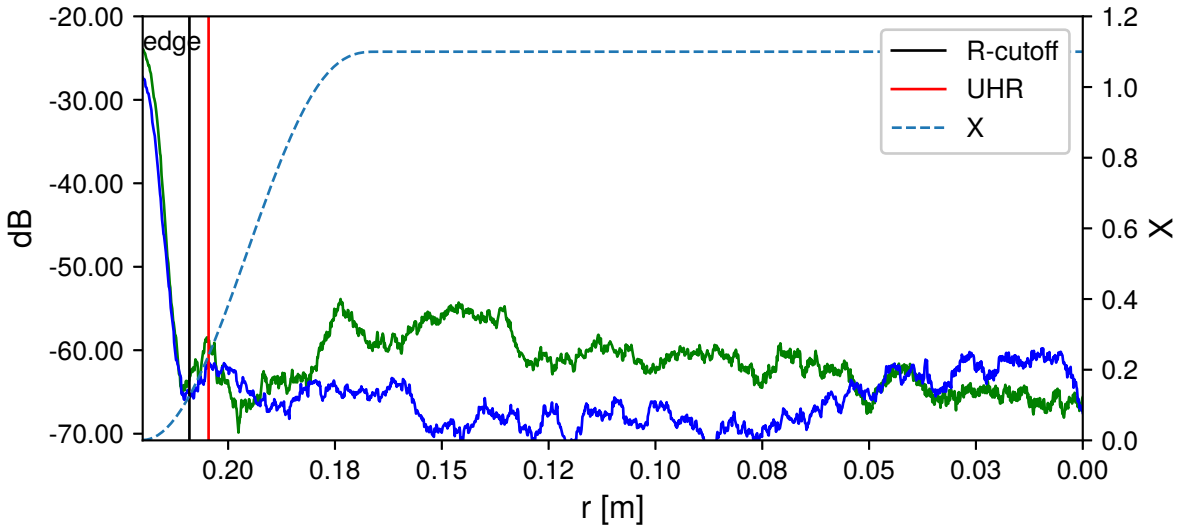

Figure 7.4: Intensity of 2.31 GHz signal measured with the monopole antenna along the radius for two different shots. Both shots were performed for the same parameters: the neutral gas pressure 10^{-2} Pa and the optimal magnetic field configuration described in Ch. 3. The positions of the R-cutoff and the UHR are indicated with the vertical lines. For both shots there is a clear indication of the effect of the R-cutoff, since at the plasma edge the signal is several orders of magnitude stronger than after the R-cutoff. The expected field amplification at the UHR is not observed.

dial direction was effectively scattered by the plasma as shown in Ch. 4. Therefore, the scattering could significantly decrease the amount of energy that reaches the UHR, where the monopole antenna was placed. Another possible explanation is that the collisions effectively dissipated the energy at the UHR, which is situated at the plasma edge where $T_e < 10$ eV.
Simulations in Ch. 6 show that EBWs are confined by the axial magnetic field inhomogeneity compensating the divergence of the EBW beam in the axial direction. Thus, it is expected that the EBW intensity decreases more slowly than that of the SX-wave. Additionally, as a result of the low T_e, the Landau damping of the EBWs is practically negligible for a wide range of $N_{\parallel}$ as discussed in Sec. 3.4.4. Furthermore, the full-wave simulations with the BVP method described in Sec. 5.3 showed that for the relevant collisional frequency in FLiPS the collisional damping should not significantly affect the EBW propagation. All these considerations lead to the conclusion that the EBW should have been detectable in FLiPS.
As shown in Fig. 7.4 beyond the R-cutoff there is no obvious EBW signal. The possible explanation for the lack of the signal is the plasma turbulence. Indeed, as pointed in [7] the plasma in a simple magnetic mirror configuration is turbulent whenever $\omega_{pe} > \omega_{ce}$. The focusing effect was modelled in Sec. 6.4, where the EBWs were launched as a Gaussian beam and the turbulence was not included. Due to the turbulence the positions of

the R-cutoff and the UHR are both fluctuating, therefore, the incoming FX-wave can undergo an abrupt R-cutoff, or the position of the SX-wave formation will be changing. Such processes lead to degradation of the foci in the wavechannel. The plasma fluctuations can also create high-density plasma blobs which trap the EBW [116], which can significantly alter the expected EBW ray trajectories. The interferometric measurements provide the density averaged along the probing microwave beam. Because of that the fluctuation level obtained with the interferometer is underestimated. Thus, to monitor the density fluctuation at the edge position a Langmuir probe was used at a large negative voltage to measure the ion saturation current given by Eq. (3.3). Assuming that $\sqrt{T_e}$ fluctuations do not affect much $I_{i,sat}$, it becomes possible to estimate the local n_e fluctuations. $I_{i,sat}$ measurements at the plasma edge are shown in Fig. 7.5. From the standard deviation σ and the mean value μ, the local level of the density fluctuations δn_e can be estimated as follows

$$\frac{\delta n_e}{\bar{n}_e} \approx 0.25 \tag{7.1}$$

It clearly shows that the fluctuations δn_e are significant and can cause the EBW scattering, which makes their detection much more complicated than it was originally anticipated.

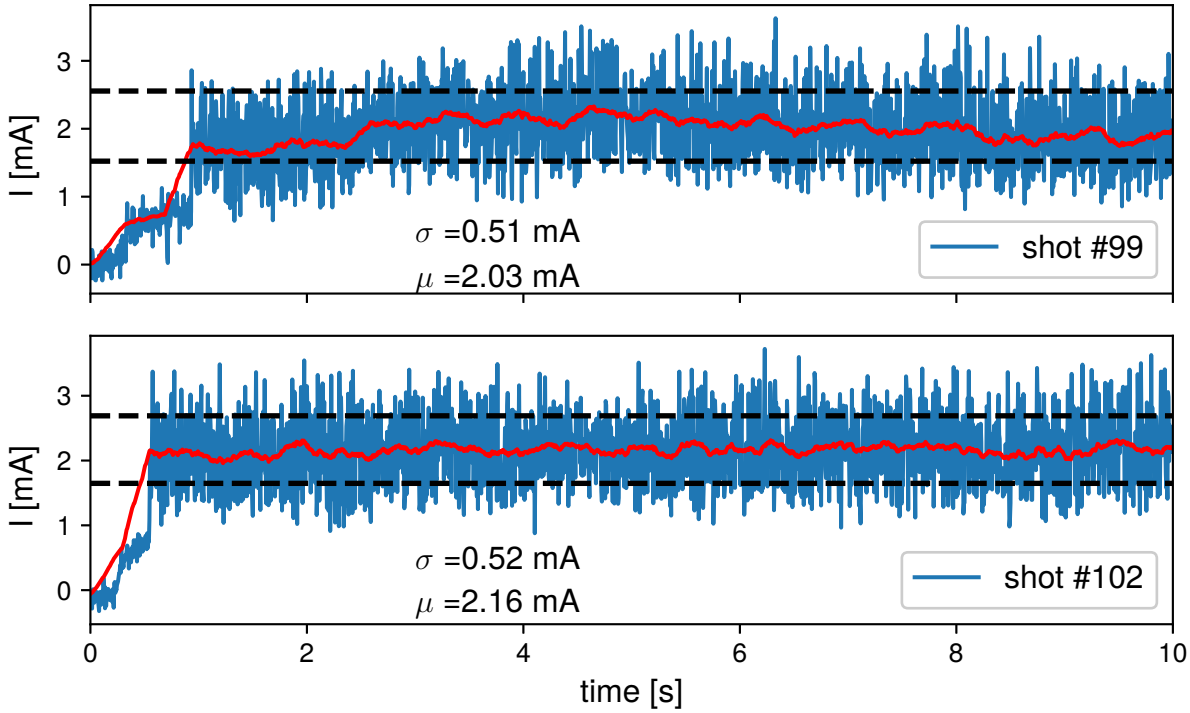

Figure 7.5: The ion saturation current $I_{i,sat}$ measured at the plasma edge shows strong local density fluctuations. σ and μ are the standard deviation and the signal mean respectively.

7.5 Summary

This chapter dealt with the experimental studies of the EBW propagation in FLiPS plasma. The main objective of the presented experimental study was detection of the EBW foci that are caused by the mirror magnetic field. The simulations in the previous chapters demonstrated that the focusing effect exists for different magnetic fields and

density profiles.
The measurements were performed with a simple monopole antenna. The EBWs were created through the direct FX-SX-EBW coupling. No clear EBW signal was detected.
The simulation results in the previous chapters showed that when turbulence is not included the EBWs should be able to propagate in the FLiPS plasma. Moreover, the monopole antenna signal showed an excellent agreement between the theoretically predicted positions of the R-cutoff and the measurements. It confirms that the experimentally measured density profile described in Ch. 3 and used in the simulations is indeed the correct profile. Therefore, the plasma turbulence was identified as a likely candidate for the negative result.
Nevertheless, it is not possible to completely exclude the role of the collisions at the UHR, since the UHR is situated at the plasma edge, where the plasma can be colder than expected. Furthermore, in [40] was explicitly stated that in a plasma similar to the FLiPS plasma the SX-mode is completely collisionally damped before reaching the UHR. Thus, to answer the question why the EBWs were not detected in this experiment, more precise measurements of the plasma edge are required as well as more advanced simulations methods such as particle-in-cell simulations.

Chapter 8

Summary and Outlook

8.1 Summary

This thesis was concerned with the application and implementation of different numerical methods to investigate the wave propagation in the Flexible Linear Plasma device FLiPS. The FLiPS plasma is produced in a 1.16 m long, 0.5 m diameter vessel, by injection of the R-wave at 2.45 GHz. The axial magnetic field with an adjustable magnetic mirror at the ends allowed to optimize the confinement, and to study the wave propagation in magnetised plasmas. The applied methods were the Finite-Difference Time-Domain method (FDTD), Boundary Value Problem (BVP), and the phase-space methods such as the ray-tracing and the Wigner function method. Every method has its pros and cons, related to the numerical cost and the nature of the approximations used. Thus, each method is suited well for different physical regimes. Indeed, the FDTD method is very powerful, but also can become unstable or produce non-physical waves, when the upper hybrid resonance is included. But it is very useful for the analysis of systems with complex geometries or when the characteristic sizes of a system are of the same order as the wavelength.
The BVP approach, being much less general than the FDTD method, allowed the inclusion of the Electron Bernstein Waves (EBWs) in the simulations. Another advantage of the BVP method over the FDTD method is that the BVP method is unconditionally stable and does not produce non-physical modes.
When the wavelength becomes much smaller than the characteristic length of the plasma, it becomes impractical to apply full-wave methods such as the FDTD and the BVP codes, since both of them must utilise a very fine numerical grid to resolve the wavelength scale. In this case, the geometrical optics approximation is valid and one can use the ray-tracing instead, which is computationally fast. In this approximation, wave effects such as diffraction are completely neglected. However, applying the so-called Wigner function, it is possible to recover the wave effects such as beam spreading, based purely on the ray-tracing simulations.
First, the FDTD method was applied to visualise the wave propagation in the FLiPS plasma. The importance of the wall reflections was clearly demonstrated as the reflections strongly affect the coupling efficiency to the EBWs. These simulations helped to understand the lack of the difference between the O- and X-mode auxiliary heating observed in FLiPS.
To simulate the EBW propagation, a BVP code was developed in the frequency domain. The EBWs were included in the simulations by treating the thermal effects as a small per-

turbation added to the cold plasma dielectric tensor. This method allowed simulations of EBWs in the UHR vicinity. Using this approach, the entire FX-SX-EBW coupling scheme was simulated, since it is the most promising coupling scenario to generate EBWs in the FLiPS plasma. The effect of the normalised collision frequency ν_{coll}/ω on the EBWs was investigated for FLiPS relevant magnetic field configurations. The simulations showed that EBW propagation is almost unaffected by collisions for $\nu_{coll}/\omega < 10^{-4}$, which is consistent with [38].

The ray-tracing and the Wigner function method were used to simulate the EBWs farther away from the UHR. The application of the methods is justified since the EBW-wavelength is very short compared to the typical plasma gradient lengths of the FLiPS plasma. Ray-tracing showed that the EBW propagation is strongly affected by the axial magnetic field in FLiPS. Thus, it is possible to control the direction of the EBW propagation by adjusting the magnetic field gradient. This effect can be used for the non-mechanical steering of the EBWs for controlled local heating. When EBWs are launched in the radial direction of the FLiPS' mid-plane, the EBW beam is predicted to undergo periodic focusing and de-focusing induced by the axial magnetic field gradient, implying that the plasma acts on the EBWs as a lens-like medium.

The numerical investigations were accompanied by dedicated experiments. The plasma was created by 2.45 GHz R-wave heating. The plasma was moderately overdense with $T_e \approx 10$ eV. The measured density profile had a steep edge, which favoured the direct FX-SX coupling. The experimentally used magnetic field was such that the fundamental electron cyclotron resonance was lying inside the plasma to ensure efficient absorption of the incoming R-wave. The magnetic mirror ratio was chosen such that there were no high energy electrons that produce the X-ray radiation, whilst the plasma had a good axial plasma confinement. The EBWs were created by the FX-SX coupling at 2.31 GHz. This frequency was chosen to avoid interference with the main 2.45 GHz heating frequency. As a receiver for the EBW signal, a radially movable monopole antenna was used. The measured parameters of the experiments indicated that both plasma turbulence and collisional damping can significantly affect EBW and SX-mode propagation in the FLiPS plasma.

The goal of the experiments was to experimentally demonstrate the numerically predicted focusing of the EBWs. The main obstacle to measure the focusing effects is assumed to come from turbulent plasma density fluctuations, since the FX-SX-EBW coupling strongly depends on the density-gradient length at the UHR. Another possible candidate for the lack of detected EBW signals is the location of the UHR close to the plasma edge, where the electron temperature is low. In this case, the EBW wavelength is very short and collisional damping can become dominant.

The predicted focusing of the EBWs is not limited only to magnetic mirror devices such as FLiPS. The described focusing effect can be found in other plasma devices where EBW propagation occurs. The practical application of the predicted focusing effect can be local plasma heating for the current drive. Also non-linear processes can be caused by the EBW focusing, since the field strength in the focal regions can exceed the parametric instability threshold. Thus, the consideration of the focusing effect is important for the analysis of experimental results. The numerical tools developed in the course of the thesis that were used to simulate the focusing effect can be applied to other magnetic field and plasma geometries.

Summarising, the EBW propagation in the FLiPS plasma was investigated with different numerical methods. Combination of the methods provided a complete theoretical picture

of the EBW propagation in FLiPS that would be unattainable applying only one numerical scheme. As a result, focusing of EBWs was predicted in the FLiPS plasma, and the dedicated experiments were carried out to verify the effect experimentally.

8.2 Outlook

In this thesis, various numerical methods were used to investigate EBW propagation in the FLiPS plasma. In this section, future plans for further work concerning the simulations and experiments are summarised.
All the simulations were either in the 1D or 2D geometry. In future studies, this simplification could be removed, and the simulations could be performed in the 3D geometry. Furthermore, additional vacuum vessel details such as ports can be included in the numerical model. The existing FDTD code used in the thesis, can simulate wave propagation in the 3D geometry. Thus, future work on the wave propagation in the 3D geometry would be concerned with the model creation and validation of the obtained results. In this thesis, the FDTD simulations were carried out on a regular rectangular grid. The code can be extended to use an adaptive grid. Using a grid with a higher resolution only in the UHR vicinity would significantly speed up the calculations.
The study of the influence of turbulent density fluctuations on the wave propagation using FDTD simulations would also be helpful. In this thesis, the plasma density fluctuations were included in the FDTD approximately by modifying the peak plasma density. In the future, local density perturbations due to turbulence should be included in the model.
The BVP simulations were performed in the 1D geometry. The model was used to describe the wave propagation in the FLiPS plasma in radial direction. Performing 2D simulations would allow to include effects of the axial plasma density and the magnetic field inhomogeneity on the wave propagation. These simulations would allow the investigation of the focusing of the EBWs by the inhomogeneous axial magnetic field.
The BVP simulations of the EBW propagation are valid only in the UHR vicinity. For the full-wave simulations of EBWs in the whole plasma other methods such as particle-in-cell should be applied. The work in this direction would be a development of a particle-in-cell code or adoption of an existing code for the FLiPS geometry.
Concerning the ray-tracing studies, the existing code could be extended to the 3D geometry. The wave absorption due to the collisional and Landau damping, as well as the cyclotron absorption can be studied with the present code.
The experimental set-up should be further improved. The thickness of the current lead shielding must be increased to avoid exposure to the X-rays in compliance with the safety requirements. The lead shield will also allow to use a wider range of accessible plasma parameters. For example, the magnetic field configuration that was used in the experiments was chosen such as to avoid strong X-ray radiation. In this configuration, the plasma was in direct contact with the vacuum window of the main heating system causing deterioration of the window surface. Using other magnetic field configurations, in which the plasma produces stronger X-ray radiation will avoid this issue. The configurations with the higher magnetic field ratios will also produce a more stable and denser plasma.
Together with the higher heating power and an optimised antenna, the accessible plasma parameters would allow experiments with negligible influence of collisions, and thus prove the predicted focusing and steering effect of EBWs.

Appendix A

Conversion efficiency calculations

According to [20] the average flux of electromagnetic energy in a medium is

$$\vec{P} = \frac{c}{16\pi}(\vec{E}^* \times \vec{B} + \vec{E} \times \vec{B}^*) \tag{A.1}$$

This energy flux in a magnetised plasma in general is made up of four components corresponding to forward (transmitted) and backward (reflected) propagating O- and X-modes. When the total energy flux is measured to the left from the UHR, finding the conversion efficiency requires the energy flux carried by the reflected O-mode. Solving (5.11) for the coefficient c_3 that corresponds to the back-propagating O-mode

$$c_3 = \frac{-E_y\alpha_4 + E_z - \alpha_1 + \alpha_4}{\alpha_3 - \alpha_4} \tag{A.2}$$

Thus the energy flux of the reflected O-mode is

$$P^O_{out} = \frac{1}{2}\epsilon_0 c|c_3|^2 \mathrm{Re}(\gamma_3 - \alpha_3\beta_3) \tag{A.3}$$

To speed up the calculations, in some simulations, the wave propagation was considered only to the right from the UHR. In this case, the singularity at the UHR is excluded from the simulation domain, allowing to set the collisional frequency to zero. The energy flux carried by the SX-mode can be found using the c_4 coefficient

$$c_4 = \frac{-E_z + \alpha_1 + \alpha_3(E_y - 1)}{\alpha_3 - \alpha_4} \tag{A.4}$$

And the energy flux is

$$P^X_{out} = \frac{1}{2}\epsilon_0 c|c_4|^2 \mathrm{Re}(\gamma_4 - \alpha_4\beta_4) \tag{A.5}$$

Appendix B

Ray-Tracing

B.1 Coordinate transformation

The plasma dispersion relation is derived in the coordinate system defined with respect to the background magnetic field. That is, the z-axis is chosen to point in the direction of the magnetic field $\vec{B_0}$. To define uniquely the system of coordinates the wave vector $\vec{k}$ is required to lie in the xz-plane. This system of coordinates is referred to as **local system of coordinates**. However, the plasma parameters variation and the background magnetic field are most easily defined in **the global system of coordinates** which is decoupled from the magnetic field definition.
Thus, to be able to use Hamilton's equations the transformation from the local to global system coordinates must be calculated. More specifically, there is a function $D(X, Y, n_x, n_z)$ in the local system of coordinates whose arguments are the function of the global coordinates. That is,

$$\begin{cases} X = X(\vec{r}) \\ Y = Y(\vec{r}) \\ \vec{n} = \vec{n}(\vec{N}) \end{cases} \tag{B.1}$$

where $\vec{r}$ and $\vec{N}$ are the coordinates and the refractive index in the global coordinates. For clarity in the following notation $\vec{Y}$ is the magnetic field in the global coordinates. Hamilton's equations require the following derivatives

$$\begin{cases} \dfrac{\partial D}{\partial \vec{N}} = \dfrac{\partial D}{\partial n_x}\dfrac{\partial n_x}{\partial \vec{N}} + \dfrac{\partial D}{n_z}\dfrac{\partial n_z}{\partial \vec{N}} \\ \dfrac{\partial D}{\partial \vec{r}} = \dfrac{\partial D}{\partial X}\dfrac{\partial X}{\partial \vec{r}} + \dfrac{\partial D}{\partial Y}\dfrac{\partial Y}{\partial \vec{r}} + \dfrac{\partial D}{\partial n_x}\dfrac{\partial n_x}{\partial \vec{r}} + \dfrac{\partial D}{\partial n_z}\dfrac{\partial n_z}{\partial \vec{r}} \end{cases} \tag{B.2}$$

Thus, in order to find $\frac{\partial D}{\partial \vec{N}}$ and $\frac{\partial D}{\partial \vec{r}}$, first one calculates $\frac{\partial n_x}{\partial \vec{N}}$, $\frac{\partial n_z}{\partial \vec{N}}$, $\frac{\partial Y}{\partial \vec{r}}$, $\frac{\partial n_x}{\partial \vec{r}}$ and $\frac{\partial n_z}{\partial \vec{r}}$. Expressing n_z and n_x explicitly as the functions of $\vec{N}$ and $\vec{Y}$, the following equations are obtained

$$\begin{cases} n_z = \vec{N} \cdot \dfrac{\vec{Y}}{Y} \\ n_x = \sqrt{N^2 - (\vec{N} \cdot \dfrac{\vec{Y}}{Y})^2} \end{cases} \tag{B.3}$$

The first equation follows from the definition of the local system of coordinates and the second follows from the Pythagorean theorem. Now, the following derivatives can be

found with respect to $\vec{N}$

$$\begin{cases} \dfrac{\partial n_z}{\partial \vec{N}} = \dfrac{\vec{Y}}{Y} \\ \dfrac{\partial n_x}{\partial \vec{N}} = \dfrac{\vec{N} - \frac{\vec{Y}\cdot\vec{N}}{Y}\vec{Y}}{n_x} \end{cases} \tag{B.4}$$

The next step is to find derivatives with respect to $\vec{r}$

$$\begin{cases} \dfrac{\partial Y}{\partial \vec{r}} = \dfrac{\vec{Y}}{Y}\nabla\vec{Y} \\ \dfrac{\partial n_z}{\partial \vec{r}} = \dfrac{n_x}{Y}\dfrac{\partial n_x}{\partial \vec{N}}\nabla\vec{Y} \\ \dfrac{\partial n_x}{\partial \vec{r}} = -\dfrac{n_z}{n_x}\dfrac{\partial n_z}{\partial \vec{r}} \end{cases} \tag{B.5}$$

This concludes the derivation of the coordinate transformation that is used in the RiP code.

B.2 Ray-Tracing solver

The ray-tracing uses Hamilton's equation to find the ray trajectories. In the ray-tracing context, the Hamiltonian is a dispersion function $D(\vec{r}, \vec{N})$ and the dispersion relation is the surface defined as $D(\vec{r}, \vec{n}) = 0$. Since the trajectories are found numerically, the numerical error leads to growth of the dispersion relation with time. It is especially pronounced for slow waves such as EBWs.
However, using the fact that a Hamiltonian can be multiplied by some non-vanishing function and still produce the same trajectories [11]. Thus, to trace the EBW and reduce the numerical drift, the dispersion function $D' = D/n_x^4$ was used. Since for EBWs $n_x \gg 1$, this modification helped to reduce the numerical drift when calculating EBW trajectories.

B.3 Derivatives of Plasma Dispersion function

The hot plasma dielectric tensor elements cannot be expressed in terms of the elementary functions. Instead one has to rely on special functions which can be represented as an integral of elementary functions or as a solution of a differential equation. Examples of special functions are the Bessel functions and the Plasma Dispersion Function [20]:

$$Z(\zeta) = i\int_0^\infty dz(i\zeta z - \frac{z^2}{4}) = i\sqrt{\pi}\omega(\zeta) \tag{B.6}$$

where $\omega(\zeta)$ is the complex error function and ζ is

$$\zeta = \frac{q-n}{\gamma q N_\parallel} \tag{B.7}$$

The RiP code requires the Plasma Dispersion Function and its first two derivatives which are given by

$$Z^{'} = -2 - 2\zeta Z \tag{B.8}$$

$$Z^{''} = -2(Z + \zeta Z^{'}) \tag{B.9}$$

Although the information on the Plasma Dispersion function can be found in many textbooks [25], the details on the calculation of the second derivative Z'' will be presented here because the numerical calculations of its second derivative requires a careful treatment for large ζ. If Z'' is not treated properly, its imaginary part will be wrong due to floating-point arithmetic. The problem with the imaginary part of the Z'' can be understood using the following formula

$$Im\ Z''(\zeta) = -4/\sqrt{\pi}(\zeta - 2\zeta^2 D(\zeta)) - 4/\sqrt{\pi}D(\zeta) \tag{B.10}$$

where $D(\zeta)$ is Dawson's function [25]. In the case of large ζ, the asymptotic expansion of $D(\zeta) \sim \frac{1}{2\zeta}$, therefore, the leading terms of the expression $-4/\sqrt{(}\pi)(\zeta - 2\zeta^2 D(\zeta))$ cancel out, and the value of the expression is given by the small corrections of the higher orders. Thus, when $N_{\|}$ is small, the machine numerical precision can be exceeded.
In the RiP code, for small values of ζ, $D(\zeta)$ function was used to calculate Z'', but for large ζ, Z'' was calculated using the asymptotic series for $D(\zeta)$. The values of Z'' for the intermediate values of ζ were smoothly connected using the Lagrange polynomial interpolation [25]. This allowed performing the correct ray-tracing for the whole range of the refractive indices.

Bibliography

[1] F. F. Chen, *Introduction to plasma physics and controlled fusion*, Plenum Press, New York, 1984.

[2] V. L. Ginzburg, *The Propagation of Radio Waves: The Theory of Radio Waves of Low Power in the Ionosphere and Magnetosphere*, Gordon and Breach, Science Publishers, Inc., New York, 1961.

[3] M. Brambilla, *Kinetic Theory of Plasma Waves: homogeneous Plasmas*, 1998.

[4] H. P. Laqua, H. J. Hartfuß, and W7-AS Team, Phys. Rev. Lett. **81**, 2060 (1998).

[5] G. Taylor et al., Physics of Plasmas **12**, 052511 (2005).

[6] H. P. Laqua, Plasma Physics and Controlled Fusion **49**, 1 (2007).

[7] R. Geller, *Electron Cyctron Resonance Ion Sources and ECR Plasmas*, Taylor & Francis, 1996.

[8] A. Taflove and S. C. Hagness, *Computational electrodynamics: the finite-difference time-domain method. 2nd ed*, volume 67-106, 2000.

[9] P. Bellan, Journal of Computational Physics **136**, 654 (1997).

[10] F. Hansen, J.-P. Lynov, C. Maroli, and V. Petrillo, Journal of Plasma Physics **39**, 319 (1988).

[11] E. R. Tracy, A. J. Brizard, A. S. Richardson, and A. N. Kaufman, *Ray Tracing and Beyond: Phase Space Methods in Plasma Wave Theory*, Cambridge University Press, 2014.

[12] S. W. McDonald, Physics Report **158**, 337 (1988).

[13] A. Torre, *Linear Ray and Wave Optics in Phase Space*, Elsevier Science, 2005.

[14] M. A. Alonso, Adv. Opt. Photon. **3**, 272 (2011).

[15] H. Weber, Ausbreitung hochfrequenter Wellen in fluktuierenden Plasmen, Master's thesis, Max-Planck-Institut für Plasmaphysik, 2013.

[16] L. D. Landau and E. M. Lifshitz, *Electrodynamics of continuous media*, Pergamon Press, 1960.

[17] V. Ginzburg, *Propagation of Electromagnetic Waves in Plasma*, Pergamon, 1960.

[18] W. Tierens and D. De Zutter, Physics of Plasmas **19**, 112110 (2012).

[19] W. Tierens and D. De Zutter, AIP Conference Proceedings **1580**, 195 (2014).

[20] T. Stix, *Waves in Plasmas*, American Institute of Physics, 1992.

[21] I. B. Bernstein, Phys. Rev. **109**, 10 (1958).

[22] F. W. Crawford and J. A. Tataronis, Journal of Applied Physics **36**, 2930 (1965).

[23] F. Leuterer, Plasma Physics **14**, 499 (1972).

[24] J. Urban et al., Nuclear Fusion **51**, 083050 (2011).

[25] M. Abramowitz, *Handbook of Mathematical Functions, With Formulas, Graphs, and Mathematical Tables,*, Dover Publications, Inc., New York, NY, USA, 1974.

[26] J. Preinhaelter and V. Kopecky, Journal of Plasma Physics **10**, 1 (1973).

[27] K. G. Budden, *The Propagation of Radio Waves: The Theory of Radio Waves of Low Power in the Ionosphere and Magnetosphere*, Cambridge University Press, 1985.

[28] N. A. Gondarenko, P. N. Guzdar, S. L. Ossakow, and P. A. Bernhardt, Journal of Geophysical Research: Space Physics **108** (2003).

[29] F. Volpe, Physics Letters A **374**, 1737 (2010).

[30] A. Köhn et al., Plasma Physics and Controlled Fusion **50**, 085018 (2008).

[31] E. Mjølhus, Journal of Plasma Physics **31**, 7 (1984).

[32] A. K. Ram and S. D. Schultz, Physics of Plasmas **7**, 4084 (2000).

[33] R. Post, Nuclear Fusion **27**, 1579 (1987).

[34] B. H. Quon and R. A. Dandl, Physics of Fluids B: Plasma Physics **1**, 2010 (1989).

[35] J. Bornemann, S. Amari, J. Uher, and R. Vahldieck, IEEE Transactions on Microwave Theory and Techniques **47**, 330 (1999).

[36] H.-J. Hartfuß and T. Geist, *Fusion Plasma Diagnostics with mm-Wave*, Wiley, 2007.

[37] I. H. Hutchinson, *Principles of plasma diagnostics*, Cambridge University Press, 2002.

[38] S. J. Diem et al., Phys. Rev. Lett. **103**, 015002 (2009).

[39] S. Pešić, Physica B+C **125**, 118 (1984).

[40] K. C. Hammond, R. R. Diaz-Pacheco, A. Köhn, F. A. Volpe, and Y. Wei, Plasma Physics and Controlled Fusion **60**, 025022 (2018).

[41] S. K. Hansen, S. K. Nielsen, M. Salewski, M. Stejner, and J. S. and, Plasma Physics and Controlled Fusion **59**, 105006 (2017).

[42] V. Shevchenko et al., Fusion Science and Technology **52**, 202 (2007).

[43] E. Gusakov and A. Surkov, arXiv preprint physics/0410190 (2004).

[44] A. Köhn et al., Plasma Physics and Controlled Fusion **55**, 014010 (2012).

[45] F. W. Crawford and H. H. Weiss, Journal of Nuclear Energy. Part C, Plasma Physics, Accelerators, Thermonuclear Research **8**, 21 (1966).

[46] J. P. Sheehan and N. Hershkowitz, Plasma Sources Science and Technology **20**, 063001 (2011).

[47] B. Nold et al., New Journal of Physics **14**, 063022 (2012).

[48] N. Mahdizadeh et al., Plasma Physics and Controlled Fusion **47**, 569 (2005).

[49] F. Crawford, Nuclear Fusion **5**, 73 (1965).

[50] Y. I. O. Yury A. Kravtsov, *Geometrical Optics of Inhomogeneous Media*, Springer-Verlag Berlin Heidelberg, 1990.

[51] A. Köhn, G. Birkenmeier, E. Holzhauer, M. Ramisch, and U. Stroth, Plasma Physics and Controlled Fusion **52**, 035003 (2010).

[52] K. S. Yee, IEEE Trans. in Antennas and Propagation Magazine **14**, 302 (1966).

[53] M. U. Bohner, Full-wave simulation of microwave propgation in fusion plasmas, Master's thesis, Stuttgart University, 2011.

[54] A. Samimi and J. J. Simpson, IEEE Transactions on Antennas and Propagation **63**, 269 (2015).

[55] M. Surkova et al., Antennas and Propagation, IEEE Transactions **62**, 6307 (2014).

[56] A. Köhn, *Investigation of microwave heating scenarios in the magnetically confined low-temperature plasma of the stellarator TJ-K*, PhD thesis, University of Stuttgart, Stuttgart, 2010.

[57] C. Lechte, G. D. Conway, T. Görler, and C. Tröster-Schmid, Plasma Physics and Controlled Fusion **59**, 075006 (2017).

[58] B. Plaum, H. Kumric, M. Grunert, and E. Holzhauer, Numerical and experimental investigation of ohmic losses in corrugated wall structures, in *2006 Joint 31st International Conference on Infrared Millimeter Waves and 14th International Conference on Teraherz Electronics*, pages 272–272, 2006.

[59] Lechte, Carsten et al., EPJ Web Conf. **203**, 04010 (2019).

[60] R. B. White and F. F. Chen, Plasma Physics **16**, 565 (1974).

[61] A. Köhn et al., Plasma Physics and Controlled Fusion **60**, 075006 (2018).

[62] E. Holzhauer and E. Blanco, Nuclear Fusion **46**, 824 (2006).

[63] D. Pozar, *Microwave Engineering, 4th Edition*, Wiley, 2011.

[64] H. Höhnle, Diploma thesis, Master's thesis, Universität Stuttgart, Stuttgart, 2008.

[65] P. Diez, Diploma thesis, Master's thesis, Institut für Plasmaforschung der Universität, Stuttgart, 2009.

[66] W. Tierens and D. de Zutter, **23**, 225 (2013).

[67] A. G. Shalashov and E. D. Gospodchikov, Plasma Physics and Controlled Fusion **52**, 025007 (2010).

[68] G. Jia and Z. Gao, Physics of Plasmas **24**, 022506 (2017).

[69] S. H. Kim, H. Y. Lee, J. G. Jo, and Y. S. Hwang, Physics of Plasmas **21**, 062108 (2014).

[70] A. Köhn, E. Holzhauer, and U. Stroth, Plasma Science, IEEE Transactions **36**, 1220 (2008).

[71] E. Jones et al., SciPy: Open source scientific tools for Python, 2001–, Online.

[72] U. Ascher, J. Christiansen, and R. D. Russell, Colsys—a collocation code for boundary-value problems, in *Codes for Boundary-Value Problems in Ordinary Differential Equations*, edited by B. Childs, M. Scott, J. W. Daniel, E. Denman, and P. Nelson, pages 164–185, Berlin, Heidelberg, 1979, Springer Berlin Heidelberg.

[73] H. Igami, M. Uchida, H. Tanaka, and T. Maekawa, Plasma Physics and Controlled Fusion **46**, 261 (2003).

[74] A. H. Seltzman, J. K. Anderson, S. J. Diem, J. A. Goetz, and C. B. Forest, Phys. Rev. Lett. **119**, 185001 (2017).

[75] A. H. Seltzman, J. K. Anderson, A. M. DuBois, A. Almagri, and C. B. Forest, Review of Scientific Instruments **87**, 11E329 (2016).

[76] O. Sauter, *Nonlocal analyses of electrostatic and electromagnetic waves in hot, magnetized, nonuniform, bounded plasmas*, PhD thesis, Ecole Polytechnique federal de Lausanne, Lausanne, EPFL, 1992.

[77] S. Ledvina, Y. Ma, and E. Kallio, Space Science Reviews **139**, 143 (2008).

[78] A. Arefiev et al., Nuclear Fusion **57**, 116024 (2017).

[79] M. Ali Asgarian, J. P. Verboncoeur, A. Parvazian, and R. Trines, Physics of Plasmas **20**, 102516 (2013).

[80] N. A. Lopez and A. K. Ram, Plasma Physics and Controlled Fusion **60**, 125012 (2018).

[81] L. I. Schiff, *Quantum mechanics*, McGraw-Hill New York, 3rd edition, 1968.

[82] N. Marushchenko, Y. Turkin, and H. Maassberg, Computer Physics Communications **185**, 165 (2014).

[83] V. Erckmann et al., Fusion Science and Technology **52**, 291 (2007).

[84] T. Whitted, Commun. ACM **23**, 343 (1980).

[85] Y. Petrov, A. Bécoulet, and I. Monakhov, Physics of Plasmas **7**, 911 (2000).

[86] H. Igami et al., Plasma and Fusion Research **11**, 2403098 (2016).

[87] Weber, Hannes, Maj, Omar, and Poli, Emanuele, EPJ Web of Conferences **87**, 01002 (2015).

[88] L. Guidi et al., Journal of Physics: Conference Series **775**, 012005 (2016).

[89] A. Snicker et al., Nuclear Fusion **58**, 016002 (2017).

[90] G. V. Pereverzev, Physics of Plasmas **5**, 3529 (1998).

[91] E. Poli et al., Computer Physics Communications **225**, 36 (2018).

[92] V. I. Arnold, *Catastrophe Theory*, Springer Verlag, 1992.

[93] A. V. Timofeev, Physics-Uspekhi **47**, 555 (2004).

[94] D. B. Batchelor, R. Goldfinger, and H. Weitzner, Plasma Science, IEEE Transactions on **8**, 78 (1980).

[95] D. Swanson, *Plasma Waves*, Academic Press, 1989.

[96] E. Nelson-Melby, R. W. Harvey, A. P. Smirnov, and A. K. Ram, Plasma Physics and Controlled Fusion **49**, 1913 (2007).

[97] F. Castejón, Á. Cappa, M. Tereshchenko, and Á. Fernández, Nuclear Fusion **48**, 075011 (2008).

[98] M. A. Balakina, A. G. Shalashov, E. D. Gospodchikov, and O. B. Smolyakova, Radiophysics and Quantum Electronics **49**, 617 (2006).

[99] F. R. Hansen, J. P. Lynov, and P. Michelsen, Plasma Physics and Controlled Fusion **27**, 1077 (1985).

[100] A. L. Virovlyansky, D. V. Makarov, and S. V. Prants, Physics-Uspekhi **55**, 18 (2012).

[101] R. J. Armstrong, A. Fredriksen, H. L. Pecseli, and J. Trulsen, Plasma Physics and Controlled Fusion **26**, 703 (1984).

[102] A. Cardinali and F. Romanelli, Physics of Fluids B: Plasma Physics **4**, 504 (1992).

[103] A. Cardinali, Physics of Fluids B: Plasma Physics **5**, 2778 (1993).

[104] F. J. Harris, Proceedings of the IEEE **66**, 51 (1978).

[105] M. Born et al., *Principles of Optics: Electromagnetic Theory of Propagation, Interference and Diffraction of Light*, Cambridge University Press, 7 edition, 1999.

[106] K. Uchijima, T. Takemoto, J. Morikawa, and Y. Ogawa, Plasma Physics and Controlled Fusion **57**, 065003 (2015).

[107] G. Janzen, *Kurze Antennen*, Franckh'sche Verlagshandlung, Stuttgart, 1986.

[108] G. Janzen, *Monopolantennen und Vertikalantennen: Analyse von Antennenstrukturen*, G. Janzen, 1999.

[109] V. K. Yadav and D. Bora, Physics of Plasmas **11**, 4582 (2004).

[110] E. Yatsuka, K. Kinjo, J. Morikawa, and Y. Ogawa, Review of Scientific Instruments **80**, 023505 (2009).

[111] Y. Y. Podoba et al., Phys. Rev. Lett. **98**, 255003 (2007).

[112] U. T. Wolters, *Nichtlineare Wellenphänomene und Heizszenario in einer EZR-Spiegelentladung*, PhD thesis, Ruhr-Universität Bochum, 2001.

[113] I. Alexeff, W. D. Jones, and D. Montgomery, The Physics of Fluids **11**, 167 (1968).

[114] V. V. Nazarov, M. V. Starodubtsev, and A. V. Kostrov, Physics of Plasmas **20**, 032110 (2013).

[115] G. Stott, Journal of Atmospheric and Terrestrial Physics **45**, 219 (1983).

[116] E. Z. Gusakov, A. Y. Popov, and A. N. Saveliev, Plasma Physics and Controlled Fusion **56**, 015010 (2014).

Danksagung

An dieser Stelle möchte ich allen Personen danken, die diese Arbeit ermöglicht haben und mir geholfen haben:
Prof. Dr. Thomas Hirth danke für die Betreuung der Arbeit. Trotz der großen Anzahl Ihrer Doktoranden haben Sie Zeit für Treffen gefunden, und immer nach dem Stand der Arbeit gefragt,
Prof. Dr. Emanuele Poli für die aufwändigen Korrekturen meiner Arbeit,
Dr. Eberhard Holzhauer für längere Diskussionen über Plasma-Wellen, und für die Unterstützung im Labor. Die Erinnerungen an den "roten kommunistischen Stift" bringen mich immer noch zum Lächeln,
Dr. Walter Kasparek für die Betreuung der Arbeit und für die Hilfe mit Mikrowellenmessungen, und fürs Zeigen, dass Physik nicht kompliziert sein muss,
Dr. Alf Köhn für die Diskussionen über Plasma-Wellen und unendlichen Optimismus,
Dr. Burkhard Plaum für die Unterschtützung bei IT-Probleme und für Gespräche über Mikrowellentechnik,
Dr. Carsten Lechte für die Geduld mit meinen Fragen über Programmierung und für den FD3D-Code, ich bin immer noch begeistert von der Qualität des Codes,
Bernhard Roth und *Achim Zeitler* für die Hilfe bei allen möglichen technischen Probleme,
Roland Munk für den Experimentaufbau und für die Organisation der Weihnachtsfeier,
Frau Wagner und *Ruth Edelmann-Amrhein* für die Hilfsbereitschaft und Organisation. Die Ausländerbehörden werden nie die kräftige Stimme der Frau Edelmann-Amrhein vergessen.
Allen Doktoranden für sehr interessante Gespräche,
meinen Eltern *Marina* & *Aleksandr Rumiantsev* für die Unterstützung,
meine Freundin *Rafaela Slompo* dafür, dass sie immer für mich da war. Ohne dich würde ich nie so viele schöne Orte besuchen.

Eidesstattliche Erklärung

Hiermit erkläre ich, dass ich die vorliegende Arbeit selbstständig verfasst und dazu keine anderen als die angegebenen Quellen und Hilfsmittel verwendet habe und dass alle Stellen, die wörtlich oder sinngemäß anderen Arbeiten entnommen wurden, durch Angabe der Quellen kenntlich gemacht sind.

Stuttgart, den Kirill Rumiantsev